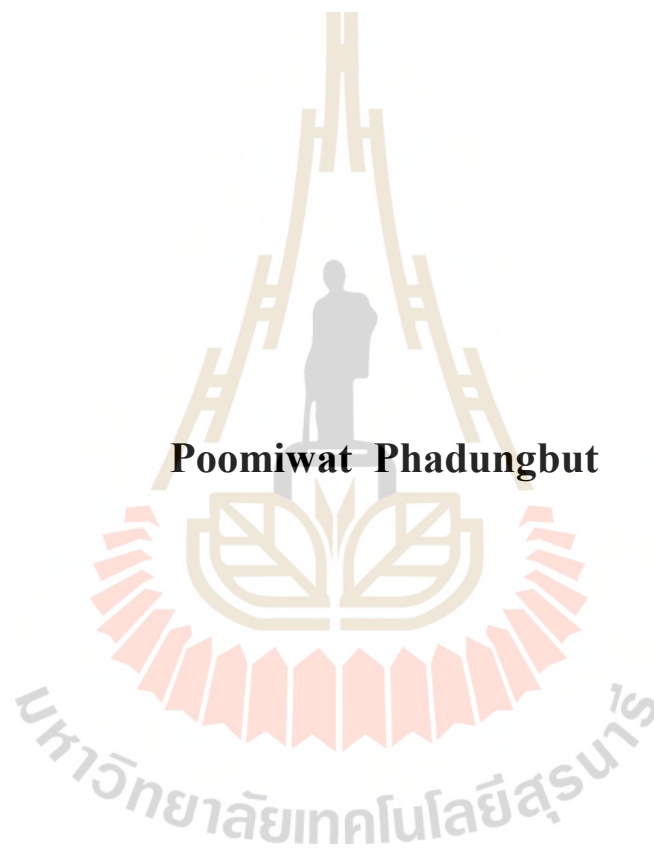# COMPUTER SIMULATION OF POROUS CARBON STRUCTURES AND GAS ADSORPTION UNDER SUBCRITICAL AND SUPERCRITICAL CONDITIONS

Poomiwat Phadungbut

A Thesis Submitted in Partial Fulfillment of the Requirements for the

Degree of Doctor of Philosophy in Chemical Engineering

Suranaree University of Technology

Academic Year 2015

การจำลองทางคอมพิวเตอร์ของโครงสร้างคาร์บอนพรุนและการดูดซับก๊าซ
ภายใต้สภาวะกึ่งวิกฤตและเหนือวิกฤต

นายภูมิวัต ผดุงบุตร

วิทยานิพนธ์นี้เป็นส่วนหนึ่งของการศึกษาตามหลักสูตรปริญญาวิศวกรรมศาสตรดุษฎีบัณฑิต
สาขาวิชาวิศวกรรมเคมี
มหาวิทยาลัยเทคโนโลยีสุรนารี
ปีการศึกษา 2558

COMPUTER SIMULATION OF POROUS CARBON

STRUCTURES AND GAS ADSORPTION UNDER

SUBCRITICAL AND SUPERCRITICAL CONDITIONS

Suranaree University of Technology has approved this thesis submitted in partial fulfillment of the requirements for the Degree of Doctor of Philosophy.

Thesis Examining Committee

_____

(Asst. Prof. Dr. Atichat Wongkoblap)

Chairperson

_____

(Prof. Dr. Chaiyot Tangsathitkulchai)

Member (Thesis Advisor)

_____

(Dr. Terasut Sookkumnerd)

Member

_____

(Asst. Prof. Dr. Boris Golman)

Member

_____

(Asst. Prof. Dr. Ratanawan Kiattikomol)

Member

_____   _____

(Prof. Dr. Sukit Limpijumnong)   (Assoc. Prof. Flt. Lt. Dr. Kontorn Chamniprasart)

Vice Rector for Academic Affairs   Dean of Institute of Engineering

and Innovation

ภูมิวัต ผดุงบุตร : การจำลองทางคอมพิวเตอร์ของโครงสร้างคาร์บอนพรุนและการดูดซับ
ก๊าซภายใต้สภาวะกึ่งวิกฤตและเหนือวิกฤต (COMPUTER SIMULATION
OF POROUS CARBON STRUCTURES AND GAS ADSORPTION UNDER
SUBCRITICAL AND SUPERCRITICAL CONDITIONS) อาจารย์ที่ปรึกษา :
ศาสตราจารย์ ดร.ชัยยศ ตั้งสถิตย์กุลชัย, 164 หน้า.

วิทยานิพนธ์นี้ศึกษาการจำลองโครงสร้างคาร์บอนพรุนและมุมมองใหม่เกี่ยวกับพฤติกรรม
การดูดซับก๊าซที่อุณหภูมิต่างๆโดยใช้แบบจำลองมอนติคาร์โล (MC) งานวิจัยนี้สามารถแบ่งออกได้
เป็นสามส่วน โดยในส่วนแรกทำการศึกษาการสร้างโครงสร้างคาร์บอนและพัฒนาวิธีการหา
คุณลักษณะของโครงสร้างรูพรุนด้วยวิธีการจำลองทางคอมพิวเตอร์ โดยในขั้นแรกทำการทดสอบ
วิธีที่นำเสนอกับแบบจำลองอย่างง่ายที่มีรูปร่างแน่นอน เช่น รูพรุนทรงกระบอก และรูพรุนแผ่น
ขนาน เป็นต้น จากนั้นขยายไปใช้กับแบบจำลองคาร์บอนพรุนที่มีความซับซ้อนของโครงสร้างมาก
ขึ้น จากการศึกษาพบว่า สมบัติรูพรุน และ ไอโซเทิร์มการดูดซับของคาร์บอนพรุนที่สร้างขึ้น
สอดคล้องกับผลของถ่านกัมมันต์จริงที่เตรียมจากเม็ดลำไย
ในส่วนที่สอง ได้ศึกษาการจำลองการเกิดวงรอบฮิสเทอรีซิส (Hysteresis) ของการดูดซับ
ก๊าซอาร์กอนที่สภาวะกึ่งวิกฤติ บนพื้นผิวกราฟีนและรูพรุนอย่างง่ายทั้งแบบช่องแคบ แบบ
ทรงกระบอก และแบบทรงกลม โดยการใช้แบบจำลองแบบแกรนด์คาร์โนนิคัล (GCE) และคาร์โน
นิคัลแบบสองปริมาตร (MCE) เพื่อค้นหา สภาวะเสถียร กึ่งเสถียร และไม่เสถียรภายในรูพรุน
ดังกล่าว จากการศึกษาพบว่าจุดเริ่มต้นของการเกิดวงฮิสเทอรีซิสเป็นผลมาจากการเปลี่ยนเฟส การ
เกิดผิวคลื่นก่อนการควบแน่น และการจัดโครงสร้างของสารถูกดูดซับภายในรูพรุน
ในส่วนสุดท้ายของวิทยานิพนธ์ ได้นำเสนอวิธีใหม่ในการหาปริมาณการดูดซับสัมบูรณ์ที่
สภาวะเหนือวิกฤตโดยได้แนวคิดจากการหาบริเวณช่องว่างที่บรรจุโมเลกุลของก๊าซได้สำเร็จ วิธีนี้
สามารถอธิบายการดูดซับของก๊าซอาร์กอนบนพื้นผิวกราฟีน ได้เป็นอย่างดี จากการศึกษาพบว่าที่
ความดันและอุณหภูมิเหนือจุดวิกฤต ในเฟสดูดซับจะมีชั้นดูดซับของอาร์กอนไม่เกิน 2 ชั้น และเฟส
ดูดซับจะมีสภาวะเป็นของเหลวเสมือน

สาขาวิชาวิศวกรรมเคมี   ลายมือชื่อนักศึกษา _____
ปีการศึกษา 2558   ลายมือชื่ออาจารย์ที่ปรึกษา _____

POOMIWAT PHADUNGBUT : COMPUTER SIMULATION OF POROUS

CARBON STRUCTURES AND GAS ADSORPTION UNDER SUBCRITICAL

AND SUPERCRITICAL CONDITIONS. THESIS ADVISOR : PROF.
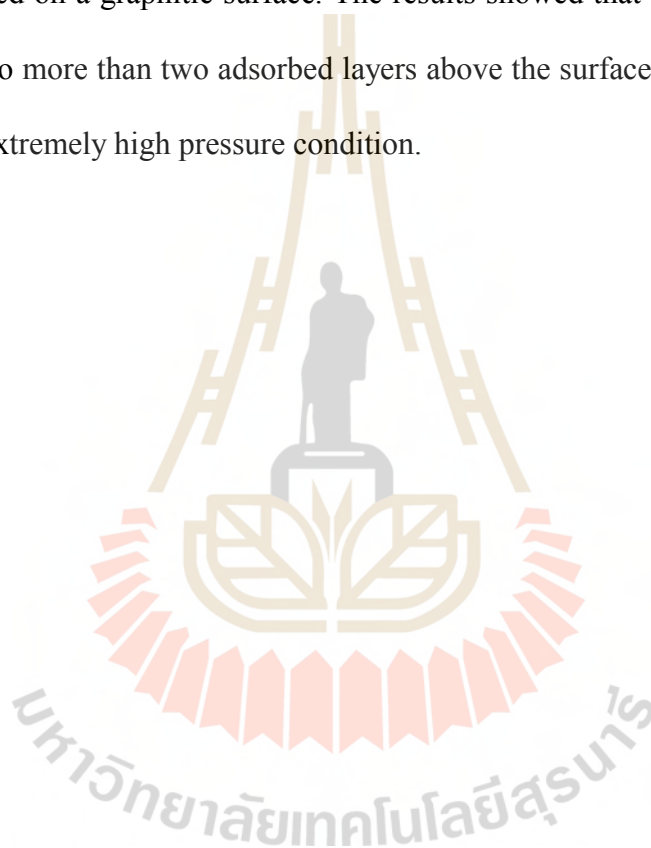
CHAIYOT TANGSATHITKULCHAI, Ph.D., 164 PP.

POROUS CARBON/ADSORPTION/

CHARACTERIZATION/MONTE CARLO SIMULATION

This thesis is concerned with the modeling of porous carbon structure and
novel aspects of gas adsorption behavior over a wide range of conditions using Monte
Carlo (MC) simulation. The thesis was divided into three parts. The first part was
focused on the creation of simulated porous carbon and the development of pore
characterization technique based on the concept of accessibility using computer
simulation. This proposed characterization method was first validated with several
simple pore models such as cylindrical and slit pores and extended to a more complex
porous carbon model. The result indicated that both the computed structural
properties and adsorption isotherms of the simulated porous carbon were in
qualitative agreement with those of longan seed-derived activated carbon, thus
proving the potential of this new pore characterization technique.

In the second part, a smooth graphitic surface and simple pore models, slit,
cylindrical and spherical pores, were used to study the microscopic behaviors of
hysteresis loop for argon adsorption under subcritical conditions. Grand canonical
(GCE) and Meso-canonical (MCE) ensembles were applied to search for the stable,
metastable and unstable states in the corresponding pores. It can be summarized that

the phase transition, the undulating interface at the onset of condensation and the restructuring of adsorbate are the microscopic origin of hysteresis loops.

For the final part, the novel approach based on the concept of fraction of successful insertion was proposed to determine absolute adsorbed amount under supercritical conditions. The method has well described the adsorption mechanism of argon adsorbed on a graphitic surface. The results showed that the adsorbed phase is confined to no more than two adsorbed layers above the surface and it is a liquid-like state at this extremely high pressure condition.

School of <u>Chemical Engineering</u>   Student's Signature _____

Academic Year 2015   Advisor's Signature _____

ACKNOWLEDGEMENTS

In addition, I would also like to express my appreciation, Dr. Nikom Klomkliang, who has pulled me out from the depth of ignorance and shared his experience in molecular simulation and adsorption.

For the friendship, kind help, sharing good and bad moments during my PhD time I thank the members in the UQ group they are: Ms. Yonghong Zeng, Mr. Shiliang Johnathan Tan and Ms. Luisa Prasetyo. I would like to thank the former members in the UQ group, Assoc. Prof. Dr. Toshihide Horikawa, Dr. Chunyan Fan, Dr. Luis F. Herrera and Dr. Van Thuy Nguyen, for their collaboration for each article.

Finally, I would like to dedicate my Ph.D. thesis and publications to my parents and grandparents who always provide me an endless love and encourage me the strength when I was weak.

Poomiwat Phadungbut

TABLE OF CONTENTS

Page

TABLE OF CONTENTS (Continued)

TABLE OF CONTENTS (Continued)

TABLE OF CONTENTS (Continued)

TABLE OF CONTENTS (Continued)

TABLE OF CONTENTS (Continued)

TABLE OF CONTENTS (Continued)

LIST OF TABLES

LIST OF FIGURES

LIST OF FIGURES (Continued)

LIST OF FIGURES (Continued)

LIST OF FIGURES (Continued)

LIST OF FIGURES (Continued)

LIST OF FIGURES (Continued)

LIST OF FIGURES (Continued)

LIST OF FIGURES (Continued)

LIST OF FIGURES (Continued)

LIST OF FIGURES (Continued)

LIST OF FIGURES (Continued)

LIST OF FIGURES (Continued)

CHAPTER I

INTRODUCTION

1.1 Rationale of the Study

Porous carbons find widespread applications in industries for purification and separation of gas and liquid mixtures and as catalyst supports because of their excellent properties of large surface area, ease of surface chemistry manipulation and tunable pore size distribution (Gregg and Sing, 1982). In principle, the microstructure of porous carbons can be tailored to suit a given application by judicious choosing of the raw material and its preparation procedure (Tao et al., 2011; Lee et al., 2006), though the detailed structure at microscopic level is still not fully understood. The microscopic observations extracted from X-ray diffraction experiment, transmission electron microscopy and elemental analysis (Marsh and Reinoso, 2006; Dumont et al., 2002; Cuesta et al., 1994; Jayabalan et al., 2009; Azuma, 1998; Bernard et al., 2010) also reveal some structural image and composition of the porous carbon but what is lacking is perhaps the information on pore characteristics which are quite complex concerning the connectivity of various pore sizes. Generally, the structure of porous carbons has been modeled by simple pore models, such as slit and cylindrical pores, but these are not capable of incorporating many features of porous carbons including the non-graphitizing nature, the presence of heteroatoms and pore connectivity (Jagiello and Olivie, 2013; Silvino et al., 2013; Neimark et al., 2009; Bhatia; 2002). Therefore, appropriate molecular models need to be developed to simulate the actual

structures of porous carbon in order that a precise study of adsorption behavior can be closely studied.

The development of computer technology and molecular simulations, such as Monte Carlo simulation (MC), Molecular Dynamics (MD) and Density Functional Theory (DFT), have been effectively used for the study of the adsorption mechanisms. They do not only provide the microscopic adsorption phenomena, but also reduce the experimentation effort for the prediction of adsorption behaviors (Allen and Tildesley, 1989; Frenkel and Smit; 2002). Among these simulation techniques, MC is most commonly used method for the equilibrium study because of its powerful ability to search for the metastable state.

Among many experimental methods that are available, the most practical ways for pore characterization is gas adsorption technique because it is inexpensive and simple experimental requirement. A physical adsorption isotherm derived from the measurement provides the adsorbed amount as a function of the relative pressure. The structural parameters that can be derived from the analysis of the adsorption isotherm are the total pore volume, surface area and pore size distribution. The characterization of these properties is usually carried out with simple gases, such as argon and nitrogen at their boiling points and carbon dioxide at 273 K or ambient temperature. Even when atomistic configuration of porous material is known, it is still desirable to obtain the pore volume distribution. Many researchers proposed the consistent methodologies by establishing their own definition of pore size, however, those proposed techniques spent a lot of computational time. In this work, we improved the computation efficiency to obtain structural properties for known configurations of porous carbons.

In addition to the pore characteristics, it is also necessary to understand the thermodynamic equilibrium of gas adsorbed in porous carbons over a range of temperature. At temperatures below the critical temperature of a pure bulk gas, a significant feature of adsorption isotherms is the hysteresis loop, which associates the condensation and evaporation of fluid within the confined space due to distinct cohesiveness factor (Horikawa et al., 2011). Hysteresis was firstly observed in 1897 by van Bemmelen in the experimental adsorption of water in silica (Everett, 1967). The existence of hysteresis is complex functions of pore shape, surface chemistry, adsorbate and temperature (Thommes, 2004). This work will search for the microscopic reason describing the existence of hysteresis.

Physical adsorption of gases under supercritical condition is of great interest and controversial topic in the area of energy storage of natural gas and hydrogen (Bhatia and Myers, 2006; Lozano-Castello et al., 2002; Zhou et al., 2000). The theoretical studies of supercritical adsorption would lead to the better understanding of the various behaviors observed experimentally and computationally; for example, the maximum of excess adsorbed amount exhibiting in the adsorption isotherm and the boundary demarcating between gas and adsorbed phases. For the first time in the literature, this work will reveal the physics of gas adsorption under supercritical conditions by means of computer simulation.

1.2 Research Objectives

The aim of this thesis is to study the construction, characterization and gas adsorption behavior of porous carbons by using computer simulation. This is achieved through the following specific objectives:

1. To develop and refine a method for determining structural characteristics of atomistic models of porous carbon from simple to complex pore models.

2. To study the microscopic behavior of argon adsorbed on a graphitic surface and in slit pores with various pore widths at temperatures below the 2D-critical temperature.

3. To extend the undulation theory for investigating the existence of undulating interface and describing the capillary condensation in cylindrical and spherical pores.

4. To investigate the microscopic origin of hysteresis loop in slit pores with different topologies by means of Meso-canonical Monte Carlo simulation.

5. To introduce a novel approach for the determination of absolute adsorbed amount with argon adsorption on a graphitic surface under supercritical condition, based on the concept of fraction of success.

1.3   Thesis Outlines

The following chapters present the accomplishment of the specific objectives of this thesis work which help to better understand the computer simulation of porous carbons and gas adsorption under subcritical and supercritical conditions.

In Chapter 2, literature review concerning the thesis topic is presented including the relevant concepts and simulation methods as tools for study of adsorption and typical porous characterization to provide on the basic knowledge of computer simulation. In Chapter 3, the details about the development of simulated porous carbons and pore characterization, whose structure is known, are proposed. It

also illustrates the determination of textural properties from the simple pore models to the complex carbon structure. In Chapter 4, the analyses of 2D-transition of adsorbed monolayer of argon on graphite surface and in slit-like pores having various pore widths are introduced to understand microscopically the hysteresis loop under subcritical conditions. Chapter 5 extends the undulation theory to describe capillary condensation in cylindrical and spherical pores under subcritical conditions. Chapter 6 presents the simulation study of the microscopic origin of hysteresis in slit-like pores with open end, one end closed and both end closed under subcritical conditions. Chapter 7, a new method is proposed for the determination of absolute adsorbed amount for argon adsorption on graphite under supercritical conditions based on the concept of fraction of success. Finally, Chapter 8 draws conclusions and presents recommendations, as well as outlining the scope for future work in this area. Total number of publications is listed in the APPENDIX.

1.4   References

Allen, M. P. and Tildesley, D. J. (1989) **Computer simulation of liquids**. Oxford University Press: Oxford.

Azuma, H. (1998). A new structural model for non-graphiting carbons. **Journal of Applied Crystal**. 31: 910-916.

Bhatia, S. K. (2002). Density functional theory analysis of the influence of pore wall heterogeneity on adsorption in carbons. **Langmuir**. 18: 6845-6856.

Bhatia, S. K. and Myers, A. L. (2006). Optimum conditions for adsorptive storage. **Langmuir**. 22: 1688-1700.

Cuesta, A., Dhamelincourt, P. and Laureyns, J. (1994). Raman microprobe studies on carbon materials. **Carbon**. 32: 1523-1532.

Dumont, M., Chollon, G., Dourges, M. A., Pailler, R., Bourrat, X. and Naslain R. (2002). **Carbon**. 38: 183-197.

Everett, D. H. (1967), **Adsorption hysteresis**. Marcel Dekkar: New York. 1055-1110.

Frenkel, D. and Smit, B. (2002). **Understanding molecular simulation: from algorithms to applications**. Academic Press: San Diego.

Gregg, S. J. and Sing, K. S. W. (1982). **Adsorption, surface area and porosity**. Academic Press: New York.

Horikawa, T., Do, D. D. and Nicholson, D. (2011). Capillary condensation of adsorbates in porous materials. **Advances in Colloid and Interface Science**. 169: 40-58.

Jagiello, J. and Olivier, J. P. (2013). Carbon slit pore model incorporating surface energetical heterogeneity and geometrical corrugation. **Adsorption**. 19: 777-783.

Jayabalan, T., Pré, P., Héquet, V., Le Cloirec, P. and Rouzaud, J. N. (2009) Material properties influencing the oxidation and ignition reactivity of activated carbons: thermal analysis, HRTEM study and statistical modeling. **Energy Fuels**. 32: 4051-4058.

Lee, J., Kim J. and Hyeon, T. (2006). Recent progress in the synthesis of porous carbon materials. **Advanced Materials**, 18, 2073-2094.

Lozano-Castello, D., Alcaniz-Monge, J., de la Casa-Lillo, M. A., Cazorla-Amoros, D. and Linares-Solano, A. (2002) Advances in the study of methane storage in porous carbonaceous materials. **Fuel**. 81: 1777-1803.

Marsh, H. and Reisono, F. R. (2006). **Activated carbon**. Elsevier.

Neimark, A. V., Lin, Y., Ravikovitch, P. I. and Thommes, M. (2009). Quenched solid density functional theory and pore size analysis of micro-mesoporous carbons. **Carbon**. 47: 1617-1628.

Silvino, P. R. G., Goncalves, D. V., Goncalves, R. V., de Lucena, S. M. P. and Azevedo, D. C. Z. (2013). Strategies to improve pore-size distribution characterization of activated carbon using CO_2 and N_2 isotherms: volume regularization and etched slit models. **Adsorption Science and Technology**. 31: 263-274.

Tao, Y., Endo, M., Inagaki, M. and Kaneko, K. (2011). Recent progress in the synthesis and applications of nanoporous carbon films. **Journal of Material Chemistry**. 21: 313-323.

Thommes, M. (2004). **Physical adsorption characterization of ordered and amorphous mesoporous materials**. Imperial College Press: New Jersey. 317-364.

CHAPTER II

GENERAL BACKGROUND

2.1 Porous Carbons and Their Models

Porous carbons are usually prepared from raw carbonaceous materials via two steps: carbonization and activation. During the carbonization, most of the non-carbon elements of the raw materials are removed via the pyrolysis process at temperatures below 800°C (Yuan et al., 2013). The solid residue left after carbonization is a carbon skeleton with low porosity referred to as char. To increase the porosity of char, it is further gasified to produce activated carbon using oxidizing gases such as steam, CO_2, or air, or it can be chemically activated with various inorganic acids or bases or alkali salts (Mahadik-Khanolkar et al., 2014). Activated carbon is commonly used for a wide range of industrial processes due to its large internal surface area developed in the form of micro- and mesopore (Choi et al., 2009). The pore structure and surface chemistry of activated carbon depends chiefly on the precursor, the carbonization-activation conditions (time and temperature) and the amount of activating agents used (Yue et al., 2006; Reinoso et al., 2000; Chang et al., 2000; Teng and Lin; 1998).

Structurally, porous carbons including activated carbon differ from graphite in that it has a microcrystalline structure of graphite-like layers arranged and connected in a random manner (Pré et al., 2013). This low degree of graphitization creates a high degree of porosity which gives increased adsorption capacity. Consequently, highly graphitized carbons with homogeneous surface are less attractive than amorphous

carbons. Due to the significance of porous carbon in many applications, attempts have been made by several researchers to model a porous carbon with structure and adsorption properties resemble those of real carbon at that detailed study on adsorption behavior can be made by a computer.

In 1951, Franklin (1951) proposed the models for non-graphitizing and graphitized carbons, from which the basic units consist of an assembly of microcrystallites containing 2-5 layers of graphene sheets. An illustration of Franklin models is shown in Figure 2.1.

(a)   (b)
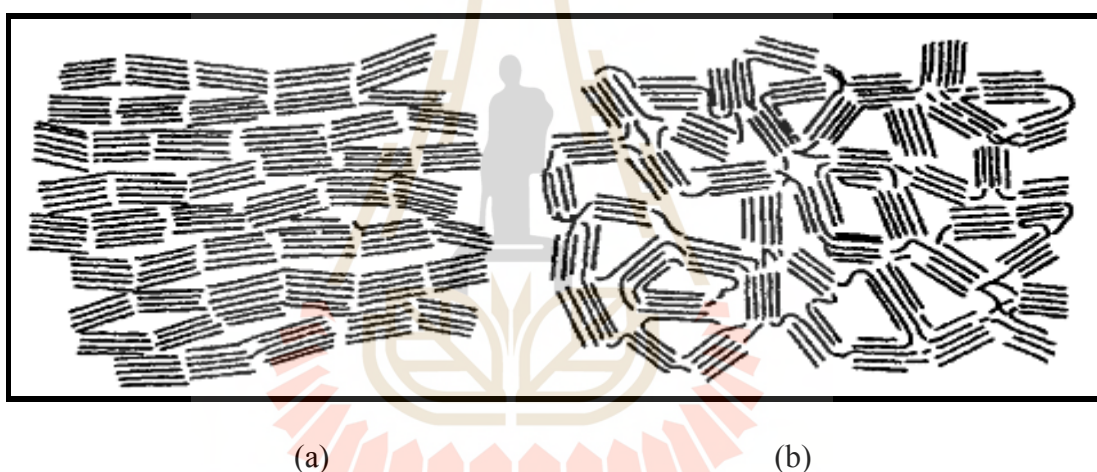
Figure 2.1 Schematic diagrams of (a) graphitizing and (b) non-graphitizing carbons.

Porosity in porous carbon is the internal space developed during the carbonization and/or activation processes within the structure of the original precursor. At the microscopic level, porosity in porous carbon is the molecular void within the network of carbon atoms and between the carbon atoms (Banhart et al., 2011). Thus, it is important to be able to model the structure of the carbon network which is required for interpreting the experimental data and to aid in the preparation

and selection of carbon adsorbents for specific applications (Nguyen et al., 2008; Palmer and Gubbins, 2012; Wang et al., 2015; Bandosz et al., 2003). There are two general approaches to create a molecular model of porous carbon, mimetic simulation and reconstruction method.

Mimetic simulation involves the development of a simulation strategy that mimics the synthetic process used to produce activated carbon in the laboratory. This method has the advantages of providing insight into the synthesis mechanism and generate a unique molecular structure based on the carbonization and activation condition. The *ab initio* and semiempirical quantum mechanical methods are illustrations of mimetic simulation methods.

Another approach is the reconstruction method which models the porous carbon by matching its properties with experimental data such as X-ray and neutron diffraction data or experimental adsorption isotherm. Transmission electron microscopy (TEM) images of the porous carbons are the initial model to create more realistic reconstruction methods including fringe lengths, stacking degree and orientations. The atomic structure of a single carbon crystal is hexagonal closed-packed unit as shown in Figure 2.2 (March and Reisono, 2006). Within the hexagonal graphite, the layers of hexagonal arrangements of carbon atoms are described as graphene layers. The distance between layers is 0.355 nm, and the distance between C-C bonds is 0.142 nm. The reconstruction method is detailed as follows (Radovic, 2003).
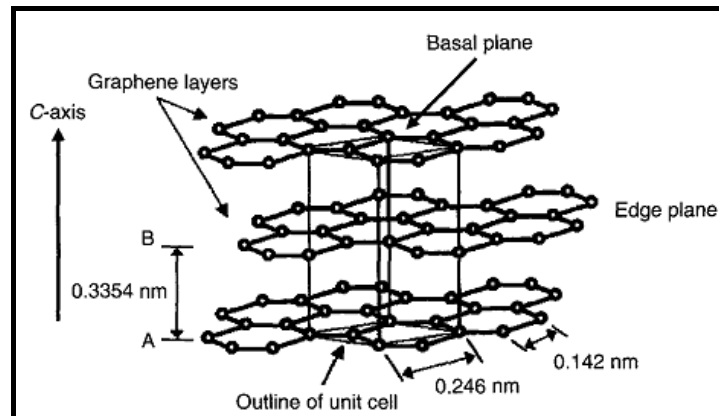
Figure 2.2 The structure of hexagonal graphite for a single microcrystallite.

2.1.1   Simple pore models

Slit and cylindrical pore models (Figure 2.3), consisting of smooth graphene layers, are the simplest geometrical models which are generally used to obtain the pore size distribution of the unknown structure of porous materials, such as activated carbon and carbon nanotubes. These models are based on simplifications of the complex structure observed from TEM images. By assuming the pore shape inside porous materials having the same pore geometry, it is thus lack of pore connectivity and heterogeneous surface of non-graphitized carbon structure. Thus, more realistic models have been attempted instead.
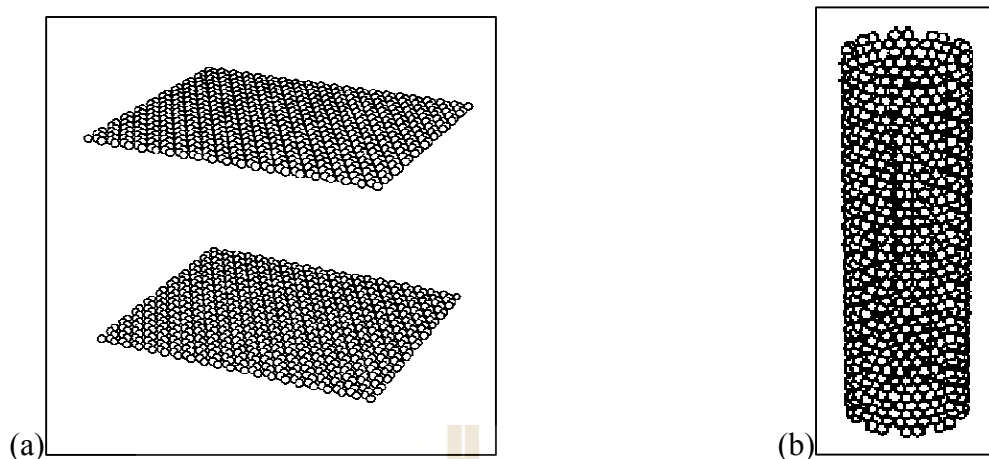
Figure 2.3 (a) Slit pore and (b) cylindrical pore models.

2.1.2   The random etched graphite model

This model presented in Figure 2.4 has been developed to account for surface heterogeneity. The etched carbon atoms are randomly removed from the inner surfaces in which probe molecules can be accessible inside the pore region. Although this model has been proposed to represent the geometrical heterogeneity of the surface, it is lack of variations in pore shape or connectivity. However, this model is initially powerful to study the surface heterogeneity on porous carbon model because it provides a realistically broader pore size distribution than the uniform slit pore model.
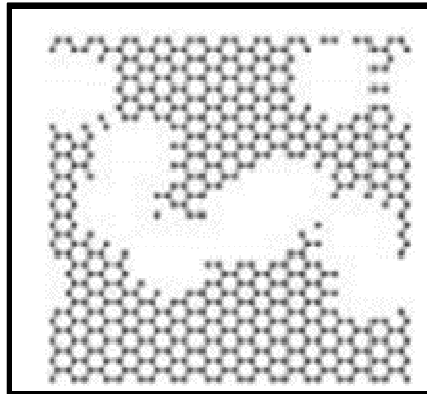
Figure 2.4 The randomly etched graphite model for one graphene layer.

2.1.3 Virtual porous carbons model

Biggs and Agarwal (1994) proposed the VPC as shown in Figure 2.5. VPCs are groups of aligned polyaromatic molecules known as basic structural units (BSUs) which are aggregated in regions that present local molecular orientation (LMO). VPC void is generated by random removing of graphene layer based on a specified porosity of the real structure. The advantage of VPC is that porous properties such as pore size distribution can be easily controlled and characterized. However, the VPC model does not give the information on internal pore connectivity.
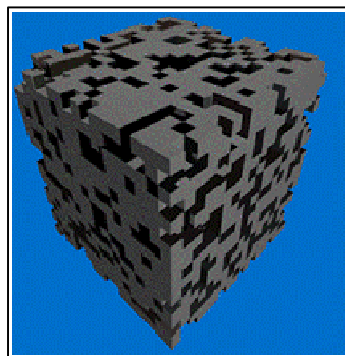
Figure 2.5 The virtual porous carbons models.

2.1.4   The reverse Monte Carlo model

The reverse Monte Carlo (RMC) model creates the microstructure of activated carbon using experimental structural data (Thomson and Gubbins, 2000). The radial distribution function (RDF) is defined as the histogram of probability of finding a carbon atom at a distance of radius away from the reference coordinates. RDF can be obtained experimentally through X-ray diffraction data and then applied for generating activated carbon structure. The advantage of RMC model is its incorporation of experimental structural data into the simulation model. However, RMC method is particularly difficult for creating mesoporous and macroporous structure. For example in Figure 2.6, the maximum length for RDF is 30 Å which resides in the range of micro- and mesopore sizes. As a result, RMC is more appropriate for creating microporous structure than for other larger pore sizes.

(a)   (b)
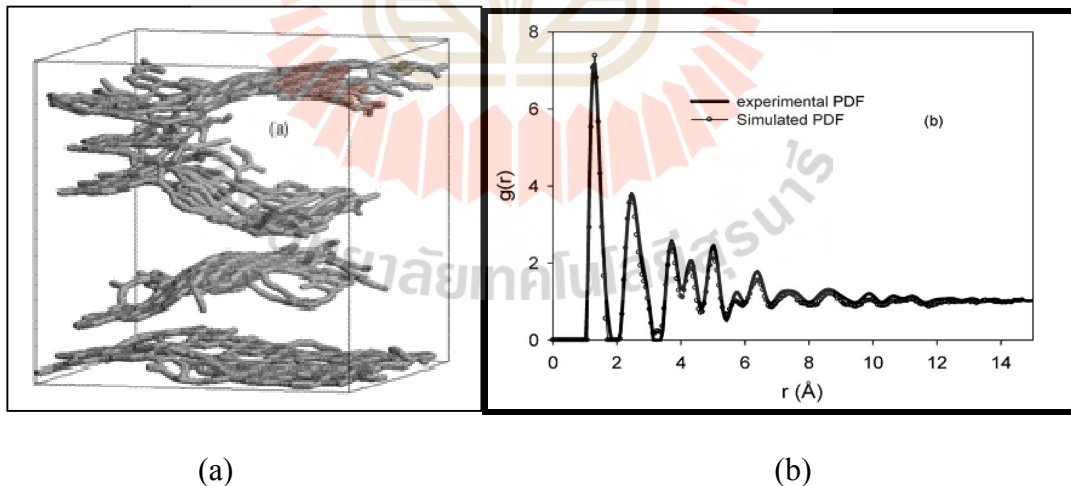
Figure 2.6   (a) Porous carbon model obtained from the reverse Monte Carlo by matching with (b) the experimental radial distribution function.

2.2   Characteristics of Gas Adsorption and Hysteresis

Gas adsorption has been commonly used to characterize the porous and non-porous materials because it is relatively easy to carry out and available in most laboratories. The adsorption is defined as the binding of molecules, atoms or ions to a surface. In principle, the fluid molecule to be adsorbed is called adsorbate, while the solid surface is referred to as adsorbent. For non-porous materials like a graphitized thermal carbon black, the adsorption feature is molecular layering onto a surface. However, for porous material, the molecular filling process takes place when the pore cross section, relative to the molecular size of adsorbate, is narrow enough; otherwise, the capillary condensation accompanied by hysteresis will occur when the pore size is large than a threshold pore size. The width of hysteresis loop decreases and then disappears when it rises to the critical hysteresis temperature.

The IUPAC classification of adsorption isotherms firstly reported in 1985 (Sing et al., 1985) were categorized into six groups. Recently, in 2015, the classification is newly refined to be related to peculiar pore structure as shown in Figure 2.7 (Thommes et al, 2015). The description of each isotherm is detailed as follows.
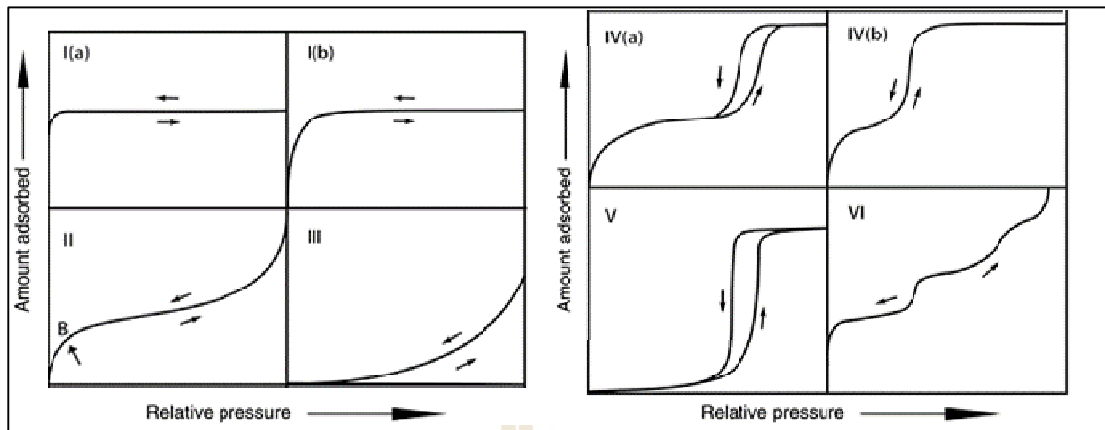
Figure 2.7 The IUPAC classification of adsorption isotherms in 2015.

Type I(a): This isotherm is found in microporous materials with narrow micropore size distribution.

Type I(b): This isotherm is typified by an adsorbent with broader micropore size distribution.

Type II: This isotherm is found for most gases favorably adsorbed on nonporous or macroporous materials with multi-layering adsorption onto the adsorbent surface.

Type III: This isotherm shows a weak adsorbent-adsorbate. The adsorbate is initially adsorbed on the strong site as a cluster, for example, the attachment of water molecules at the surface functional groups of a carbon black, followed by a form of water cluster at high adsorption loading.

Type IV(a): This type is similar to the Type II but it exhibits the hysteresis loop. This occurs when the pore width is large enough to accommodate the adsorbate into the denser phase.

Type IV(b): This isotherm is formed when the pore width is small and the one side of pore is closed.

Type V: This is similar to the Type III but it occurs with porous materials are considered. The cluster formation is followed by penetration into the pore.

Type VI: This type is representative of layer-by-layer adsorption on a uniform surface.

In 1967, the four types of hysteresis loop were firstly proposed by Everett (Everett, 1967) based on the pressure range of boundaries of the hysteresis loop. In 1972, De Boer (1972) classified the hysteresis loop into five types, A, B, C, D and E. In 1985, the IUPAC classification shows four types (H1, H2, H3 and H4) which were commonly observed by the experimental isotherms with disordered porous materials. Only two types of De Boer classification are similar to the IUPAC one: Type A = H1 and Type E = Type H2. Nowadays, the synthesis of highly ordered mesoporous solids has currently developed understanding the capillary condensation and pore characterization. In the past decade, many different hysteresis loops have been also observed, especially Type C. Thus, the novel IUPAC classification of hysteresis loops shown in Figure 2.8 (Thommes et al., 2015) is extended and categorized into six types.
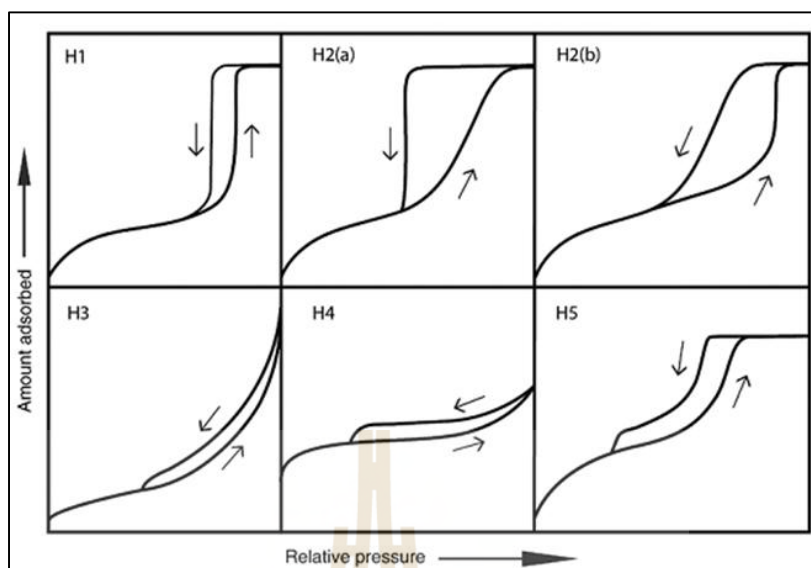
Figure 2.8 The IUPAC classification of hysteresis loops in 2015.

Type H1: This is found in a narrow range of mesopore size distribution, such as MCM-41 and SBA-15. The open-ended ink-bottle pore is normally modeled to explain the mechanism underlying this type of hysteresis loop.

Type H2(a): The loop shape is based on the network percolation theory, and linked to the ink-bottle model. The evaporation can be contributed to pore blocking and cavitation in a narrow pore neck like SBA-16.

Type H2(b): It is the same as Type H2(a) but the evaporation is only governed by pore blocking in porous materials having large pore neck, such as mesoporous ordered silicas after hydrothermal treatment.

Type H3: the adsorption branch resembles a Type II according to the adsorption isotherm and the lower closure point is located at the limit of tensile strength of adsorbate. This loop is associated with solids containing non-rigid plate-like structure and pore network consisting of macropores.

Type H4: The loop is similar to Type H3 but the pore network connects to be a narrower micropore and mesopore size distributions. The adsorption branch is a combination of Types I and II. This is commonly found in activated carbon when nitrogen gas at its boiling point is used.

Type H5: This is observed when the pore structure contains both open and partially blocked mesopores.

2.3   Monte Carlo Simulation for Adsorption

Monte Carlo (MC) simulation is a numerical method which employs random sampling to arrive at an approximate solution of a given problem. The Metropolis algorithm is practically used to carry out the simulation in various ensembles that are mostly used in adsorption, and they are briefly described here. Full details can be found in Frenkel and Smith (2002).

2.3.1   Canonical Ensemble (NVT)

In this ensemble, the number of particles, temperature and volume of simulation box are constant, and thermodynamic properties derived from a simulation are pressure and chemical potential. The brief procedure of simulation with canonical ensemble is as follows:

1. Set the size of the simulation box.

2. Insert a number of particles, N, randomly in the simulation box.

3. Calculate the configuration energy of the system, U_1, then choose a particle randomly.

4. Move the selected particle from the initial position to a random position. This is called as local displacement move.

5. Calculate the new configuration energy of the system, U_2.

6. The criteria to accept or reject the movement is based on the following probability;

$$P = \min\left(1, \exp\left(-\frac{(U_2 - U_1)}{k_B T}\right)\right) \tag{2.1}$$

7. If the new configuration has been accepted, then updating the position of the particle and the energy of the system; otherwise, the old configuration is unchanged.

8. Repeat the process until the system reaches the equilibrium state.

2.3.2 Grand canonical ensemble (GCE)

The grand canonical ensemble is commonly used in adsorption studies. In this ensemble, the temperature, volume and chemical potential of surrounding bulk gas (μ) are fixed. Apart from the local displacement described in earlier section, the insertion and deletion of a particle is additional movement in GCE.

An insertion step is conducted by inserting a particle from the surrounding at a random position within a simulation box. The probability of accepting this insertion is given by:

$$P = \min\left(1, \frac{V}{\Lambda^3 (N+1)} \exp\left(\frac{\mu - U_2 + U_1}{k_B T}\right)\right) \tag{2.2}$$

where N is a number of particles in the simulation box, U_1 and U_2 is the energy of the system before and after the insertion and Λ is de Broglie wavelength. Similar to the

local displacement, if the insertion is accepted, the configuration of the system will be updated.

The probability of accepting the deletion of a randomly selected particle in the simulation box is given by:

$$P = \min\left(1, \frac{\Lambda^3 N}{V} \exp\left(-\frac{\mu + U_2 - U_1}{k_B T}\right)\right) \tag{2.3}$$

In GCE simulation, the system must have equal probability for the insertion and deletion to ensure the detailed balance. For the GCE simulation conducted in this work, the equal probability for local displacement, insertion and deletion in each cycle is applied for simulating the gas adsorption.

2.3.3 Meso-canonical ensemble (MCE)

Experimentally, the volumetric method is commonly used to obtain isotherms for gas adsorption. To simulate the operation of an actual volumetric experiment, a method has been introduced in which the adsorbent cell (left box) is attached to a reservoir of finite volume (right box) as shown in Figure 2.9a. The method is akin to the gauge cell Monte Carlo method (Neimark and Vishnyakov, 2000). It has in common the use of a finite dosing reservoir, which suppresses fluctuations so that the van der Waals (vdW) loop in the isotherm can be traced. The procedure of this ensemble is as follows. A fixed number of molecules, N, is supplied to the gas reservoir (Figure 2.9b) and then distribute themselves between the adsorption cell and the dosing reservoir (Figure 2.9c) until the equilibrium is established. Therefore, besides the local displacement within the same box, the global

displacement is used to exchange the particle into another box. The probability of accepting this global displacement is given by:

$$P = \min\left\{1, \exp\left(-\frac{\left(\Delta U_{ins} + \Delta U_{del} + k_B T \ln\left(\frac{V_{del}\left(N_{ins}+1\right)}{V_{ins}N_{del}}\right)\right)}{k_B T}\right)\right\} \qquad (2.4)$$

where U_{ins}, V_{ins}, N_{ins}; U_{del}, V_{del}, N_{del} are the configurational energy change, volume and number of particles of the "insert" and "delete" box, respectively.

The advantage of this ensemble compared to the NVT ensemble is its ability to compute equilibrium pressure and chemical potential with the absence of solid-fluid interaction in the dosing cell.
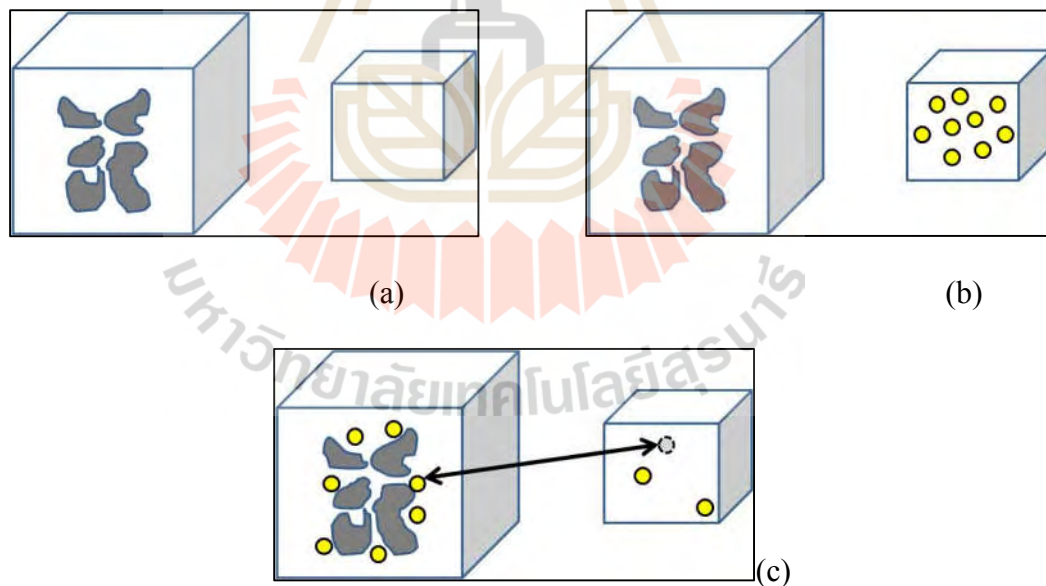
Figure 2.9 Schematic diagrams of meso-canonical ensemble.

2.4 Fluid-Fluid Interaction

To describe the fluid-fluid interaction energy, we used the following 12-6 Lennard Jones (LJ) equation:

$$\varphi_{FF}(r) = 4\varepsilon_{FF}\left[\left(\frac{\sigma_{FF}}{r}\right)^{12} - \left(\frac{\sigma_{FF}}{r}\right)^{6}\right] \tag{2.5}$$

where φ_{FF} is the LJ potential energy, σ_{FF} is the collision diameter, $_{FF}$ is the energy well-depth of the interaction energy and r is the distance between two adsorbate atoms. The LJ plot of argon-argon interaction is illustrated in Figure 2.10.
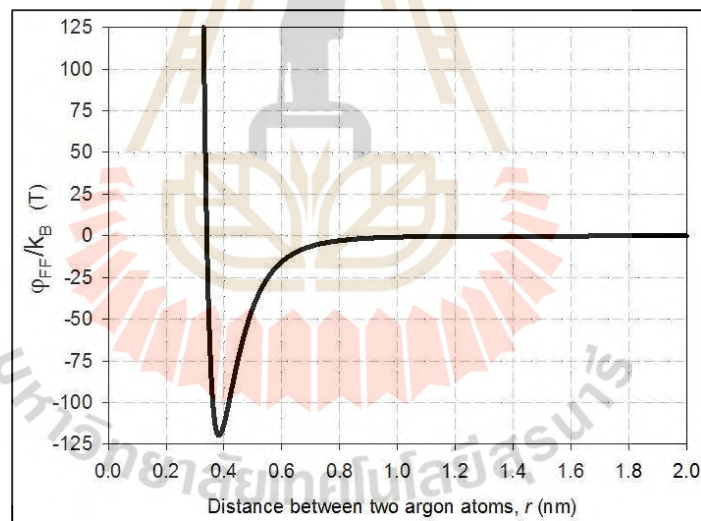
Figure 2.10 Lennard-Jone potential profile of two argon atoms.

For polyatomic molecule with dispersive and partial charge sites, the interaction energy between two molecules is given by sum of the LJ and Coulomb interactions as shown below:

$$\varphi_{ij}\left(r\right) = \sum_{a=1}^{A}\sum_{b=1}^{B} 4\varepsilon_{ij}^{ab}\left[\left(\frac{\sigma_{ij}^{ab}}{r_{ij}^{ab}}\right)^{12} - \left(\frac{\sigma_{ij}^{ab}}{r_{ij}^{ab}}\right)^{6}\right] + \sum_{c=1}^{C}\sum_{d=1}^{D}\frac{q_i^c q_j^d}{4\pi\varepsilon_0 r_{ij}^{cd}} \qquad (2.6)$$

where φ_{ij} is the interaction between fluid molecules i and j, A and B are the number of LJ site on the molecule i and j, respectively, C and D are the number of charge on the molecule i and j, respectively, and $_0$ is the permittivity of a vacuum. The combined well-depth and collision diameters are given by the Lorentz-Berthelot mixing rule as seen below:

$$\varepsilon_{ij}^{ab} = \sqrt{\varepsilon_i^a \varepsilon_j^b} \qquad\qquad \sigma_{ij}^{ab} = \left(\sigma_i^a + \sigma_j^b\right)/2 \qquad (2.7)$$

The list of the molecular parameters for the LJ and charge sites used in this work is given in Table 2.1.

Table 2.1 The molecular parameters of gas molecules used in this work.

Adsorbate	Critical point		Interacting site	σ_{FF} (nm)	$_{FF}/k_B$ (K)	q (e)
	Pressure (atm)	Temperature (K)				
Helium	2.26	5.19	He	0.2556	10.22	0
Neon	2.77	44.49	Ne	0.2780	34.90	0
Argon	4.86	150.69	Ar	0.3405	119.8	0
Krypton	5.53	209.48	Kr	0.3685	164.40	0
Xenon	5.84	289.73	Xe	0.4047	231.00	0
Nitrogen	33.54	126.20	N	0.3310	36.00	-0.482
			M (Center site)	0	0	0.964
Carbon dioxide	72.90	304.20	C	0.280	27.00	0.70
			O	0.3050	79.00	-0.35

2.5   Solid-Fluid Interaction

Two models are commonly used to model the solids. The first is the atomistic model, which takes into account the periodic arrays of discrete carbon atoms in hexagonal arrangement. The potential between adsorbate and carbon atoms of solid is calculated by using 12-6 Lennard-Jones equation and/or Coulombic electrostatic interaction. The second model is referred to the structureless model, in which the solid is composed of structureless layers with constant surface density of carbon atoms. The various types of structureless model studied in this work are as follows.

2.5.1   Infinite surface and slit pore models

The solid-fluid interaction energy between a LJ site i of that molecule and the infinite homogeneous flat surface being modeled, with periodic boundary condition, is calculated by the following 10-4-3 Steele potential (Steele, 1973):

$$\varphi_{i,S}(z_i) = 2\pi\rho_S\varepsilon_{SF}\sigma_{SF}^2\left[\frac{2}{5}\left(\frac{\sigma_{FF}}{z_i}\right)^{10} - \left(\frac{\sigma_{FF}}{z_i}\right)^4 - \left(\frac{\sigma_{FF}^4}{3\Delta(0.61\Delta+z_i)^3}\right)\right] \quad (2.8)$$

where z_i the distance of LJ site i and from the flat surface, $_{SF}$ and σ_{SF} the solid-fluid well-depth and collision diameter calculated from Lorentz-Berthelot mixing rule with $_{SS}/k_B$ = 28 K and σ_{SS} = 0.34 nm for graphitic surface. For a slit pore, the adsorbate molecule interacts between two graphitic walls.

2.5.3   Finite surface and slit pore models

A finite size surface of constant surface density can be described by a Bojan-Steele potential, which is infinite extent in x-direction and finite extent in y-

direction. The solid-fluid interaction energy of this surface is given by (Bojan and Steele, 1988; Bojan and Steele, 1989):

$$\varphi_{i,S}(z_i) = 2\pi\rho_S\varepsilon_{SF}\sigma_{SF}^2$$
$$\left\{\left[\varphi_{rep}(z_i,y_i^+) - \varphi_{rep}(z_i,y_i^-)\right] - \left[\varphi_{att}(z_i,y_i^+) - \varphi_{att}(z_i,y_i^-)\right]\right\} \tag{2.9}$$

where the variables of y^+ and y^- are the y-coordinates of the right and left hand edge relative to the position of a LJ site as shown as the equation below:

$$y_i^+ = \frac{L}{2} - y_i \qquad\qquad y_i^- = -\frac{L}{2} - y_i \tag{2.10}$$

2.5.3 Infinite cylindrical pore model

The interaction energy of a cylindrical pore wall of infinite extent in axial direction and a LJ site i of that molecule can be calculated using the following equation (Tjatjopoulos et al., 1988):

$$\varphi_{i,S}(r_i) = 4\pi^2\rho_S\varepsilon_{SF}\sigma_{SF}^2\left(I_6 - I_3\right) \tag{2.11}$$

The functions of I_3 and I_6 are given by:

$$I_3 = \frac{3}{4}\left(\frac{\sigma_{SF}}{R}\right)^4\left[1 - \left(\frac{r_i}{R}\right)^2\right]^{-4}F\left[-\frac{3}{2};-\frac{3}{2};1;\left(\frac{r_i}{R}\right)^2\right] \tag{2.12}$$

$$I_6 = \frac{63}{128}\left(\frac{\sigma_{SF}}{R}\right)^{10}\left[1 - \left(\frac{r_i}{R}\right)^2\right]^{-10}F\left[-\frac{9}{2};-\frac{9}{2};1;\left(\frac{r_i}{R}\right)^2\right] \tag{2.13}$$

where R is radius of the infinite cylinder and r is the radial distance between a LJ site and the center of the cylinder.

2.5.4 Spherical pore model

The interaction energy of a spherical pore wall and a LJ site i of that molecule can be calculated using the following equation (Baksh and Yang, 1988):

$$\varphi_{i,S}\left(r_i\right) = 2\pi\rho_S \varepsilon_{SF} \sigma_{SF}^2 \left[I_{10} - I_4\right] \tag{2.14}$$

The functions of I_4 and I_{10} are given by:

$$I_4 = \sum_{j=0}^{9} \left(\frac{\sigma_{SF}^4}{R^j x^{4-j}} + \left(-1\right)^j \frac{\sigma_{SF}^4}{R^j \left(x-2R\right)^{4-j}} \right) \tag{2.15}$$

$$I_{10} = \frac{2}{5}\sum_{j=0}^{9} \left(\frac{\sigma_{SF}^{10}}{R^j x^{10-j}} + \left(-1\right)^j \frac{\sigma_{SF}^{10}}{R^j \left(x-2R\right)^{10-j}} \right) \tag{2.16}$$

where $x = R - r_i$ is the distance between a spherical pore wall and a LJ site i radially.

2.6 Analysis of Simulation Data

2.6.1 Surface excess density

The surface excess of adsorption is defined as the excess with respect to a gas reference amount:

$$\Gamma_{ex} = \frac{N_{ex}}{S} = \frac{\langle N \rangle - \rho_b V_{acc}}{S} \tag{2.17}$$

where <N> is the ensemble average of number of particles in the simulation box, ρ_b is the bulk gas density, V_{acc} is the accessible volume and S is geometrical surface area of the solid. The calculation of accessible volume will be discussed in Chapter 3. This quantity is interesting when the gas is adsorbed under supercritical conditions because the excess isotherm exhibits a maximum. We shall show in Chapter 7 how important this is for the adsorption on a graphitic surface at very high temperature and pressure.

2.6.2   Absolute pore density

The absolute pore density, ρ_{pore}, is defined as the number of molecules per unit accessible volume using the following equation:

$$\rho_{pore} = \frac{\langle N_{pore} \rangle}{V_{acc}} \tag{2.18}$$

where <N_{pore}> is the ensemble average of number of particles within the pore space. This quantity will indicate how dense the adsorbate is within the pore.

2.6.3   Isosteric heat

The isosteric heat, or heat of adsorption, is defined as the ratio of the infinitesimal change in the adsorbate enthalpy to the infinitesimal change in the excess adsorbed amount. The isosteric heat can be experimentally measured by calorimetric means, or it can be calculated by applying the Clausius-Clapeyron equation to the experimental isotherms at two closely temperatures.

For the GCE simulation, the isosteric heat can be obtained by applying the thermodynamic fluctuations (Nicholson and Parsonage, 1982):

$$q_{st} = k_B T - \frac{f(U,N)}{f(N,N)} \tag{2.19}$$

where U is the configurational energy of the simulation box. The function f is defined as $f(X,Y) = <XY> - <X><Y>$, where the symbol $< >$ denotes as the ensemble average. The assumption of this isosteric heat equation is the ideal gas and smaller molar volume of the adsorbed phase compared to the bulk gas phase.

For the MCE simulation, the differential isosteric heat in the adsorption cell is defined as the energy of the adsorbed phase per unit change in the excess amount, as shown in the following equation (Rouquerol et al., 1999):

$$q_{st} = k_B T + u_b - \frac{\partial(\langle U \rangle - U_G)}{\partial N_{ex}} \tag{2.20}$$

where U_G is the energy of the gas space in the adsorption cell and u_b is the molecular internal energy of the gas reservoir.

2.6.4 Pressure

The method used to calculate the pressure of the bulk gas system is through the virial equation in the following equation (Allen and Tildesley, 1989). For MCE simulation, the calculation takes place in the gas reservoir box under subcritical condition.

$$P = \rho_b k_B T - \frac{1}{3V_b} \sum_{i=1}^{N_b-1} \sum_{j=i+1}^{N_b} \frac{\left(\vec{r_{ij}} \cdot \vec{r_{ij}^{ab}} \right)}{r_{ij}^{ab}} \frac{\partial \varphi_{ij}^{ab}}{\partial r_{ij}^{ab}} \tag{2.21}$$

where the subscript b indicates a bulk gas system. The second term is the intermolecular pair virial function.

2.6.5 Local density distribution

For 2D-local density distribution, the simulation space was divided into 2D-differential bins in the y- and z-directions and the 2D-density of each bin is defined as:

$$\rho(y,z) = \frac{\langle N(y,z) \rangle}{L_x \Delta y \Delta z} \tag{2.22}$$

where <N(y,z)> is the ensemble average of the number of particles in the bin bounded by [y, y+Δy] and [z, z+Δz].

2.6.6 Local particle number fluctuation

The local particle number fluctuation (PNF) is useful in probing the non-uniformity of an adsorbate separated into three phases in the pore: the adsorbed phase, the interfacial undulating and the gas-like regions (Fan et al., 2014). Along one direction, such as radial direction, this is defined as (Razak et al., 2011)

$$PNF(r) = \frac{f(N(r), N(r))}{\langle N(r) \rangle} \tag{2.23}$$

In locations where the adsorbate is very dense, close to the pore wall, the PNF is less than unity, but in the region where mass exchange is taking place between the adsorbed layer and the gas-like core, the PNF is greater than unity. In the ideal-gas limit, the PNF approaches unity.

2.6.7 Local compressibility

To measure the cohesiveness of the adsorbed phase and gas region, the local compressibility is calculated in one direction, such as z-direction. For each bin, it is defined as

$$\kappa(z) = -\frac{1}{V(z)}\frac{\partial V}{\partial P} = \frac{PNF(z)}{k_B T\rho(z)} \tag{2.24}$$

2.7 The Mid-Density Scheme

The mid-density scheme (MDS), was developed by Liu et al. (2011) to determine the equilibrium transition in the hysteresis loop of a capillary condensation in mesoporous solids, and has been successfully used in other applications. Here it was applied to locate the transition in the adsorbed argon at temperatures less than the 2D-critical temperature as outlined in Chapter 4. The description is depicted in Figure 2.11. At a given chemical potential μ^* in the hysteresis loop, the two states on the hysteresis boundary are N_A and N_B. Molecules are removed randomly from the high density configuration to give a state having $(N_A+N_B)/2$ molecules (the Mid-Density). Simulation is then carried out at this mid-density state in the canonical ensemble until the system is fully relaxed, followed by a simulation in the grand canonical ensemble at the same chemical potential μ^*. The state achieved at the end is taken to be equilibrium state.
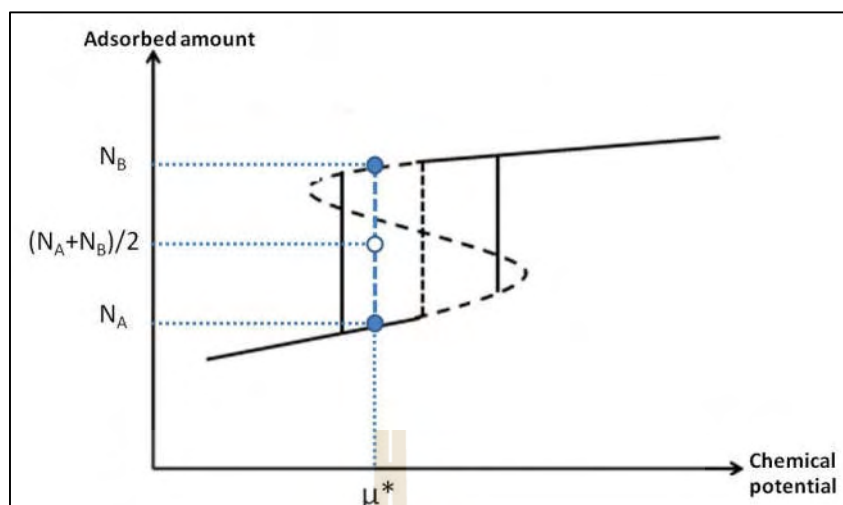
Figure 2.11 Schematic diagram of the mid-density scheme for determining equilibrium phase transition.

2.8 References

Allen, M. P. and Tildesley, D. J. (1989) **Computer simulation of liquids**. Oxford University Press: Oxford.

Baksh, M. S. A. and Yang, R. T. (1991) Model for spherical cavity radii and potential functions of sorbates in zeolites. **AIChE Journal**. 37: 923-930.

Bandosz, T. J., Biggs, M. J., Gubbins, K. E., Hattori, Y., Iiyama, T., Kaneko, K., Pikunic, J. and Thomson, K. (2003). Molecular models of porous carbons, **Chemistry and Physics of Carbon**, 28: 41-228.

Banhart, F., Kotakoski, J. and Krasheninnikov, A. V. (2011). Structural defects in graphene. **ACS Nano**. 5: 26-41.

Biggs, M. and Agarwal, P. (1994). Mass diffusion of diatomic fluids in random micropore spaces using equilibrium molecular-dynamics. **Physical Review E**. 49: 531-537.

Bojan, M. J. and Steele, W. A. (1988). Computer simulation of physisorption on a heterogeneous surface, **Surface Sciences**, 199: 395-402.

Bojan, M. J. and Steele, W. A. (1989). Computer simulation of physisorbed Kr on a heterogeneous surface, **Langmuir**, 5: 625-633.

Chang, C. F., Chang, C. Y. and Tsai, W. T. (2000). Effects of burn-off and activation temperature on preparation of activated carbon from corn cob agrowaste by CO_2 and steam. **Journal of Colloid and Interface Science**. 232: 45-49.

Choi, S., Drese, J. H. and Jones, C. W. (2009). Adsorbent materials for carbon dioxide capture from large anthropogenic point sources. **ChemSusChem**. 2: 796-854.

De Boer, J. H., (1972), The structure and texture of a physical adsorbent. **Colloques Internationaus du CNRS**. 201: 407.

Everett, D. H. (1967), **Adsorption hysteresis**. Marcel Dekkar: New York. 1055-1110.

Fan, C., Zeng, Y., Do, D. D. and Nicholson, D. (2014). An undulation theory for condensation in open end slit pores: critical hysteresis temperature and critical hysteresis pore size. **Physical Chemistry and Chemical Physics**. 16: 12362-12372.

Franklin, R. E. (1951). Crystallite growth in graphitizing and nongraphitizing carbons, **Proceedings of the Royal Society of London**, 209: 196-218.

Frenkel, D. and Smit, B. (2002). **Understanding molecular simulation: from algorithms to applications**. Academic Press: San Diego.

Liu, Z., Herrera, L., Nguyen, V. T., Do, D. D. and Nicholson, D. (2011). A Monte Carlo scheme based on mid-density in a hysteresis loop to determine equilibrium phase transition. **Molecular Simulation**. 37: 932-939.

Mahadik-Khanolkar, S., Donthula, S., Sotiriou-Leventis, C. and Leventis, N. (2014) Polybenzoxazine aerogels: 1. High-yield room-temperature acid-catalyzed systhesis of robust monoliths, oxidative aromatization, and conversion to microporous carbons. **Chemistry of Materials**. 26: 1303-1317.

Marsh, H. and Reisono, F. R. (2006). **Activated carbon**. Elsevier.

Neimark, A. V. and Vishyakov, A. (2000). Gauge cell method for simulation studies of phase transitions in confined systems. **Physical Review E**. 62: 4611.

Nguyen, T. X., Cohaut, N., Bae, J. and Bhatia, S. K. (2008). New method of atomistic modeling of the microstructure of activated carbons using hybrid reverse Monte Carlo simulation. **Langmuir**. 24: 7912-7922.

Nicholson, D. and Parsonage, N. G. (1982). **Computer simulation and the statistical mechanics of adsorption**. Academic Press: London.

Palmer, J. C. and Gubbins, K. E. (2012). Atomistic models for disordered nanoporous carbons using reactive force fields. **Microporous and Mesoporous Materials**, 154: 24-37.

Pré, P., Huchet, G., Jeulin, D., Rouzaud, J. N., Sennour, M. and Thorel, A. (2013). A new approach to characterize the nanostructure of activated carbons from mathematical morphology applied to high resolution transmission electron microscopy images. **Carbon**. 52: 239-258.

Radovic, L. R. (2003). **Chemistry and physics of carbon**. Volume 28. Marcel Dekkar Inc.

Razak, M. a. A., Nguyen, V. T., Herrera, L. F., Do, D. D. and Nicholson, D. (2011). Microscopic analysis of adsorption in slit-like pores: layer fluctuations of

particle number, layer isosteric heat and histogram of particle number. **Molecular Simulation**. 37: 1031-1043.

Reinoso, F. R., Pastor, A. C., March, H. and Martinez, M. A. (2000). Preparation of activated carbon cloths from viscous rayon. Part II: physical activation processes. **Carbon**. 38: 379-395.

Rouquerol, F., Rouquerol, J. and Sing, K. (1999). **Adsorption by Powders and Porous Solids**, Academic Press: London.

Sing, K. S. W., Everett, D. H., Haul, R. A. W., Moscou, L., Pierotti, R. A., Rouquerol, J. and Siemieniewska, T. (1985). Reporting physisorption data for gas/solid systems with special reference to the determination of surface area and porosity. **Pure and Applied Chemistry**. 57, 603-619.

Steele, W. A. (1973). The physical interaction of gases with crystalline solids: I. gas-solid energies and properties of isolated adsorbed atoms. **Surface Sciences**. 36: 317-352.

Teng, H. and Lin, H. C. (1998). Activated carbon production from low ash subbituminious coal with CO_2 activation, **AIChE Journal**. 44: 1170-1177.

Thommes, M., Kaneko, K., Neimark, A. V., James, P. O., Reinoso, F. R., Rouquerol, J. and Sing, K. (2015). Physisorption of gases with special reference to the evaluation of surface area and pore size distribution (IUPAC technical report). **Pure and Applied Chemistry**.

Thomson, K. T. and Gubbins, K. E. (2000). Modeling structure morphology of microporous carbons by reverse Monte Carlo. **Langmuir**. 16: 5761-5773.

Tjatjopoulos, G. J., Feke, D. L. and Mann, J. A. (1988). A molecule-micropore interaction potentials. The Journal of Physical Chemistry, 92: 4006-4007.

Wang, C., Watson, J. K., Louw, E. and Mathews, J. P. (2015). Construction strategy for atomistic models of coal chars capturing stacking diversity and pore size distribution. **Energy and Fuels**. 29: 4814-4826.

Yuan, Z. Y., Zhang, Y. M. and Zhou, Y. F. (2013). Effect of curing catalyst content on the pore structure of porous carbon obtained from phenolic resin and furfuryl alcohol. **Material Letter**. 110: 218-220.

Yue, Z., Economy, J. and Bordson, G. (2006) Preparation and characterization of NaOH activated carbon from phenolic resin. **Journal of Material Chemistry**. 16: 1456-1461.
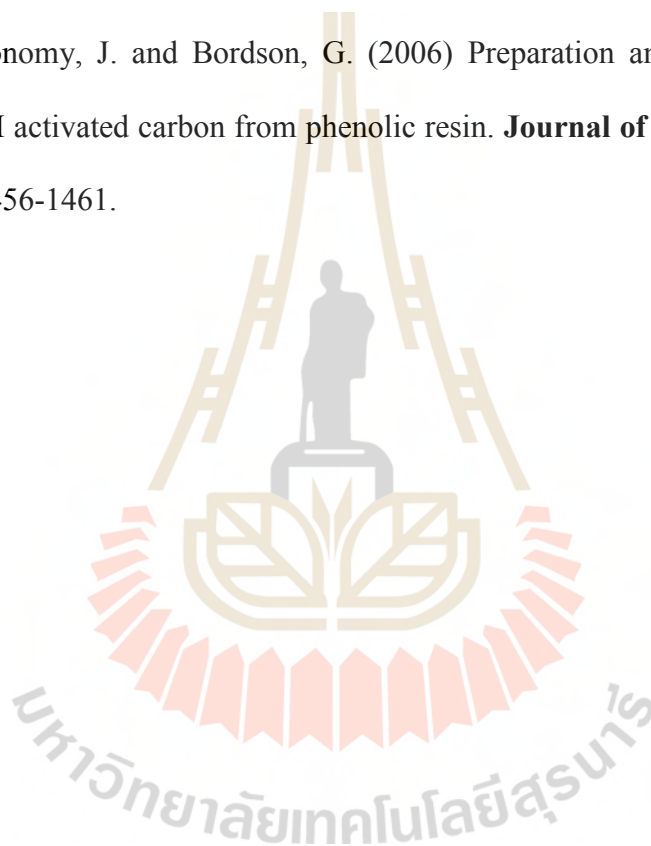
CHAPTER III

PORE CHARACTERIZATION AND ADSORPTION

ISOTHERMS OF SIMULATED POROUS CARBONS

3.1 Abstract

We refined and improved the computation efficiency of the TriPOD technique to determine the accessible characteristics of porous solids with known configuration of solid atoms. Instead of placing a probe molecule randomly, we implemented a scheme of dividing the porous solid into 3D-grids and computing the solid-fluid potential energies of all these grid points. We illustrated the potential of this technique to determine the total pore volume, the surface area and the pore size distribution of various molecular models of porous carbons ranging from simple pore models to a more complex simulated porous carbon model, the latter of which is constructed from a canonical Monte Carlo simulation of carbon microcrystallites of various sizes. Finally, the conventional Grand Canonical Monte Carlo (GCMC) simulation is used to generate adsorption isotherms of argon (87 K), nitrogen (77 K) and carbon dioxide (273 K), and compare them with the experimental data of a biomass derived activated carbon.

3.2   Introduction

The characterization of structural properties of nanoporous carbon is best done with the gas adsorption technique, using gases such as N_2 at 77 K and CO_2 at 273 K (Rouquerol et al., 1999; Thommes et al., 2015). These molecular probes have quadrupole moment and their adsorption is preferable in sites carrying partial charges, potentially resulting in erroneous derivation of structural properties, especially surface area (Kruk et al., 2000a). To avoid this, inert gases with no partial charges, such as argon, are increasingly used (Kruk and Jaroniec, 2000b) because of its non specific adsorption. Once the adsorption isotherm is obtained experimentally, the pore volume is derived from the adsorptive capacity at a relative pressure of 0.95 (Neimark et al., 1998) and the surface area from the application of the BET method (Brunauer et al., 1938) to experimental data in the low relative pressure range of 0.05 to 0.3 (Rouquerol et al., 1999). For the determination of pore size distribution, there are two main approaches: the classical methods (Madani, et al., 2015a) and the adsorption integral approach (Madani et al., 2015b). The classical methods rely on the macroscopic thermodynamics which are separately applied for micropores and mesopores, while the integral approach is based on an ensemble of model pores whose sizes cover micropores and mesopores. The Grand Canonical Monte Carlo simulation (GCMC) or density functional theory (DFT) (Do and Do, 2003) based on statistical mechanics are then employed to generate the simulated isotherms for these model pores. The sum of these isotherms with weighting factors of specific pore volumes is then matched with the "experimental" isotherm to determine these specific pore volumes which form the pore size distribution, from which the total pore volume can be derived.

However, in cases where the atomistic configuration of porous carbon is available, the determination of the textural properties is better done with a computer simulation approach, which is superior to the classical methods discussed in the above paragraph, in the sense that we can exactly define a void space that is accessible to a given molecular probe. To date, there are three definitions of void space. It is

1. the space that solid atoms and a probe molecule treated as hard sphere such that they do not overlap each other (Connolly, et al., 1983). The accessible surface is located at the surface of the probe molecule.

2. proposed by Düren et al. (2007). It is the same as the first one except that the accessible surface is now located at the center of the probe molecule.

3. suggested by Do et al. (2007). It is defined as the space accessible to the center of probe molecule having non-positive solid-fluid potential. We shall use this definition in this paper to illustrate the refined scheme of the TriPOD method.

In this work, we develop a refined scheme of TriPOD to drastically improve its computation efficiency to calculate the accessible pore volume, surface area and pore size distribution, by employing the Monte Carlo integration (MCI) based on the definition of accessible region. The key concept is to divide a porous solid (simulation space) into 3D-grid points and compute their solid-fluid potential energies. Once each grid has been tested its accessibility with respect to volume, area and pore size, the textural properties of the given solid can be derived. We will demonstrate our method with simple pore models and a simulated porous carbon, and derive structural characteristics with different probe molecules. Finally we carry out a GCMC

simulation of argon, nitrogen and carbon dioxide adsorption in the simulated porous carbon, and compare the simulated results against the experimental data of an activated carbon derived from longan seed.

3.3   Porous Carbon Models

Four simple pore models, slit, cylinder, connected slits of different widths and wedge pores, are considered (Figure 3.1). The pore walls of these models are constructed with carbon atoms arranged in the same manner as those in a graphene layer.

(a)   (b)   (c)   (d)
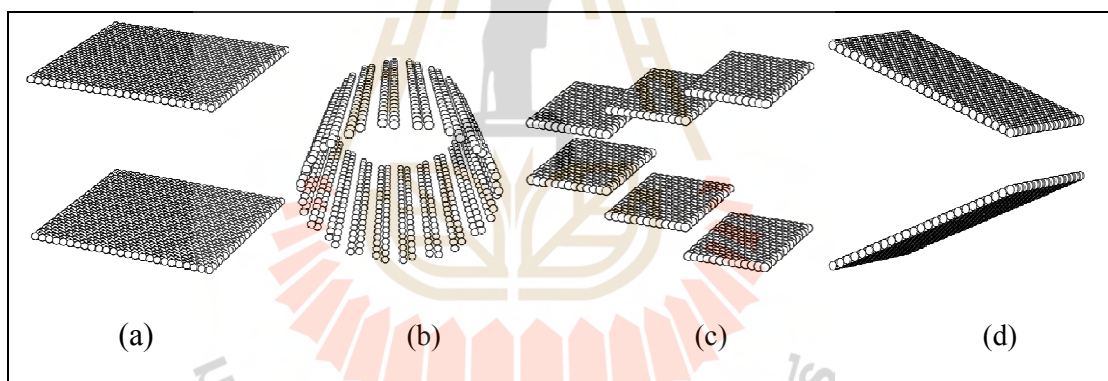
Figure 3.1   The simple pore models: (a) slit pore, (b) cylindrical pore, (c) connected slit pores and (d) wedge pore.

Another porous carbon, whose structure is more complex than the four simple ones described above, is also considered. This is constructed with a mimetic method based on Monte Carlo simulation (Herrera et al, 2009), to simulate a real porous carbon, not only showing a distribution of pore size but also a strong connectivity between different regions in the porous network. The simulated model is composed of

200 graphitic microcrystallites of five layers whose linear dimension is 2 nm length as reported experimentally by Franklin (1951). This collection of microcrystallites is performed in a canonical Monte Carlo simulation to obtain a metastable configuration of a porous carbon (Figure 3.2a), which is then cropped to produce a spherical porous carbon of radius of 7.5 nm (Figure 3.2b) to eliminate the large pore size region near the boundaries.
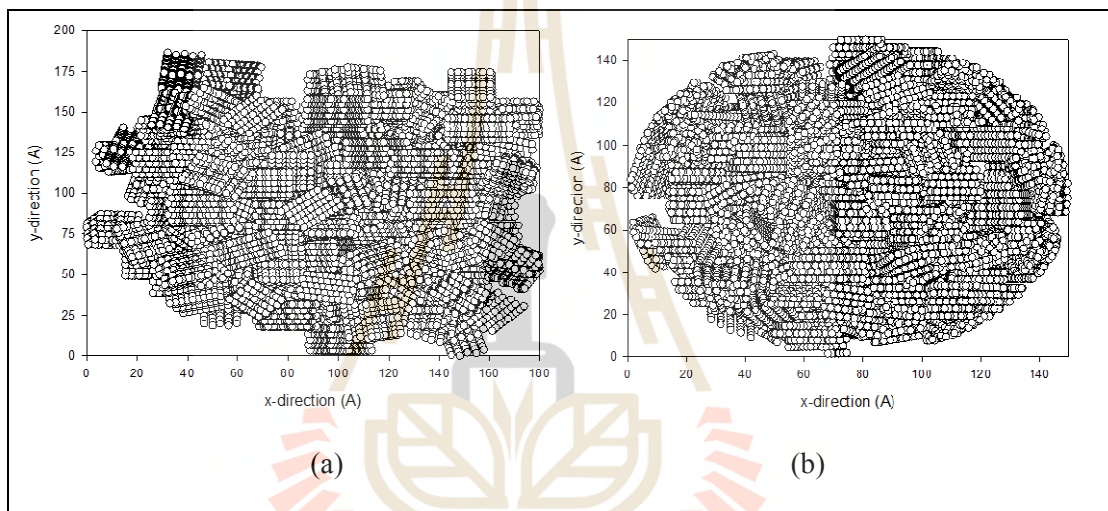
Figure 3.2   Molecular model of simulated porous carbon: (a) before and (b) after cropping as a spherical structure.

3.4   Pore Characterization

We applied the technique based on the concept of accessible space to obtain pore volume, surface and pore size distribution.

3.4.1   Accessible pore volume

Accessible pore volume (V_{acc}) is defined as the volume accessible to the center of mass of a probe particle at zero loading. Following a similar approach to

the one developed earlier (Do et al., 2008), instead of employing random insertion of a probe molecule, the simulation box is divided into a fine grid and we put the center of the probe molecule at every grid point and calculate its potential energy with all the solid atoms. For polyatomic molecules like CO_2 and N_2, we rotate the molecule many times and then store the lowest potential value for that grid in order to determine the accessible volume and surface area. The insertion of a given grid point is called a success if its potential is non-positive, otherwise it is a failure. An illustration of the insertion of the probe molecule can be seen in Figure 3.3. Finally, the accessible pore volume is simply computed by the volume of simulation box (V_{box}) times the fraction of successful insertion (f), that is, $V_{acc} = f \cdot V_{box}$.
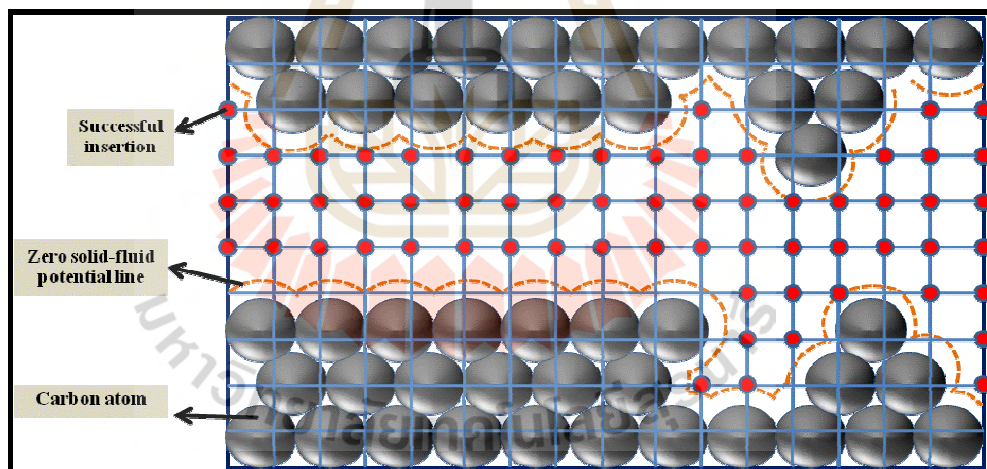
Figure 3.3   Schematic diagram of the determination of accessible pore volume of known porous carbon structure.

3.4.2 Accessible surface area

The accessible surface area (S_{acc}) is defined as the area the boundary on which the solid-fluid potential is zero (Herrera et al., 2010) (see the dashed line in

Figure 3.3). To compute this surface area, we continue on the calculation process from Section 3.4.1, where the lowest potential value has already known at every grid point. For each successful insertion, let us take grid "i" as shown in Figure 3.4 as an example. We determine the minimum distance ($r_{i,min}$) between the selected grid "i" and its closed point having zero solid-fluid potential as shown in the right panel of Figure 3.4. This zero potential point can be obtained by applying Bisection method between the grid "i" and its closest grid having non-negative potential "j". If the distance $r_{i,min}$ falls between r_{k-1} and r_k, we store that successful insertion in the volume of bin "k". Having done for every grid, the accessible volume of bin "k" ($V_{acc,k}$) is calculated by the volume of simulation box times the fraction of success falling in the bin (f_k), $V_{acc,k} = f_k \cdot V_{box}$.

Knowing the accessible volume of bin "k" for all bins, we compute the accessible surface area of the corresponding bin by the following equation:

$$S_{acc,k} = \frac{V_{acc,k}}{r_k - r_{k-1}} \qquad (3.1)$$

Once this process is done, we simply plot $S_{acc,k}$ as a function of distance from zero potential surface and then extrapolate to the y-axis to to obtain the accessible surface area. In addition, this also provides the information of surface curvature.
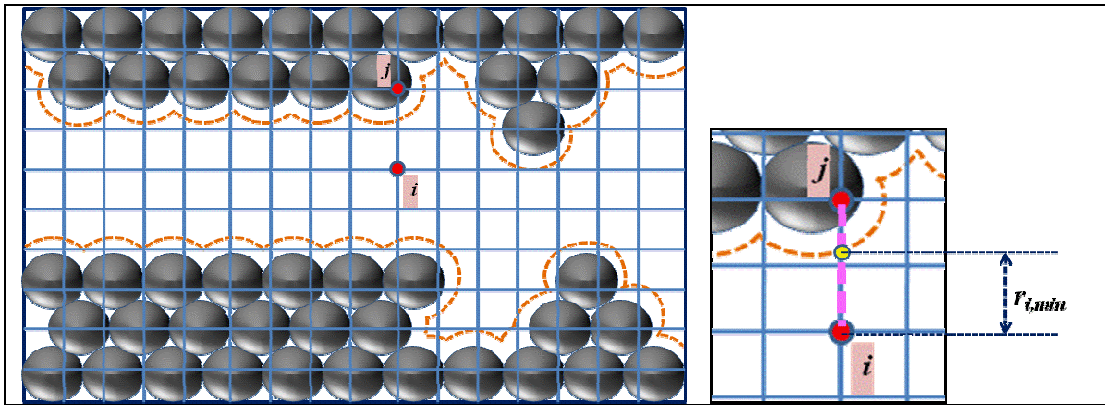
Figure 3.4   Schematic diagram of the calculation of minimum distance between the selected grid "i" and the closest point having zero solid-fluid potential.

3.4.3 Accessible pore size distribution

The pore size distribution (D_{acc}) is defined as the largest sphere which can be accommodated within the pore in such a way that any point within the sphere is non-positive solid-fluid potential (Do et al., 2008). Indicating of a pore size associated with each grid having successful insertion. To compute the pore size, we continue the further process from Section 3.4.2, where the minimum distance ($r_{i,min}$) is already known at every grid. For each successful insertion, let us take "i" as shown in Figure 3.5a as an example, we first construct the shells around the selected grid "i" and we use these points "j" in the shell having non-positive potential for providing the pore size of grid "i". Secondly, the distance between both grids is computed ($r_{i,j}$) and then checked whether this distance overlaps the inaccessible region. If it does not completely overlap (Figure 3.5b) the pore size (r_i) can be updated by choosing the largest distance to the zero solid-fluid potential surface as $r_i = \max(r_{i,min}, r_{j,min})$,

otherwise this point "*j*" cannot be designated as a pore size (Figure 3.5c). The process is repeated for all points in the first shell and then moved forward to the next shell. The process stops when every point in that considered shell is not met the criteria for updating pore size; this will provide the resultant pore diameter of grid "*i*" as $D_{acc,i} = 2r_i$. If the distance $D_{acc,i}$ falls between $D_{acc,k-1}$ and $D_{acc,k}$ we store that successful insertion in the volume of bin "*k*". When the computation is performed for every grid, the accessible volume of bin "*k*" ($V_{acc,k}$) is calculated by the volume of simulation box times the fraction of success falling in the bin (f_k), $V_{acc,k} = f_k \cdot V_{box}$. By plotting the $V_{acc,k}$ as a function of $D_{acc,k}$, we are able to obtain the accessible pore size distribution.
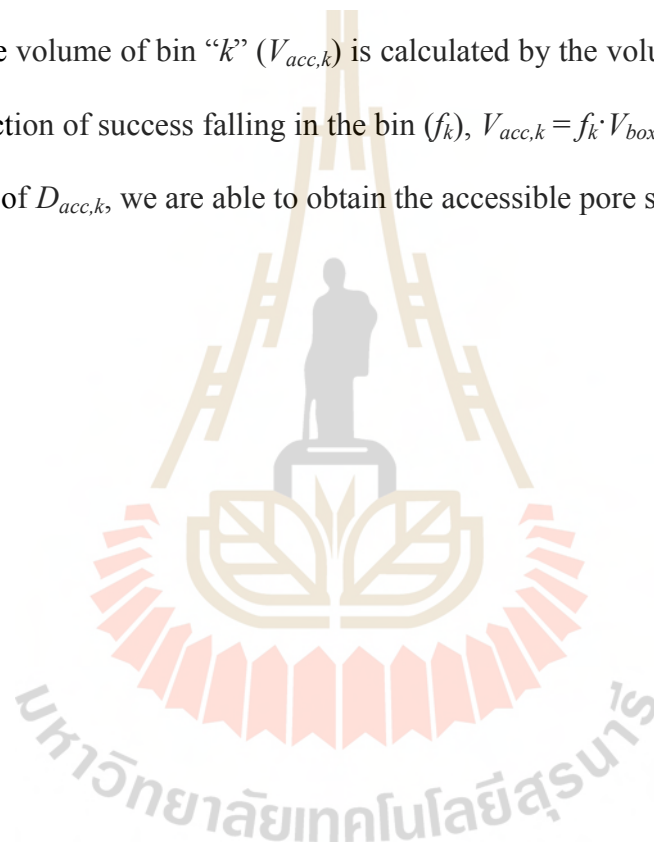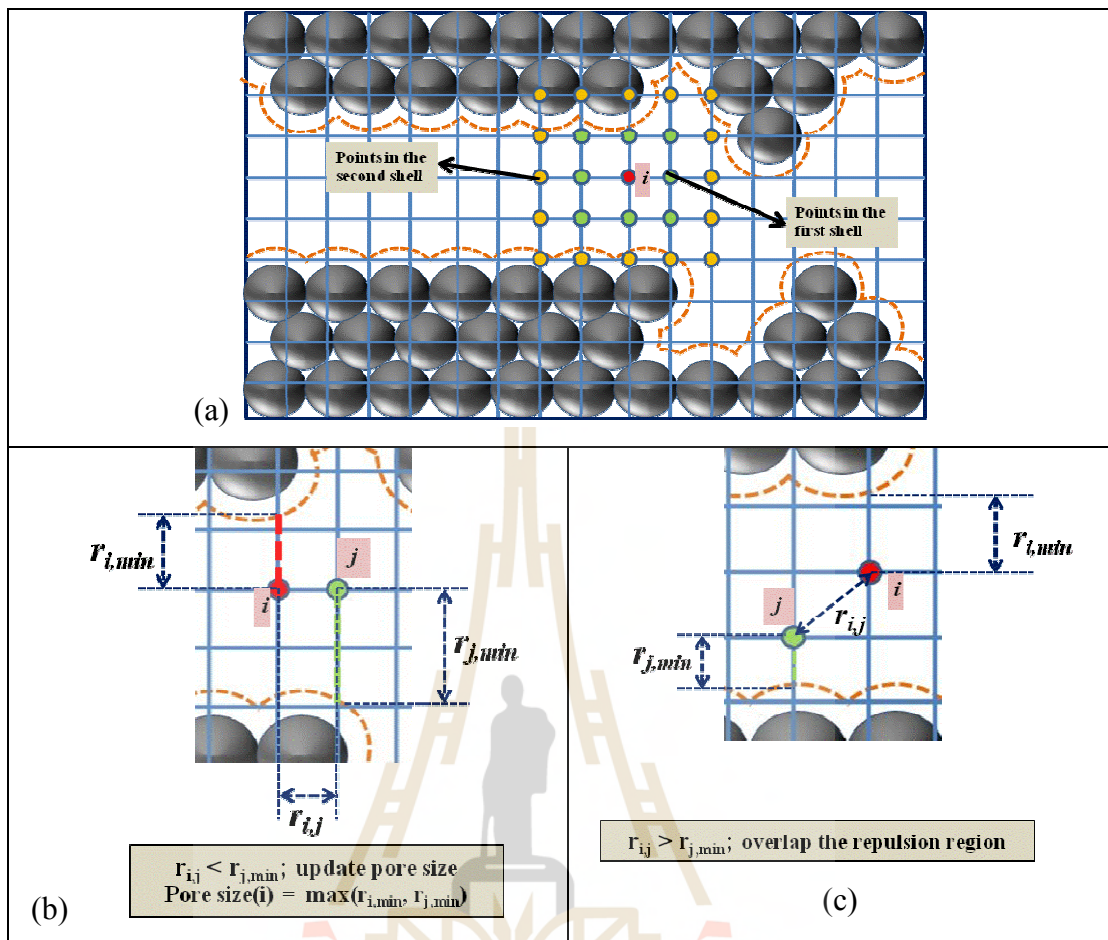
Figure 3.5   Schematic diagram of the determination of accessible pore size of the
selected grid *"i"*. Representation of (a) shells around grid *"i"*, (b) the
grid *"j"* on the first shell being allowable to search for the pore size,
and (c) another grid *"j"* on the corresponding shell rejected to find the
pore size due to overlapping to the repulsion region.

3.5   Results and Discussion

3.5.1   Graphitic slit pore

The graphitic slit pore in Figure 3.1a is composed of 1,372 carbon
atoms per a graphitic surface with a linear dimension of 5.75×5.54 nm and a

physical pore width of 1.562 nm, which is defined as the distance between the plane passing through the center of carbon atoms of one surface to that of the opposite surface. Results of the accessible pore volume, surface area and pore size distribution are shown in Figure 3.6.

Figure 3.6a shows that accessible pore volume decreases with the increasing size of the noble gases, as physically expected, since a smaller molecule can approach closer to the carbon atoms. The surface area profile of a slit pore for argon, as an illustration, is constant as seen in Figure 3.6b. The calculated accessible surface area being obtained by extrapolating to the y-axis at zero distance is also constant for all probe molecules as seen in Figure 3.6a. Remarkably, the surface area obtained by this method (1,232 m^2/g) is slightly larger than the geometrical surface area (1,164 m^2/g) because this method accounts for the curvature of the carbon atoms in the graphene surface. Figure 3.6c displays the accessible pore size distribution calculated from different probe molecules. The derived pore size distribution only exhibits a single peak which represents an accessible pore size of the pore. The 2D-contours of pore size for argon in Figure 3.6c also confirm the result of pore size distribution. We confirm the correctness of the accessible pore size obtained by the TriPOD method because it is, indeed, analytically related to the physical pore width by $D_{phy} = D_{acc} + 2z_0$ where z_0 is the position measured from the plane of center of graphene to the surface of zero solid-fluid potential. Since z_0 is greater with increasing molecular size, we can see that the accessible pore size is smaller with molecular size. This is consistent with the accessible volume that was discussed above.
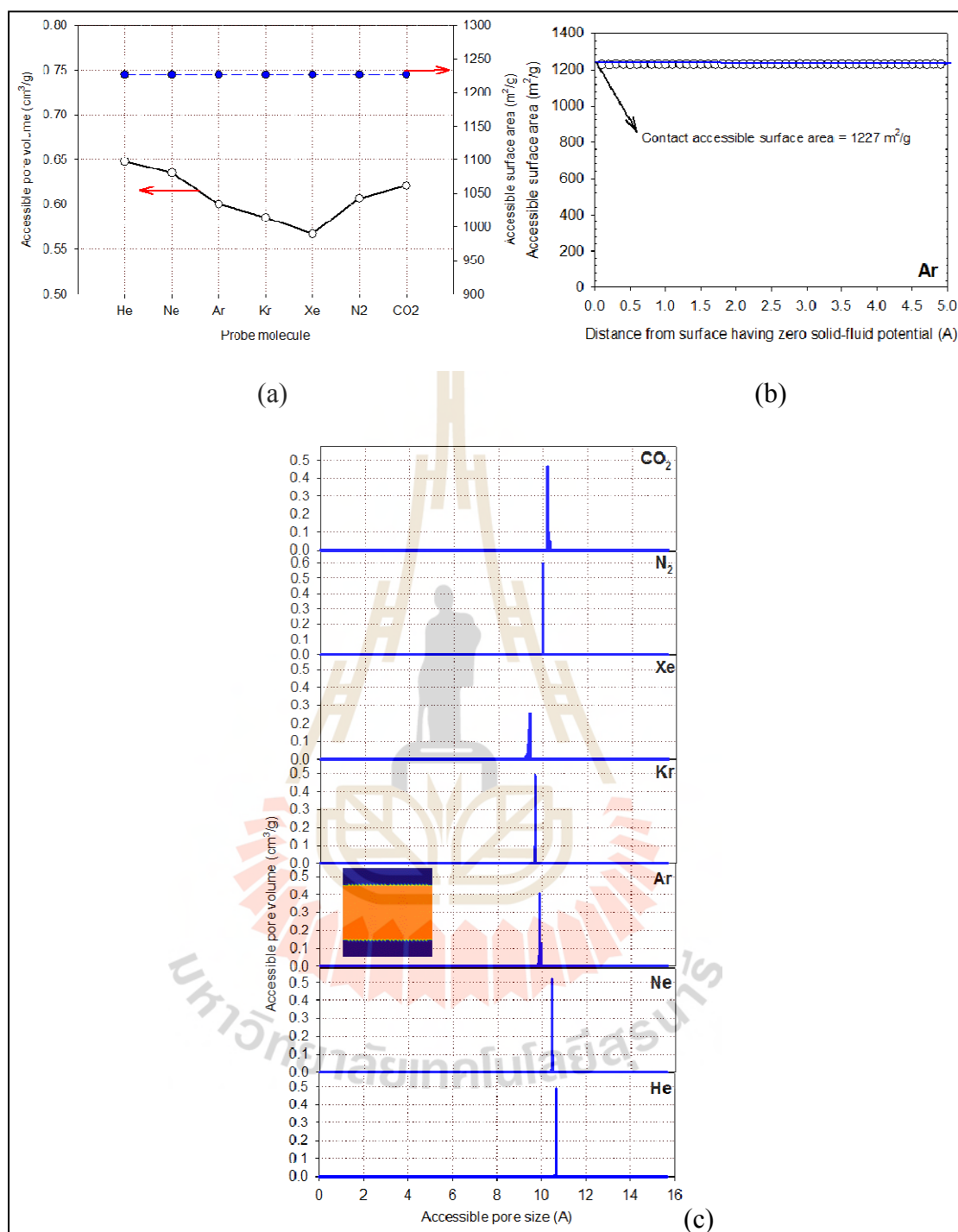
Figure 3.6 (a) Accessible pore volume and surface area of different probe molecules, (b) the illustration for determining accessible surface area of argon, and (c) accessible pore size distribution of different probe molecules of a graphitic slit pore.

3.5.2   Graphitic cylindrical pore

What we have concluded for the graphitic slit in Section 3.5.1 is reproduced here with a carbonaceous cylinder shown in Figure 3.1b. The radius and length of this cylinder are 1.36 nm and 4.93 nm, and there are 840 carbon atoms in the pore wall. The textural properties derived with the TriPOD method with various probe molecules are shown in Figure 3.7.

The differences between cylinder and slit are the variation of the accessible pore volume and surface area, and this is expected because of the surface curvature: the smaller is the molecular probe and the greater the accessible volume and area because of deeper approach to the carbon atom.

3.5.3   Connected graphitic slit pores

The effect of the connectivity can be studied by considering a pore composed of three uniform slits having physical pore widths of 0.7, 1.3 and 2.0 nm (shown graphically in Figure 3.1c). The structural characteristics of this pore with various probe molecules are shown in Figure 3.8 for accessible pore volume, surface area and pore size distribution, respectively. The linear dimensions for each graphitic wall are 2.84 × 2.81 nm.

The pore size distribution (Figure 3.8c) shows three distinct peaks, as would be expected. To show the effect of connectivity (the junction between two adjacent slits) the pore size profile along the pore axis is illustrated in Figure 3.8d. Obviously the accessible space and the pore size become smaller for larger molecular probe.
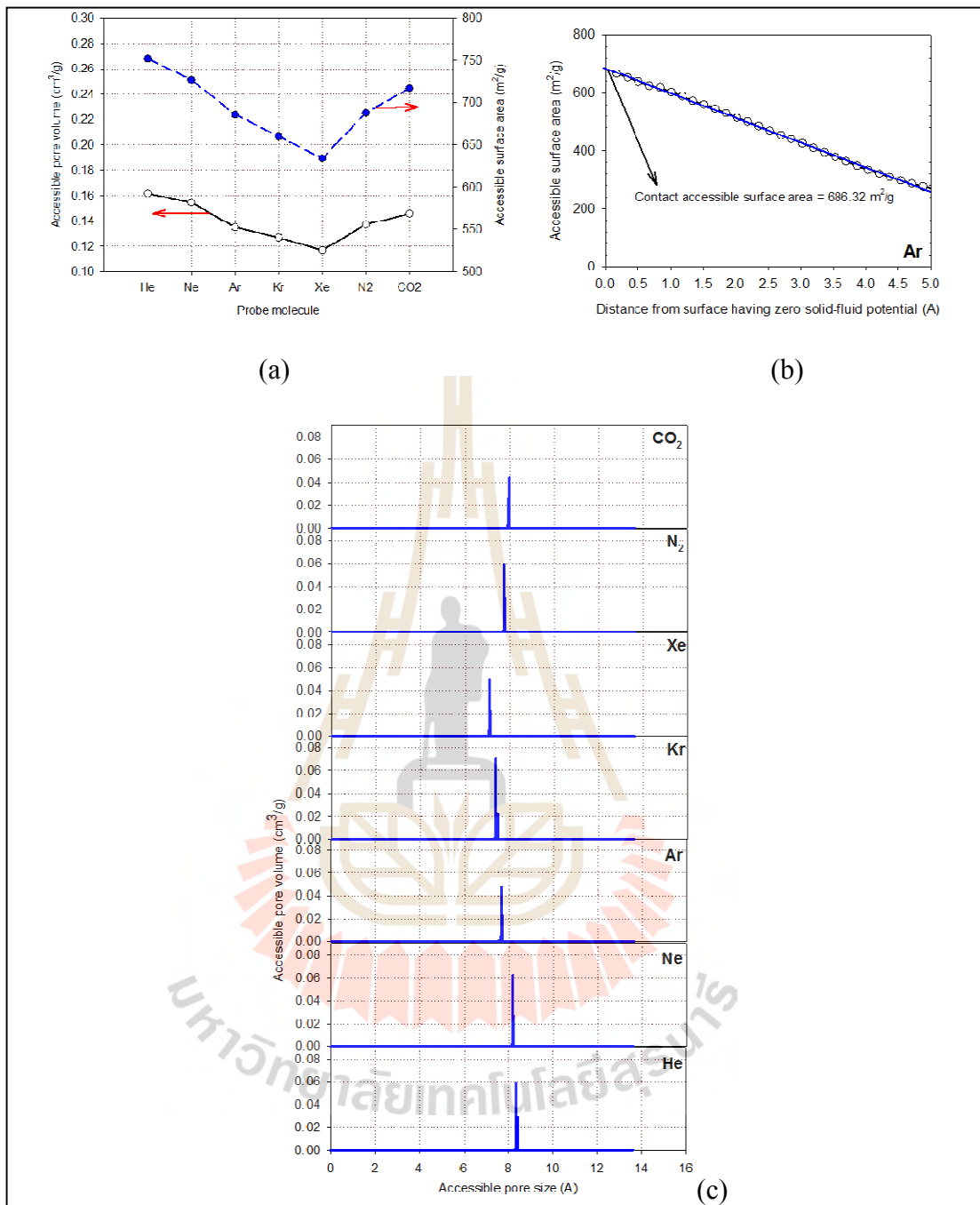
Figure 3.7 (a) Accessible pore volume and surface area of different probe molecules, (b) the illustration for determining accessible surface area of argon, and (c) accessible pore size distribution of different probe molecules of a graphitic cylindrical pore.
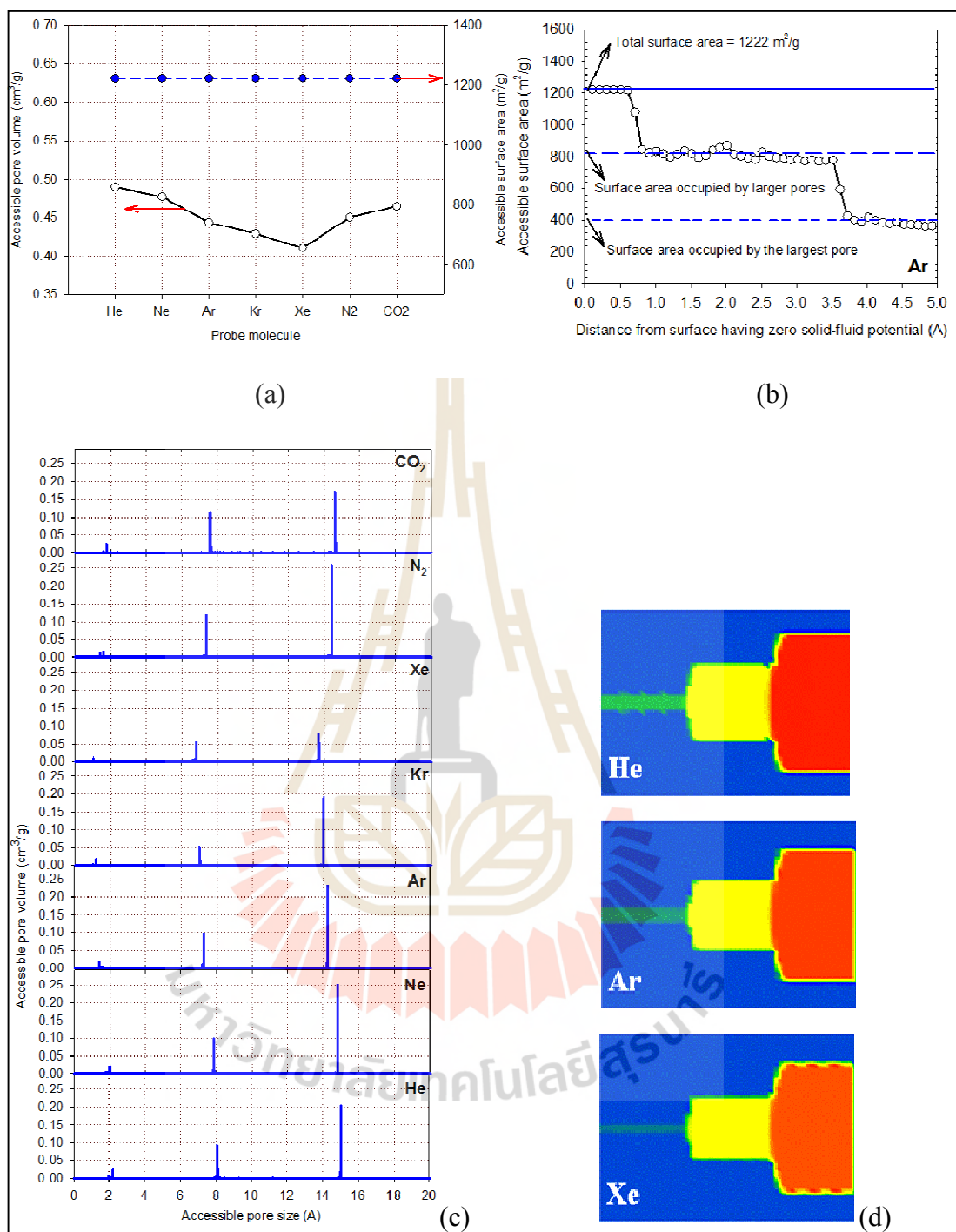
Figure 3.8 (a) Accessible pore volume and surface area of different probe molecules, (b) the illustration for determining accessible surface area of argon, and (c) accessible pore size distribution, (d) the pore size profiles of different probe molecules of connected graphitic slit pores.

The plot of surface area as a function of distance from zero potential surface for argon as a probe molecule is illustrated in Figure 3.8b for determining the accessible surface area. There are three regions of constant surface area: the first and highest surface area (1,222 m^2/g) is for calculation of whole pore, while the second and third ones are for the larger (813 m^2/g) and largest pores (408 m^2/g), respectively.

3.5.4 Graphitic wedge pore

Having discussed the well-defined slit and cylindrical pore shapes, we now turn to discuss the porous properties of a graphitic wedge pore (Figure 3.1d) with variation of pore sizes along the single pore. The linear dimensions for each pore wall are exactly the same as the wall of the slit pore but the physical pore widths of narrow and wide ends are set as 0.4 and 1.562 nm, respectively.

Figure 3.9 shows the structural properties for the wedge pore by using different probe molecules. The results of accessible pore volume and surface area (Figure 3.9a) are consistent with the cylindrical pore dealth with earlier, regarding to the effect of probe size. This suggests that the interior of wedge pore is concave-like surface as seen from the linear decrease of surface area with distance in Figure 3.9b. However, we raise a question why the derived accessible surface area of the wedge pore is not the same as that of the slit pore even though we use the same pore wall's dimension? To address this question, Figure 3.9d shows that the accessible space becomes smaller with larger probe size, hence resulting in the lesser accessible surface area.

Figure 3.9c shows broad distribution of pore size and it then peaks near the end of distribution where it represents the accessible pore size of the wider end of the pore, as substantiated by the pore size contour in Figure 3.9d. Interestingly, the

highest peak locates exactly at the same position as that of the slit pore (Figure 3.6c). However, this does not mean that the adsorption mechanism of the wedge pore is similar to that of the slit pore (Zeng et al., 2015). Therefore, using the uniform slit pore as kermels to analyze the pore size distribution by means of experimental data might underestimate, especially the mesopore due to the occurrence of capillary condensation.

3.5.5 Nitrogen and carbon dioxide gases as a probe

According to Figure 3.6-3.9, we also applied the nitrogen and carbon dioxide as a probe to demonstrate the application of polyatomic molecules for determining the porous properties. From our observation from these simple pore models, the values of porous properties from nitrogen are nearly the same as those from argon. However, for carbon dioxide, they are in the range between neon and argon; this indicates that CO_2 can be probe nearer to the surface of carbon atom than N_2. This should explain why CO_2 is typically used for characterizing porous materials containing ultramicropores, apart from solving the diffusional transport into the pores (Castello et al., 2004). As a result, in order to save the computational time due to molecular orientation, we here recommend that neon and argon can be applied to characterize porous carbons with the absence of surface functional groups, instead of using nitrogen or carbon dioxide.
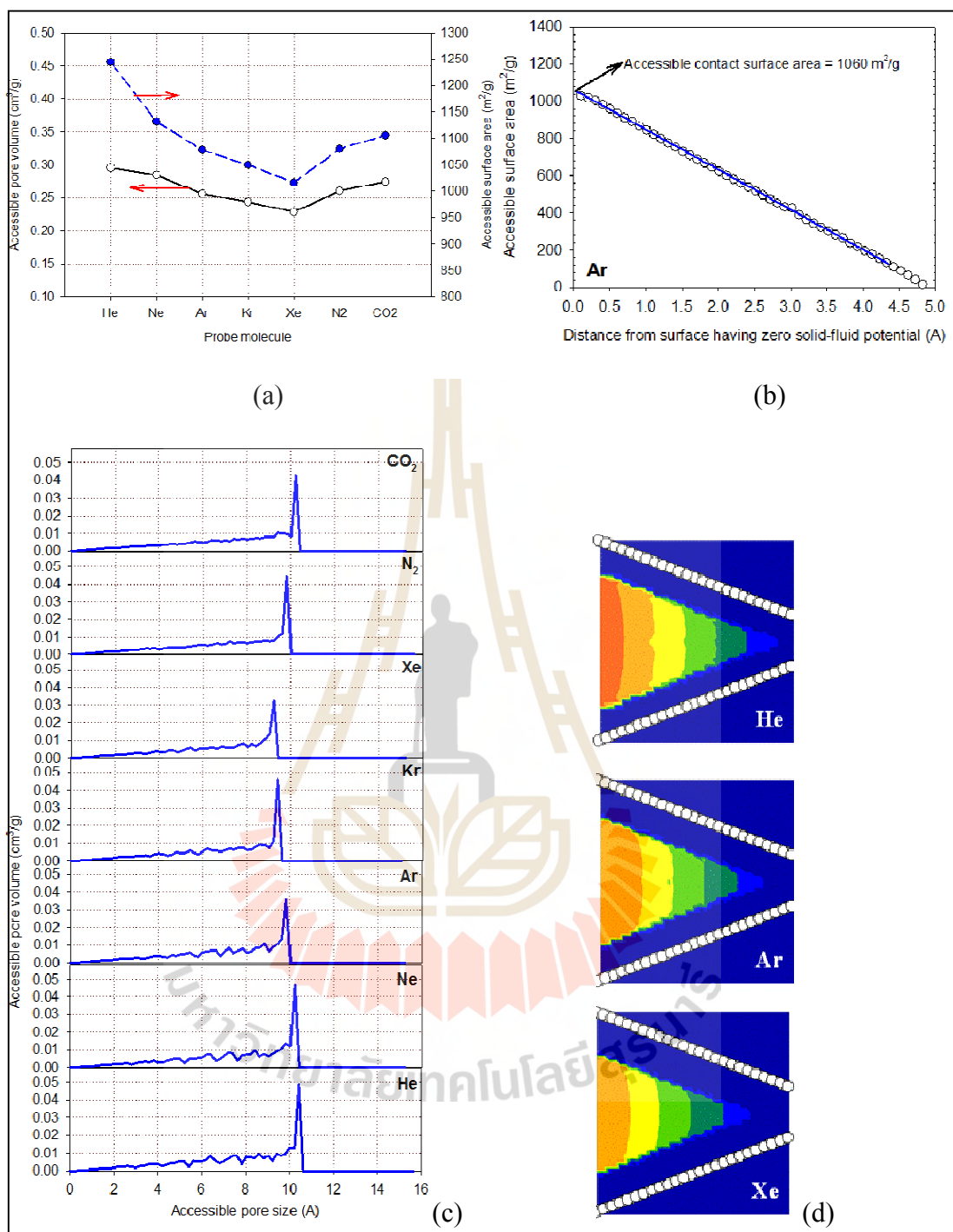
Figure 3.9 (a) Accessible pore volume and surface area of different probe molecules, (b) the illustration for determining accessible surface area of argon, and (c) accessible pore size distribution, (d) the pore size profiles of different probe molecules of a graphitic wedge pore.

3.5.6 Simulated porous carbon

Before discussing the results of textural properties of simulated porous carbon constructed in Section 3.3.1, we examined the pore topology within the carbon model. Figure 3.10a shows the 3D-snapshot of our simulated porous carbon. To further understand the perspective of pore shape, we selected the cross-section residing between two yellow planes and plotted into 2D-atomistic snapshot as presented in Figure 3.10b. In contrast to the simple pore models, we can see that the pores are irregular in shape and connected as 3D-network. We further investigate the accessible and inaccessible regions by probing the 2D-crossectional snapshot with argon giving the accessibility contour as shown in Figure 10c. The contour projects exactly the same as the snapshot and the accessible pore region will certainly decrease as the probe molecule is larger.
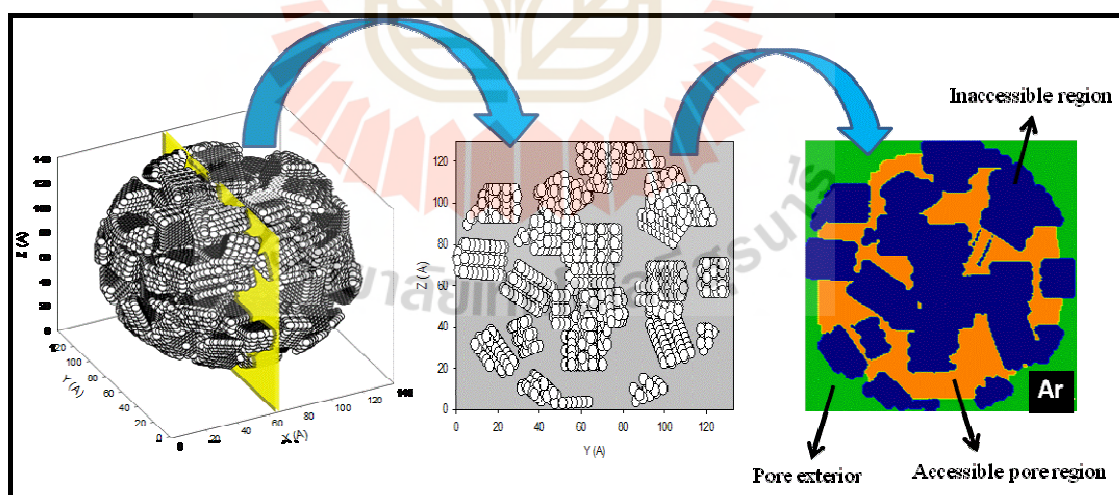
(a) (b) (c)

Figure 3.10 (a) 3D-structure of simulated porous carbon, (b) 2D-snapshot at the middle of the structure (the section between two yellow planes), and (c) 2D-contour of accessible pore region when argon is used to probe.
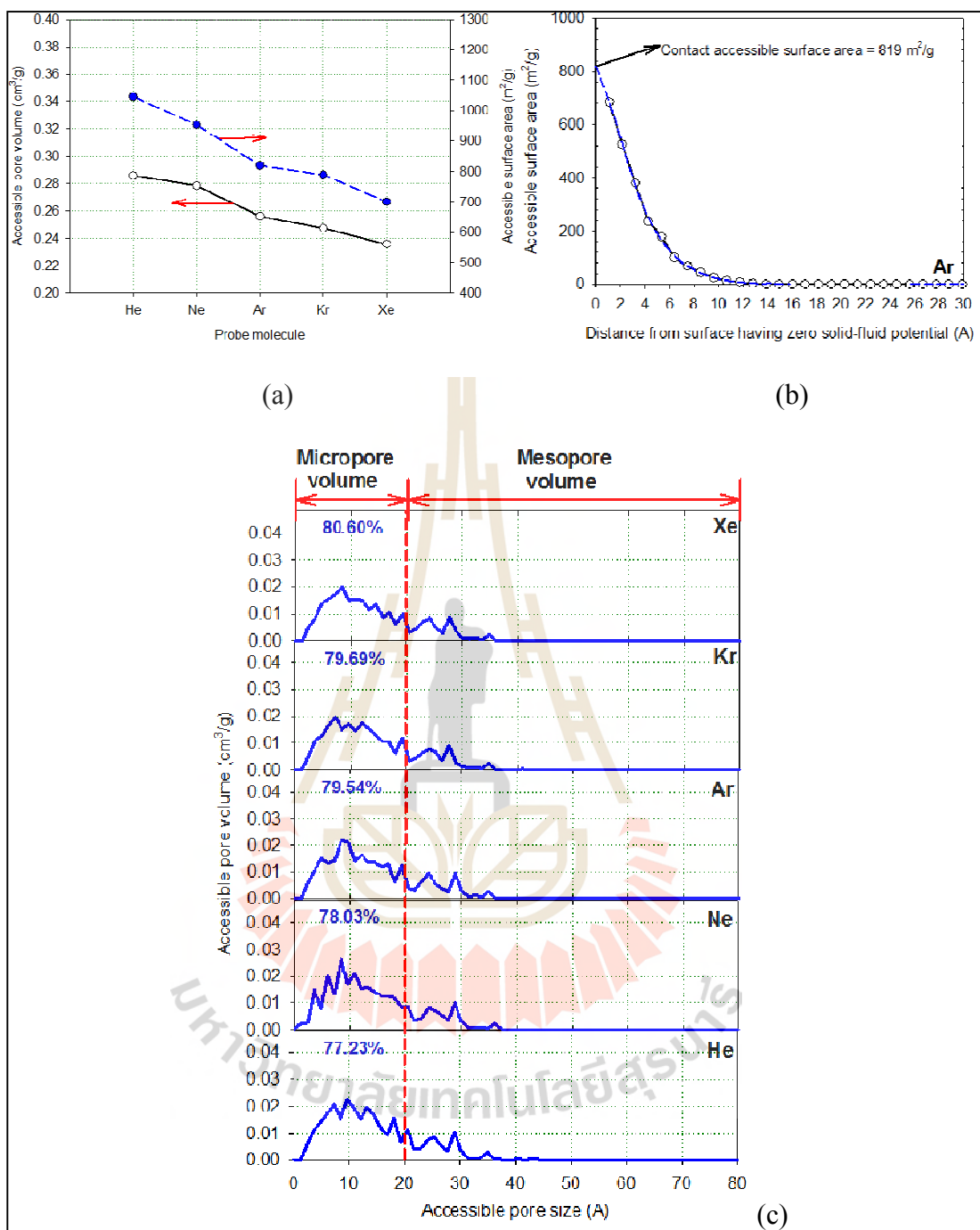
Figure 3.11 (a) Accessible pore volume and surface area of different probe molecules, (b) the illustration for determining accessible surface area of argon, and (c) accessible pore size distribution with percentage of micropore of different probe molecules of simulated porous carbon.

The accessible pore volume and surface area of simulated porous carbon with different noble gases are presented in Figure 3.11a. These trends are consistent with those of cylindrical and wedge pores, where these properties decrease because of the reduction of accessible volume space with the bigger probe molecule. The variation of surface area with the distance from the surface is shown for argon in Figure 3.11b. Unlike the cylindrical and wedge pores, the area decreases abruptly with increasing distance, indicative of higher degree of confinement.

Figure 3.11c presents the pore size distributions of simulated porous carbon with different noble gases. It is clear that the simulated porous carbon is mostly occupied by the volume of micropore with a broad distribution around the center core of carbon structure, followed by the mesopore being connected to the pore exterior. With regard to the effects of increasing probe size, it is not surprising that the percentage of micropore volume, as well as the location of highest peak, slightly shift to lower values; this is because the accessible pore region is contracted with larger probe molecules.

Consideration of adsorption isotherms of Ar, N_2 and CO_2 in Figure 3.12a reveals that the isotherms exhibit Type Ib according to the new IUPAC Classification; this conforms to the derived pore size distribution. With the indication of mesopore range, the hysteresis loops of argon and nitrogen adsorption at their boiling points might be found from this carbon structure.

(a)   (b)
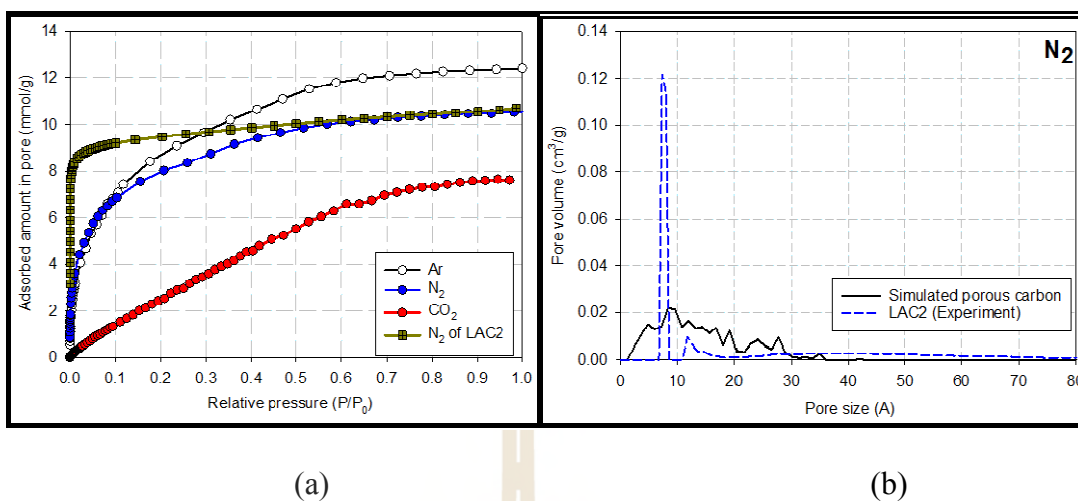
Figure 3.12   (a) Adsorption isotherms of argon (87 K), nitrogen (77 K) and carbon dioxide (273 K) gases for simulated porous carbon and longan seed-derived activated carbon (LAC2). (b) Pore size distribution of experimental activated carbon and simulated porous carbon by probing with nitrogen gas.

Table 3.1   Textural properties of longan seed-derived activated carbon and simulated porous carbon using nitrogen as a probe molecule.

Textural properties	Simulated porous carbon	Activated carbon (LAC2)
Total pore volume (cm^3/g)	0.2527	0.37
Surface area (m^2/g)	825.10	705.00
Micropore volume (cm^3/g)	0.2004 (79.30%)	0.26 (70.27%)
Mesopore volume (cm^3/g)	0.0523 (20.70%)	0.11 (29.73%)

We also compare our results with the actual experimental results of activated carbon derived from longan seed as reported by Junpirom et al. (2008). It is found that the shape of N_2 adsorption isotherm of simulated porous carbon in Figure 3.12a qualitatively agree with that of LAC2, as well as pore size distribution shown in

Figure 3.12b and with comparable total pore volume and surface area as shown in Table 3.1. For LAC2, it was prepared from longan seed by two-step CO_2 activation at 850˚C activating temperature for 60 minutes, giving the degree of char burn-off of 26%. This confirms that the porous properties of our simulated porous carbon resemble those of activated carbon produced at low degree of activation. Performing to the experimental adsorption isotherm, it is noted that the simulated porous carbon should be constructed to give narrower micropore size distribution in order that the isotherm at low pressure could be shifted closer to the isotherm of actual activated carbon. However, the simulated results provide reasonably good description of larger proportion of micropore volume as compared to the mesopore volume. Further works will be directed toward studying the effect of structural parameters of simulated porous carbon including fragment length, number of graphene layers, number of microcrystallites and surface heterogeneity on pore characteristics and adsorption isotherms.

3.6 Conclusions

In this work, the TriPOD technique has been extended for the determination of the accessible pore volume, surface area and pore size distribution for porous carbon with known atomistic configurations. Apart from the random insertion, the developed procedure places a probe particle onto every fine grid distributing in the simulation box. The method is successfully applied to several simple models of porous carbon which are normally used in molecular simulation. We have recommended that this method is faster than the previous one on the subject of computational cost.

Furthermore, we have also demonstrated the validity of this method for estimating the textural properties of simulated porous carbon created by assembling carbon microcrystallites in a random manner. The gathered results of porous properties and adsorption isotherms indicate that the obtained carbon model conforms qualitatively to the biomass-derived activated carbon with low degree of activation. In this respect, the molecular model of porous is still needs to be further developed in order to simulate the adsorption behavior of practical porous carbons by studying the effects of such parameters as the structural properties of microcrystallites, surface heterogeneity and temperature.

3.7   References

Brunauer, S., Emmett, P. H. and Teller, E. (1938). Adsorption of gases in multimolecular layers, **Journal of the American Chemical Society**, 60: 309-319.

Castello, D. L., Amoros, D. C. and Solano, A. L. (2004). Usefulness of CO_2 adsorption at 273 K for the characterization of porous carbons, **Carbon**, 42: 1233-1242.

Connolly, M. L. (1983). Analytical molecular surface calculation, **Journal of Applied Crystallography**, 16: 548-558.

Do, D. D. and Do, H. D. (2003). Pore characterization of carbonaceous materials by DFT and GCMC simulations: A review, **Adsorption Science and Technology**, 21: 389-423.

Do, D. D. and Do, H. D. (2007). Appropriate volumes for adsorption isotherm studies: the absolute void volume, accessible pore volume and enclosing particle volume, **Journal of Colloid and Interface Science**, 316: 317-330.

Do, D. D., Herrera, L. F. and Do, H. D. (2008). A new method to determine pore size and its volume distribution of porous solids having known atomistic configuration, **Journal of Colloid and Interface Science**, 328: 110-119.

Do, D. D., Herrera, L. F. and Nicholson, D. (2011) A method for the determination of accessible surface area, pore volume and its volume distribution for homogeneous pores of different shapes, **Adsorption**, 17: 325-335.

Duren, T., Millange, F., Ferey, G., Walton, K. S. and Snurr, R. Q. (2007). Calculating geometric surface areas as a characterization tool for metal-organic frameworks, **The Journal of Physical Chemistry**, 111: 15350-15356.

Franklin, R. E. (1951). Crystallite growth in graphitizing and nongraphitizing carbons, **Proceedings of the Royal Society of London**, 209: 196-218.

Herrera, L. F., Junpirom, S., Do, D. D. and Tangsathitkulchai, C. (2009). Computer synthesis of char and its characterization, **Carbon**, 47: 839-849.

Herrera, L., Do, D. D. and Nicholson, D. (2010). A Monte Carlo integration method to determine accessible volume, accessible surface area and its fractal dimension, **Journal of Colloid and Interface Science**, 348: 529-536.

Junpirom, S., Tangsathitkulchai, C., Tangsathitkulchai, M. and Ngernyen, Y. (2008). Water adsorption in activated carbon with different burn-offs and its analysis using a cluster model, **Korean Journal of Chemical Engineering**, 25: 825-832.

Kruk, M., Jaroniec, M. and Sayari, A. (2000a). Nitrogen adsorption study of MCM-41 molecular sieves sysnthesized using hydrothermal restructuring, **Adsorption-Journal of the International Adsorption Society**, 6: 47-51.

Kruk, M. and Jaroniec, M. (2000b). Accurate method for calculating mesopore size distributions from argon adsorption data at 87 K developed using model MCM-41 materials, **Chemistry of Materials**, 12: 222-230.

Madani, S. H., Badalyan, A., Biggs, M. J. and Pendleton, P. (2015a). Uncertainty in pore size distribution derived from adsorption isotherms: I. classical methods, **Microporous and Mesoporous Materials**, 214: 210-216.

Madani, S. H., Diaz, L. H., Biggs, M. J. and Pendleton, P. (2015b). Uncertainty in pore size distribution derived from adsorption isotherms: II. Adsorption integral approach, **Microporous and Mesoporous Materials**, 214: 217-223.

Neimark, A. V., Ravikovitch, P. I., Grun, M., Schuth, F. and Unger, K. K. (1998). Pore size analysis of MCM-41 type adsorbents by means of nitrogen and argon adsorption, **Journal of Colloid and Interface Science**, 207: 159-169.

Rouquerol, F., Rouquerol, J. and Sing, K. (1999). **Adsorption by powders and porous solids**. Academic Press: London.

Zeng, Y., Phadungbut, P., Do, D. D. and Nicholson, D. (2015). Wedge pore as an alternative to the uniform slit pore model for the determination of pore size distribution in activated carbon, **The Journal of Physical Chemistry C**, 119: 25853-25859.

CHAPTER IV

2D-TRANSITION ON GRAPHITE AND IN SLIT PORES

4.1   Abstract

The phase evolution of argon adsorbed in open end graphitic slit pores at temperatures below the 2D-critical temperature of the first layer was simulated using the grand canonical Monte Carlo (GCE) and meso-canonical ensembles (MCE). In the latter the adsorption system is connected to a finite reservoir and the combined system is a canonical ensemble. Hysteresis loops and sigmoid van der Waals loops were found for the GCE and MCE simulations respectively, corresponding to the observed 2D-transitions, which comprised vapor-solid, vapor-liquid and liquid-solid changes of state depending on the temperature. The MCE isotherms in the large open end pores exhibited a sequential adsorption, not previously noted in the literature, where the monolayer filling on one wall is followed by monolayer filling on the opposite wall, giving rise to a double van der Waals loop. When the spacing between the pore walls is decreased, this double-vdW loop evolves to form a fused single loop, and the transition shifts from being predominantly a surface adsorption to pore volume filling.

4.2 Introduction

2D-transitions in the layering adsorption of simple gases on graphite at low temperatures have been extensively studied. At temperatures below the 2D-triple point, a 2D-transition occurs between the rarefied and dense phases on the surface. In the temperature range between the 2D-triple point and the 2D-critical temperature there are 2D gas-liquid and 2D liquid-solid transitions, depending on the tangential pressure (Ustinov and Do, 2012a). Above the 2D-critical temperature there is only a 2D hypercritical fluid-solid transition, which is referred to as an ordering transition (Ustinov and Do, 2012b, 2013a,b). Experimentally, the triple point and critical temperatures for the first layer of argon adsorbed on graphite, have been reported to be around 47.2 K and 58 K, respectively (Choi et al., 2006).

Adsorption in a confined space is typically modeled using simple geometries, such as slits or cylinders. Hysteresis is generally found in mesopores at temperatures below the 3D-critical temperature (Thommes, 2004; Everet and Haynes, 1973; Evans et al., 1986), but does not usually occur in micropores or in mesopores above the 3D-critical temperature. On the other hand, the confinement effect, as well as the temperature effect, may change the properties of adsorbate layers residing in the pore interior. It is know that the adsorbed layers adjacent to the pore walls differ from higher layers. In recent communications, Ustinov and Do (2013b) used kinetic Monte Carlo to investigate the 2D-transition. They found the van der Waals-like (vdW) loop during the 2D-transition.This is an indication of the existence of hysteresis loop on the surface.

In this chapter, the evolution of the phase transition and microscopic behavior of argon adsorbed on a graphitic surface and in open end slit pores of various pore sizes at temperatures below the 2D-critical temperature of the first layer.

4.3 Simulation

The conventional Grand Canonical Monte Carlo (GCE) and the meso-canonical (MCE) ensembles were employed. For each point on the isotherm, 50,000 cycles, each of length 1,000 configurations, were run in both the equilibration and sampling stages. The solid-fluid interaction energy for a graphitic slit pore in infinite extent was calculated from the Steele 10-4-3 equation and the argon-argon interaction potential was calculated from the Lennard-Jones 12-6 equation.

4.4 Results and Discussion

4.4.1 Monolayer Adsorption onto Graphite and into a Large Open End Slit Pore

We first investigated the differences between monolayer adsorption of argon onto a square graphitic surface of $20\sigma_{ff} \times 20\sigma_{ff}$ with a hard wall at the opposite boundary, and into an open end graphitic slit pore of $20\sigma_{ff} \times 20\sigma_{ff} \times 8$ nm with the MCE simulation. The temperature was 55 K, which is below the 2D-critical temperature of the first layer. The isotherms and the local density distributions for these two cases are shown in Figure 4.1.

We see that the MCE isotherm obtained for the slit pore exhibits two vdW loops whose size and shape are the same and, most importantly, they occur over the same range of pressure as the transition on the graphite. The first loop is

associated with the unstable branch of a canonical isotherm for one surface. This is verified by the local density distributions for points A-C and D-F along the first and second vdW loops, respectively (Figure 4.1b). In the MCE, molecules build up on one surface first (because once a few molecules are laid down on one surface, the combined effect of fluid-fluid and fluid-solid interactions are stronger than the fluid-solid interaction alone) before moving onto the second surface. This process is similar to that reported by Gor et al. (2012) in their MCE simulation study of the 3D-transition of nitrogen adsorption in overlapping spheres, where it was found that filling was completed inside one sphere while only one or two layers were adsorbed in the connected sphere.

4.4.2 Effects of Temperature for a Large Open End Pore

The effects of temperature on argon adsorption in the open end graphitic slit pore with dimensions $20\sigma_{ff} \times 20\sigma_{ff} \times 8$ nm, at temperatures ranging from below to above the 2D-critical temperature of the first layer, are shown in Figure 4.2 as plots of surface excess versus the absolute pressure. A number of interesting points may be noted:

1. There is no phase change at 77 K and 87 K as these temperatures are above the 2D-critical temperature.

2. At 40 K and 45 K, which are temperatures below the 2D-triple point, vapor-like (V) and solid-like (S) states can be identified in the meso-canonical isotherms, corresponding to the vapor-solid transition.

3. At 50-60 K, the vapor-like (V) and the liquid-like (L) and the solid-like (S) spinodals are found along the unstable branch, indicative of vapor-liquid and liquid-solid transitions.

(a)

(b)
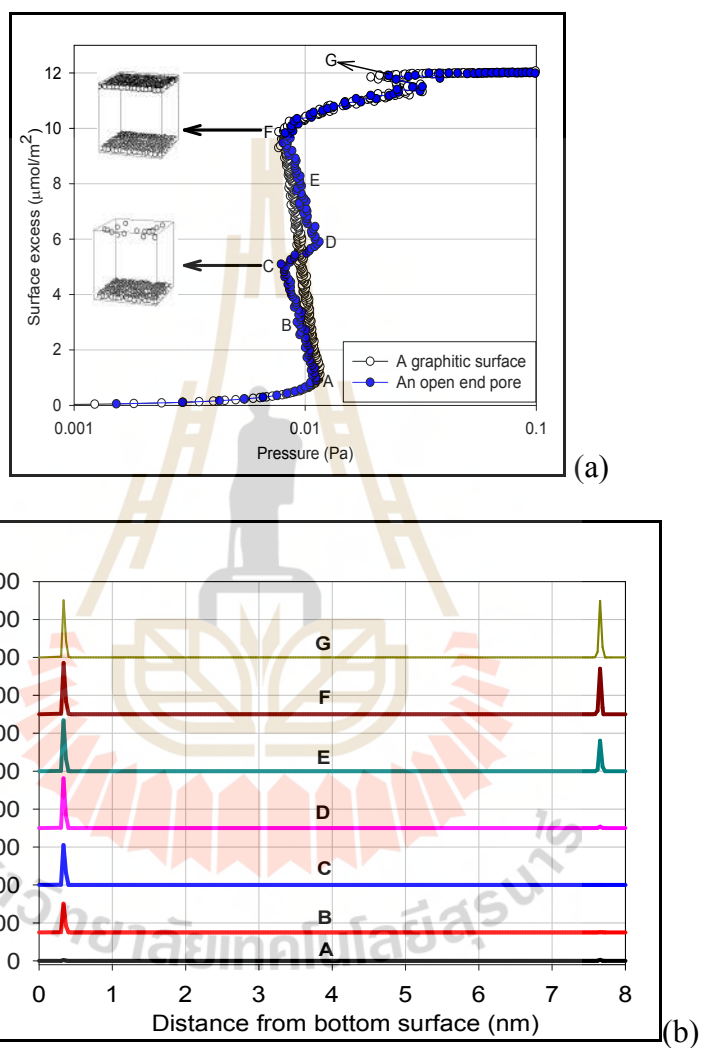
Figure 4.1   (a) MCE isotherms of argon adsorption onto a square graphite and an open slit pore of 8 nm width at 55 K. (b) Plots of the local density distribution as a function of distance across the pore at points along the isotherm.
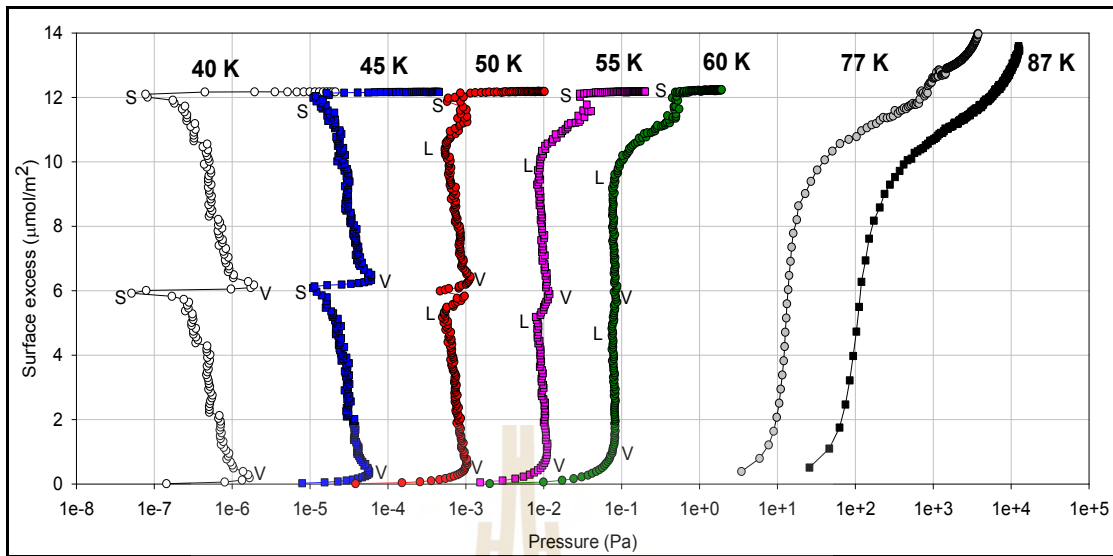
Figure 4.2   Argon adsorption isotherms in the graphitic slit pore of $20\sigma_{ff} \times 20\sigma_{ff}$ x

8 nm at temperatures ranging from 40 to 87 K.

To shed further light on how argon adsorption adsorbed on the two

walls of the pore at temperatures below 2D-critical temperature, we chose two cases:

(1) T = 40 K to study the vapor-solid transition and (2) T = 55 K to study the vapor-

liquid and liquid-solid transitions.

4.4.3 Vapor-Solid Transition of Argon in the Adsorbed Monolayer

The GCE and MCE isotherms at 40 K and the vapor-solid transition

obtained with the mid-density scheme are shown in Figure 4.3. To obtain the MCE

isotherm, we used a dosing reservoir having a linear dimension of 10^4 nm and a

dosing increment of 2 molecules.

The MCE isotherm in Figure 4.3a shows two distinct vdW loops

occurring over the same range of pressure, which implies that each loop is associated

with the vapor-solid transition for one surface as discussed in Section 4.4.1. On the

transition on the first wall, the solid-like cluster, circular in shape, surrounded by the

rarefied fluid grows from the vapor-like spinodal point up to Point A. As loading is further increased to Point B the circular cluster changes into a strip. Beyond this point, the strip grows larger at the expense of the rarefied phase, but the coexistence of the two phases is retained, resulting in a vertical segment at the same pressure. After this the rarefied phase decreases in size and increases in density, resulting in the second unstable segment until Point C (solid-like spinodal) is reached. At this point the rarefied phase disappears and the wall is completely filled with adsorbate molecules. Once this has been achieved, the same process occurs for the other wall, marked by the portion DEF of the isotherm in Figure 4.3a.

In contrast to the MCE isotherm, the GCE isotherm (solid line in Figure 4.3a) shows a hysteresis loop whose vertical boundaries are due to large fluctuations that overcome the free energy barrier that the separates the phases. These fluctuations result in a switch from one phase to the other before the spinodal point has been reached.

The two vertical segments in the MCE isotherm reflect the phase coexistence between the gas and solid phases for the two surfaces. This is substantiated by the first order vapor-solid transition found using the mid-density scheme, shown as the dashed line in Figure 4.3a, and coinciding exactly with the two vertical segments in the MCE isotherm.
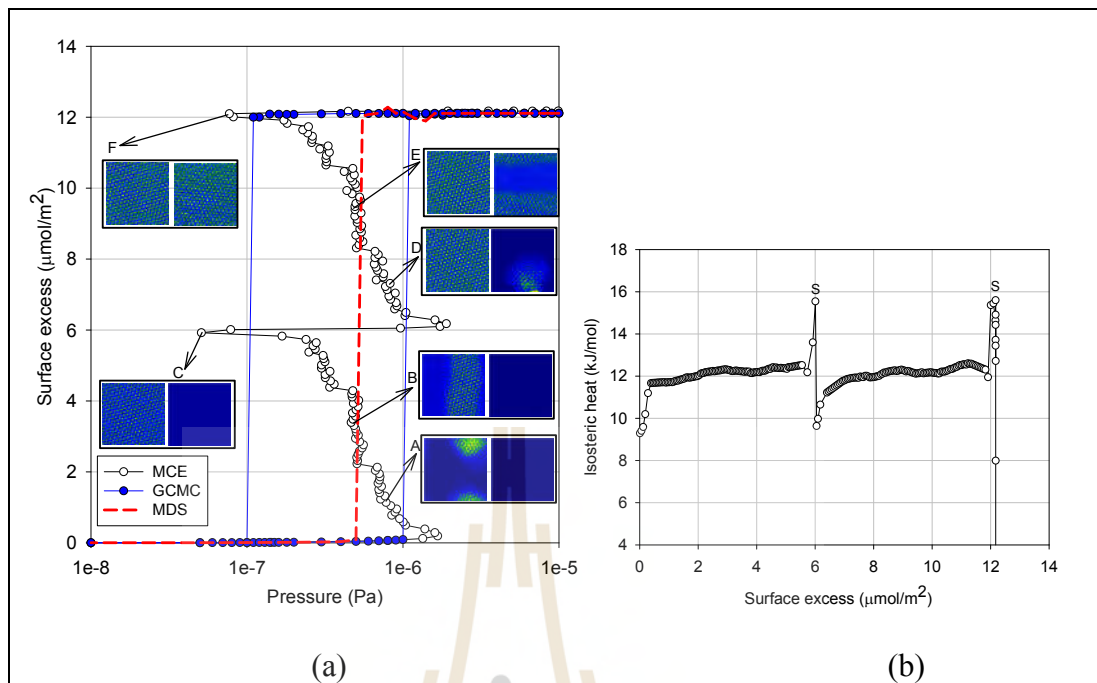
Figure 4.3 (a) Adsorption isotherm of whole system and 2D-density profiles of
top (left panel) and bottom (right panel) walls and (b) isosteric heat of
argon in an open end pore of $20\sigma_{ff} \times 20\sigma_{ff}$ x 8 nm at 40 K. "S" stands
for solid-like state.

The isosteric heat obtained with the MCE ensemble is shown in Figure 4.3b.
There are two regions of constant heat (12.1 kJ/mol), corresponding to the vapor-solid
transitions on the walls, in qualitative agreement with the results obtained by Ustinov
and Do (2013b). The magnitudes of the two peaks in the isosteric heat for the two
walls at 40 K, which occur when where the first layer is completely filled on the wall,
are exactly the same, and correspond to perfect (2D) solid close packing.

4.4.4 Vapor-Liquid and Liquid-Solid Transition of Argon in the Adsorbed Monolayer

Vapor-liquid and liquid-solid transitions at 55 K were observed for argon adsorbed in the first layer on each wall. Figure 4.4 shows the MCE and GCE isotherms. A cubic dosing reservoir with a linear dimension of 10^3 nm and dosing increment of 2 molecules were sufficient to obtain the unstable branch.

In contrast to the results obtained at 40 K, the MCE isotherm exhibits three consecutive vdW loops: the first and second ones are for the sequential evolution of the vapor and liquid phases on the two walls, while the third loop, which is much smaller in size, represents the liquid-solid transition on each wall. The 2D-density profiles in Figure 4.4a show the evolution of the configurations in the first layer. At Point A, liquid droplets are formed on one surface and spread over the surface as loading is increased up to Point B and finally to Point C, where the surface is covered with a 2D-liquid like adsorbate. This sequence is then repeated on the other surface (Points D-F). Further increase in loading from Point F results a transition of adsorbate on the two walls to a solid-like state at the solid spinodal point.

The three vdw loops observed in the MCE simulation are translated to two hysteresis loops in the GCE isotherm, corresponding to the vapor-liquid (large loop) and liquid-solid (small loop) transitions.

The equilibrium transition obtained with the mid-density scheme (dashed line in Figure 4.4a) was first-order and passes through the middle of the unstable branch. Had the size of the two walls been greater, we would have seen a vertical segment on the unstable branch of the MCE isotherm and the first order equilibrium transition would pass through these vertical segments.
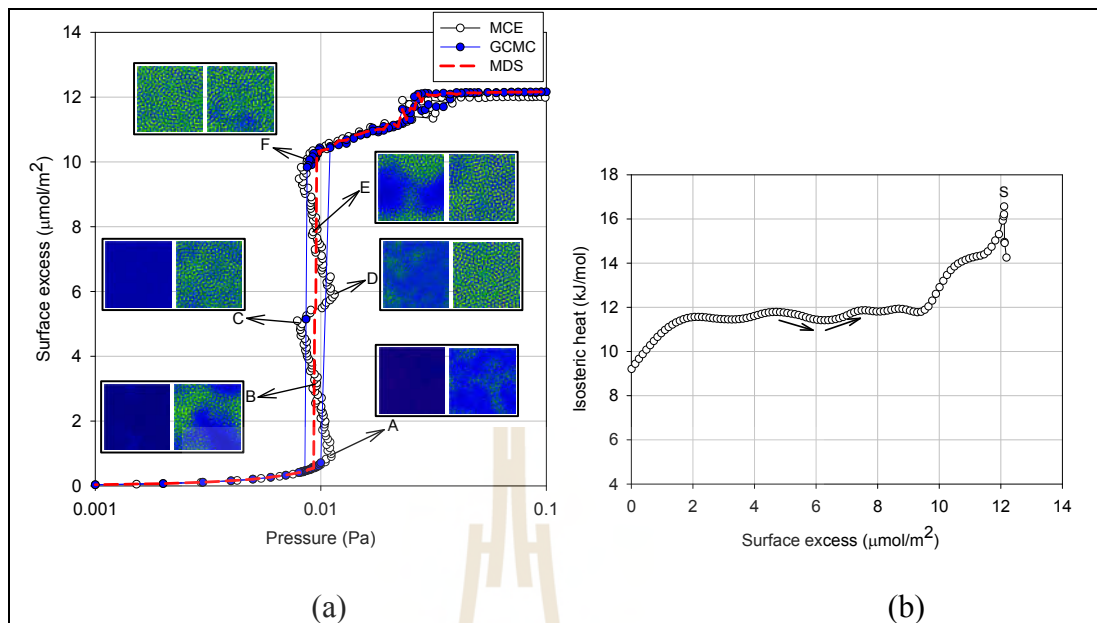
Figure 4.4   (a) Adsorption isotherm of whole system and 2D-density profiles of top (left panel) and bottom (right panel) walls and (b) isosteric heat of argon in an open end pore of $20\sigma_{ff} \times 20\sigma_{ff}$ x 8 nm at 55 K. "S" stands for solid-like state.

We have earlier made the argument that the solid-liquid transitions on the two walls occur simultaneously instead of sequentially. This argument is substantiated by the isosteric heat curves shown in Figure 4.4b, where there is a single peak (marked as S) at the loading where the liquid-solid transition occurs. On the other hand, there are two regions on the heat curve corresponding to the separate vapor-liquid transitions on each wall. The constant heat at the gas-liquid transition is 11.7 kJ/mol, which is in perfect agreement with the result obtained by Ustinov and Do (2013b).

4.4.5   Effect of Pore Width

When the two surfaces are moved closer to each other, a correlation between them develops and adsorption on one wall is affected by the state of the adsorbate on the opposite wall. Using MCE simulation, we have studied widths varying from 8 nm where the first layer adsorption on the two walls is in dependent, to 1 nm where the pore can accommodate only two integral layers of molecules, and where there is strong correlation between the two opposing layers. In this range, the evolution of the vdW loop can be classified into four groups.

4.4.5.1 Group I: The Evolution of Double vdW Loops

Figure 4.5 shows the MCE isotherms for argon at 40 K for pore widths in the range 1.5-8 nm and those for 55 K for pore widths in the range 1.7-8 nm. At 40 K, a cubic dosing reservoir having a linear dimension of 10^4 nm and a dosing increment of 2 molecules were required to trace the unstable portion of the isotherm. On the other hand, at 55 K, a smaller volume of the dosing reservoir of 10^3 nm and a dosing increment of 2 molecules were sufficient.

The MCE isotherms in this group show double vdW loops, similar to those discussed in the last sections. However, a number of interesting points are particularly noted when the pore width is decreased:

(1)   All spinodal points are shited to lower pressure as denoted by the solid arrow in Figure 4.5. For the vapor-like spinodal points to occur at lower pressure, the driving force has to be the density of the gas-like core in the middle of the pore, i.e. the core is more compressed that the bulk gas phase. This is indeed the case as illustrated in Figure 4.6 where we show the density in the core as a function of pressure at 55 K.
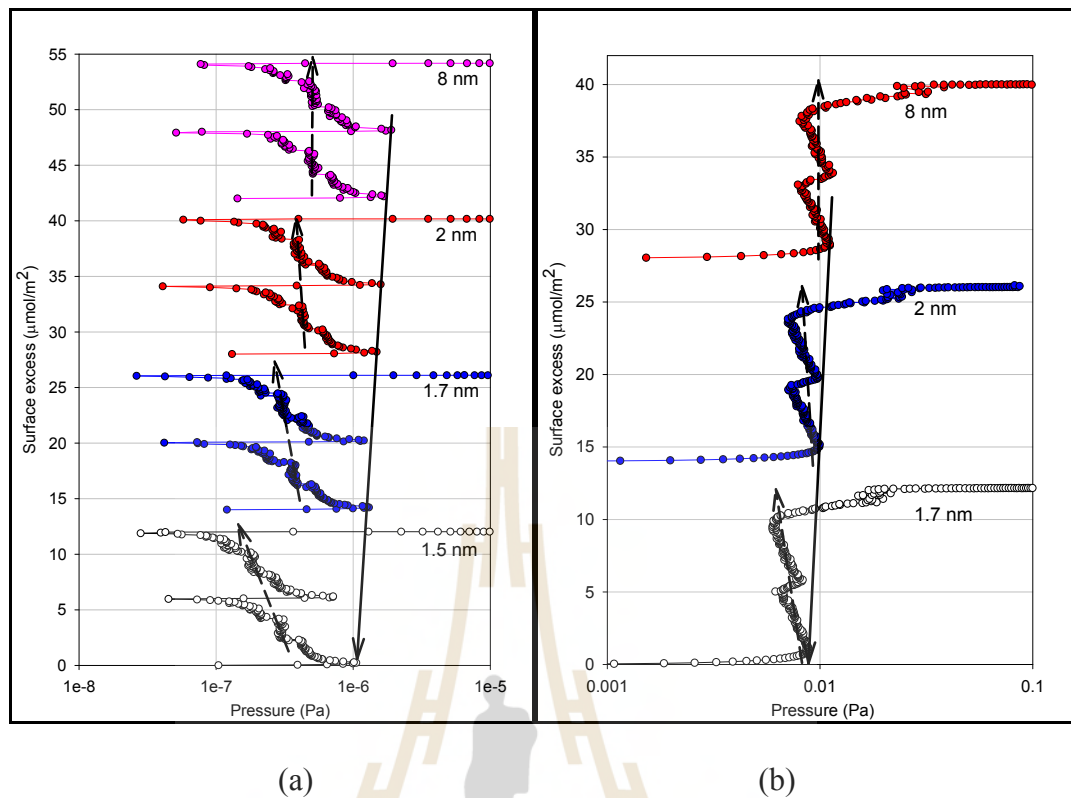
Figure 4.5   MCE isotherms of argon adsorption in open end pores having two opposite square walls of $20\sigma_{ff} \times 20\sigma_{ff}$ with pore widths ranging from (a) 1.5-8 nm at 40 K and (b) 1.7-8 nm at 55 K. As the pore width is reduced, the solid arrows show the evolution of position of the first vapor-like spinodals. The dashed arrows represent the evolution of intermediate states.
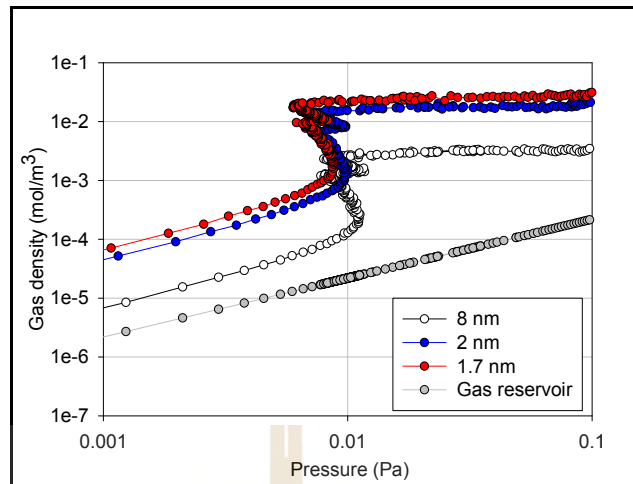
Figure 4.6   Gas density versus pressure between monolayer of argon adsorption at 55 K in the core of an open end pore with different pore widths.

(2)   Once the monolayer on one wall has been completed, the monolayer on the opposite wall forms at a lower pressure now interact with the previously formed monolayer, and with the "compressed" gas in the middle of the pore, in addition to the adsorbent wall.

(3)   Figure 4.7 shows the 2D-density profiles along the MCE isotherms at 40 K and 55 K for the 1.7 nm pore. The microscopic behavior of the vapor-solid transition at 40 K and the vapor-liquid and liquid-solid transitions at 55 K are similar to that in the larger pore (8 nm), as discussed in Section 4.4.3 and 4.4.4.
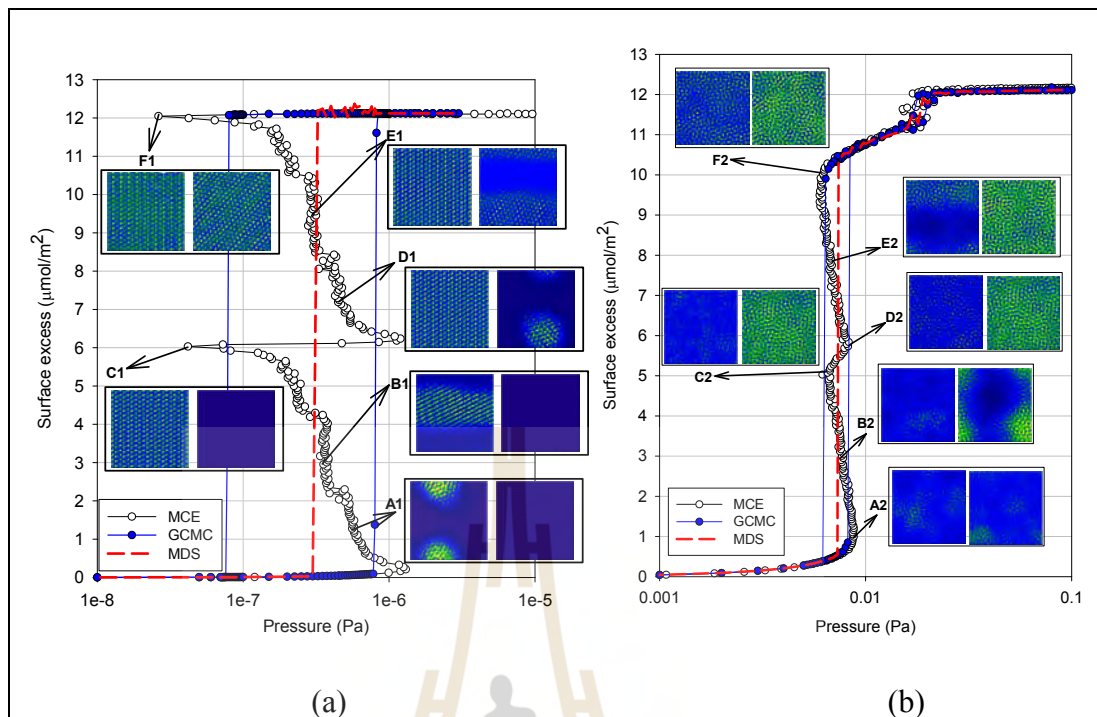
Figure 4.7   Argon adsorption isotherms and 2D-contour plots of top (left) and bottom (right) walls at (a) 40 K and (b) 55 K in an open end pore of $20\sigma_{ff} \times 20\sigma_{ff} \times 1.7$ nm.

4.4.5.2   Group II: Pore Width of 1.5 nm at 55 K

The MCE and GCMC isotherms in the 1.5 nm pore at 55 K are shown in Figure 4.8. In contrast to the wider pores, where there are double vdW loops, here there is only a single loop for the vapor-liquid transition. Although this is similar to adsorption on a single graphitic surface, the transition is at a much lower pressure and results from simultaneous adsorption on the two walls. The local density distribution across the 1.5 nm pore, shown in Figure 4.8b, confirms this mechanism.
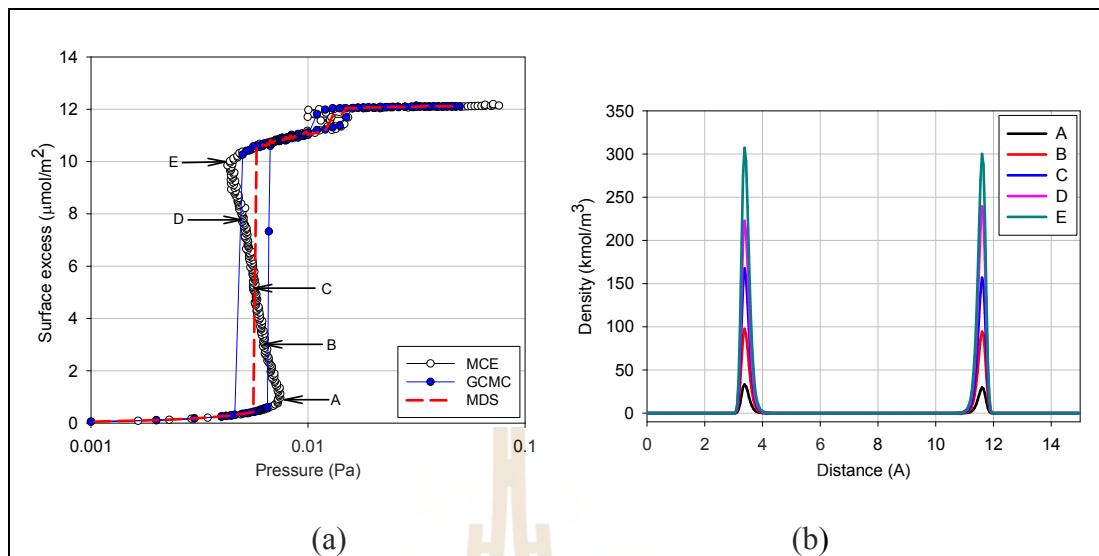
Figure 4.8 (a) Adsorption isotherms and (b) local density distribution along the pore width of argon at 55 K in open end pores of $20\sigma_{ff} \times 20\sigma_{ff} \times 1.5$ nm.

4.4.5.3 Group III: Pore Width of 1.3 nm

In this group, the isotherms at 40 K and 55 K are shown in Figure 4.9. The MCE isotherms were obtained with dosing reservoirs of linear dimension 1.2×10^4 nm at 40 K and 10^3 nm at 55 K, and dosing increment of 3 molecules.

When the pore width is decreased to 1.3 nm the condensation shifts to a lower pressure because there is a deeper potential energy between the pore walls. Instead of a 2D-transition at each wall, there are now three layers of molecules which pass through a 3D-transition, typical of micropore volume filling as seen in the local density distribution plotted in Figure 4.10.
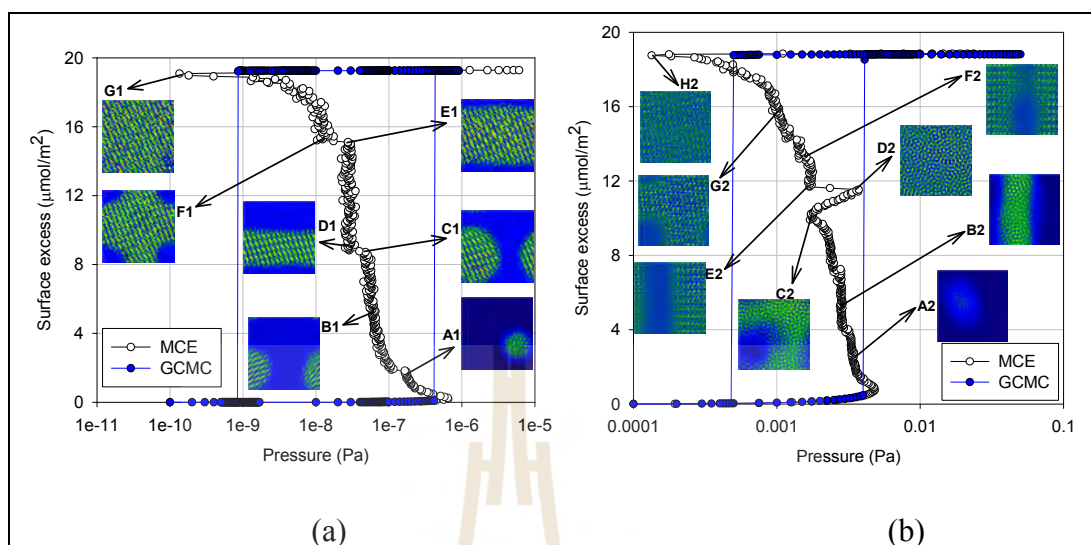
Figure 4.9 Argon adsorption isotherms and 2D-density profiles at (a) 40 K and (b) 55 K in an open end pore of $20\sigma_{ff} \times 20\sigma_{ff} \times 1.3$ nm.
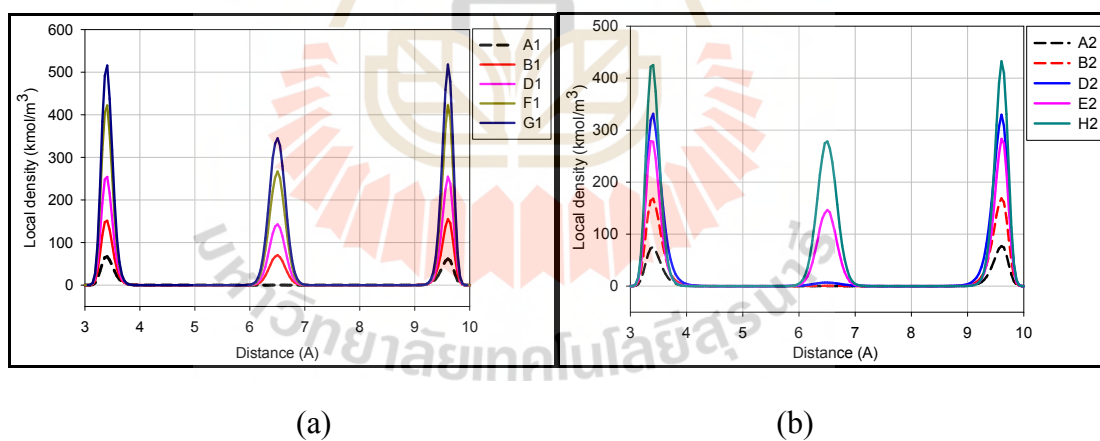
Figure 4.10 Local density distributions across the pore for argon at (a) 40 K and (b) 55 K in an open end pore of $20\sigma_{ff} \times 20\sigma_{ff} \times 1.3$ nm. The labels are indicated in Figure 4.9.

At 40 K, there are only two spinodal points on the MCE isotherm: vapor-like and solid-like. From the vapor-like spinodal point to Point A1, circular solid-like clusters are initially formed on the two walls with an insignificant number of molecules in the central core (see the local density distribution in Figure 4.10a). As the loading is increased to Point B1, these clusters grow larger, together with the onset of the central layer. This represents the switch from a 2D-transition to 3D-transition. We noted that there is a vertical segment from D1 to E1, which represents the co-existence of the 3D-gas and solid phases, instead of the 2D-gas and solid phases for the larger pores dealt with in Section 4.4.1.

At 55 K, adsorption proceeds by filling the first layers on the two surfaces, followed by adsorption in the middle layer as seen in Figure 4.10b. This raises questions about the nature of the phases during this transition, and whether this is a mixture of 2D- and 3D-transitons? To address these questions, we show the layer compressibility for the three layers in Figure 4.11. The vertical steps in the compressibility curves suggests that two transitions, vapor-liquid and liquid-solid, are occurring in the first layers at the two walls, and a single vapor-solid transition in the middle layer; the latter because of the presence of the potential energy field from the two first layers. Microscopically, the liquid-like droplets on both walls grow from the gas-like spinodal point up to Point A2 (Figure 4.9b), and then the configuration changes from 2D-droplets to a strip at B2, and as the loading is increased to C2 the 2D-rarefied phase becomes smaller in size and changes to 2D-bubbles. These bubbles reduce in size and eventually the two walls are covered with a 2D-liquid at Point D2. From E2 to H2, the middle layer evolves along the MCE isotherm from a solid-like strip to a structured solid-like configuration.
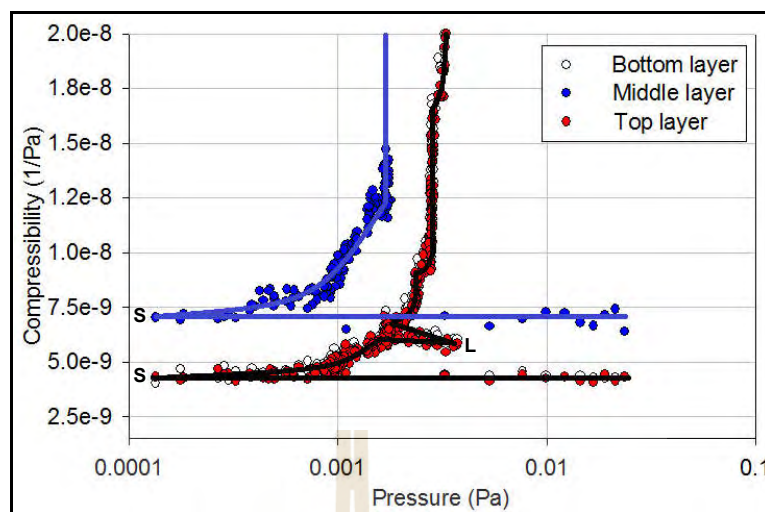
Figure 4.11 Layer compressibility for argon adsorption in an open end pore of $20\sigma_{ff} \times 20\sigma_{ff} \times 1.3$ nm at 55 K. "L" and "S" stand for liquid-like and solid-like states. The lines are guided to the eye.

4.4.5.4 Group IV: Pore Width of 1.0 nm

Isotherms at 40 K and 55 K for a pore of 1 nm width are shown in Figure 4.12 (this pore can accommodate only two layers.) The MCE isotherms were obtained from a cubic dosing reservoir of 1.2×10^5 nm for 40 K and 5×10^3 nm for 55 K with a dosing increment of 3 molecules. Both isotherms show two spinodal points: vapor-like and solid-like. The mechanisms are similar to those discussed earlier for 1.3 nm pore at 40 K.
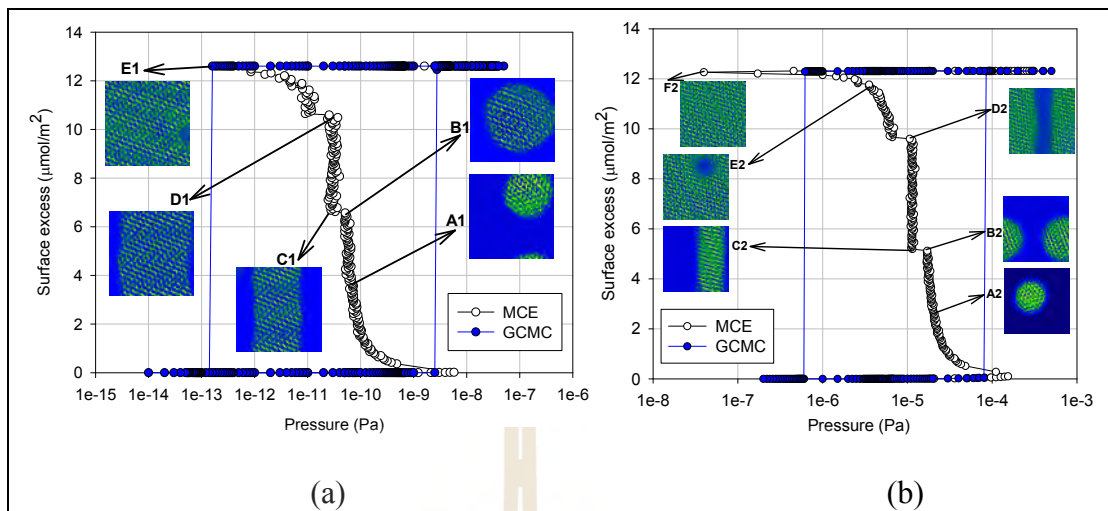
Figure 4.12   Argon adsorption isotherms and 2D-density profiles at (a) 40 K and (b) 55 K in an open end pore of $20\sigma_{ff} \times 20\sigma_{ff} \times 1.0$ nm.

4.5   Conclusions

We have used MCE and GCE simulation to study argon monolayer adsorbed on graphite and in graphitic slit pores of widths ranging from 1 nm to 8 nm and at two temperatures, 40 K and 55 K, both of which are below the 2D-critical temperature. The results are displayed as isotherms, isosteric heats and snapshots showing the local structure of the adsorbate at different stages of the adsorption. Our results can be classified into 4 groups: In the first group, with pore widths between 1.5 nm (at 40 K) or 1.7 nm (at 55 K), the MCE simulations proceed through a double sigmoidal loops each loop being associated with adsorption on one surface during 2D-transition in contrast to a similar study of adsorption on a homogeneous graphitic surface, and the spinodal points shift to a lower pressure as pore width is decreased. The second group is typified by a pore of width 1.5nm at 55 K; here there is only a single loop because the interactions with the central core have a significant effect. In the third group of

narrower pores (width 1.3 nm) three layers of molecules form and the system passes through a 3D-transition, typical of micropore volume filling. A study of the compressibility suggests that two transitions, vapor-liquid and liquid-solid, are occurring in the first layers at the two walls, followed by a transition of rearrangement of molecules in the first layers. The fourth group comprises pores of only 1 nm width and the isotherms show two spinodal points: vapor-like and solid-like.

4.6   References

Choi, B.I., Nham, H.S., Kwon, S.Y. and Kim, J.C. (2006). Phase diagram of a physisorbed argon monolayer on graphite. **Journal of the Korean Physical Society**. 49: 2348-2352.

Evans, R., Marconi, U.M.B. and Tarazona, P. (1986). Capillary condensation and adsorption in cylindrical and slit-like pores. **Journal of the Chemical Society, Faraday Transactions 2**. 82: 1763-1787.

Everett, D.H. and Haynes, J.M. (1973). Capillarity and porous materials: equilibrium properties. **Colloid Science**. 4: 123-172.

Gor, G.Y., Rasmussen, C.J. and Neimark, A.V. (2012). Capillary condensation hysteresis in overlapping spherical pores: a Monte Carlo simulation study. **Langmuir**. 28: 12100-121007.

Thommes, M. (2004). Physical adsorption characterization of ordered and amorphous mesoporous materials. In: Lu, G., Zhao, X.S. (Eds.). **Nanoporous Materials**. Science & Engineering. Imperial College Press. New Jersey: 317-364.

Ustinov, E.A. and Do, D.D. (2013a). Simulation study of two-dimensional phase transitions of argon on graphite surface and in slit micropores. **Adsorption**. 20: 439-451.

Ustinov, E.A. and Do, D.D. (2013b). Effects of melting and ordering on the isosteric heat and monolayer density of argon adsorption on graphite. **Adsorption**. 19: 291-304.

Ustinov, E.A. and Do, D.D. (2012a). Two-dimensional order-disorder transition of argon monolayer adsorbed on graphitized carbon black: kinetic Monte Carlo method. **The Journal of Chemical Physics**. 136: 134702.

Ustinov, E.A. and Do, D.D. (2012b). Thermodynamic analysis of ordered and disordered monolayer of argon adsorption on graphite. **Langmuir**. 28: 9543-9553.

Zhu, D.M. and Dash, J.G. (1986). Surface melting and roughening of adsorbed argon films. **Physical Review Letter**. 57:2959.

CHAPTER V

UNDULATION THEORY IN

CYLINDRICAL AND SPHERICAL PORES

5.1   Abstract

The undulation theory, recently developed to explain the mechanism of the onset of condensation in an open end slit pore, is extended to investigate the effects of pore diameter, pore wall curvature, temperature, and surface strength on the condensation of argon in cylindrical and spherical pores. Using the concept of an undulating interface separating the adsorbed phase and the gas-like core, we can determine the mean thickness of the adsorbed phase and thus the mean radius of the gas-like core just before condensation. The radius of curvature of the core is used in the Cohan-Kelvin equation, modified to account for the contribution from the solid-fluid interaction (better known as the Derjaguin-Broekhoff-de Boer equation), to derive the interfacial energy parameter. For cylinders and spheres, this parameter is always greater than the bulk phase value, which is used in the unmodified Cohan-Kelvin equation but converges to the bulk value as the pore diameter is increased. For spheres, the energy parameter is smaller than in cylinders of the same diameter but is still higher than the bulk value for pore diameters less than 6 nm. This difference is attributed to packing effects in the 3D-confined spherical geometry. This shows the

interesting interplay between packing effects in 3D-spherical confinement and the cohesiveness of the adsorbate enhanced by the solid-fluid interaction.

5.2   Introduction

The capillary condensation phenomenon in the adsorption of gases in mesoporous materials at temperatures below the critical hysteresis temperature is characterized by a very steep (first-order) change in the density in the adsorption isotherm and is accompanied by a hysteresis loop. This subject has been extensively investigated for several decades because of its importance in the characterization of porosity and pore size distribution in many porous solids with industrial applications (Everett et al., 1973a; Rouquerol et al., 1999; Thommes, 2004). The progress in molecular simulation has greatly improved our understanding of the fundamental physics of confined fluids, from which the correlation between the condensation mechanism and pore morphology, temperature, adsorbate and surface heterogeneity can be established (Horikawa et al., 2011).

In 1973, Everett and Haynes (1973b) pointed out that there are two radii of curvature describing any curved surface and three possible configurations for meniscus curvature. They proposed a mesoscopic thermodynamic mechanism for capillary condensation in cylinders, in which nucleation of the dense adsorbate phase originates from a wave-like undulation, which grows and transforms into liquid bridge bounded by two hemispherical menisci. This led them to argue that the wave-like structure is the origin of the condensation process. The original thermodynamic formulation for condensation in and evaporation from cylinders due to Cohan invoked only two forms of meniscus curvature: cylindrical and spherical with condensation

occurring at the former and evaporation from the latter. The Cohan-Kelvin equations (Cohan, 1938) have been widely applied to describe condensation and evaporation in cylindrical pores, forming the basis for the determination of pore size distribution in the mesopore range. Cohan suggested that the difference in shape between the cylindrical meniscus during adsorption and the hemispherical meniscus during desorption was the reason for the existence of hysteresis. The classical (unmodified) Cohan-Kelvin equations are valid for large pores, where the adsorbate structure is largely that of the bulk liquid at the same temperature. However, in pores of nanodimensions, those equations fail because:

1. the structuring effect, due to the external adsorbent field, extends throughout most of the adsorbate.

2. the constraints of confinement (repulsive forces), especially in cylindrical and spherical geometries, impose limitations on molecular packing.

In attempts to refine the classical equations, it was suggested that condensation occurred at the surface of an adsorbed layer whose statistical thickness, t, could be obtained from adsorption measurements on a nonporous solid with the same surface chemistry. These modifications extend the range of validity of the Cohan-Kelvin equation to smaller pores; however when pores are of nanodimensions, the contribution from the solid-fluid potential cannot be ignored. To this end, the work by Derjaguin (1992) and Broekhoff and de Boer (DBdB) accounting for the solid-fluid potential at the interface separating the adsorbed phase and the gas-like core provides a significant advance in condensation theory (Broekhoff and de Boer, 1967a; 1967b). Recently, Ustinov et al. (2005) further refined the DBdB model for cylindrical pores

by correcting the potential of a nonporous solid for the curvature of the pore wall, and Kornev et al. (2002) developed a mathematical theory in which the ideas of Derjaguin and the undulating structure of the adsorbate were both incorporated.

In this chapter, using grand canonical ensemble, the extension of the undulation theory is used to describe condensation in cylindrical and spherical pores and to study the effects of pore diameter, pore wall curvature, temperature and surface strength. Using our simulation data, we determine the boundaries of the adsorbed film, of the fluctuation region, and of the gas-like core just before condensation and obtain values for the radius of curvature of the interface separating the adsorbed phase and the gas-like core. This radius of curvature is then used in the Derjaguin-Broekhoff-de Boer equation to determine the interfacial energy parameter.

5.3   Simulation

The argon adsorbate was modeled by the Lennard-Jones 12-6 equation. The adsorbents were cylindrical or spherical pores with graphitic pore walls. The cylindrical pores were infinite in length with periodic boundaries in the axial direction. Both pore models were composed of a single graphitic layer.

In the GCMC simulations, we used 70,000 cycles in the equilibration and sampling stages. Each cycle consisted of 1,000 attempted displacements, insertions or deletions with equal probability.

To analyze capillary condensation with the Derjaguin-Broekhoff-de Boer (DBdB) equation, the radius of curvature of the core needs to be determined, and it is necessary to specify a way to define this parameter in an unambiguous manner. Knowing the profile of particle number fluctuation (PNF) versus the radial distance

we can identify the thickness of the adsorbed layer (d_A), that of the fluctuation region (d_F), and the diameter of the gas-like core (D_{core}). In a recent communication (Phadungbut et al., 2015), we showed that the boundary separating the adsorbate from an adjacent gas-like phase could be located by an equal area construction applied to a fraction of success profile measured during a simulation. The radius of curvature for a liquid meniscus (r^*) can then be defined as the distance from the center of the pore to the midpoint of the fluctuation region, as shown the schematic diagram in Figure 5.1. The radius of curvature, defined in this way, was used in either the DBdB equation.
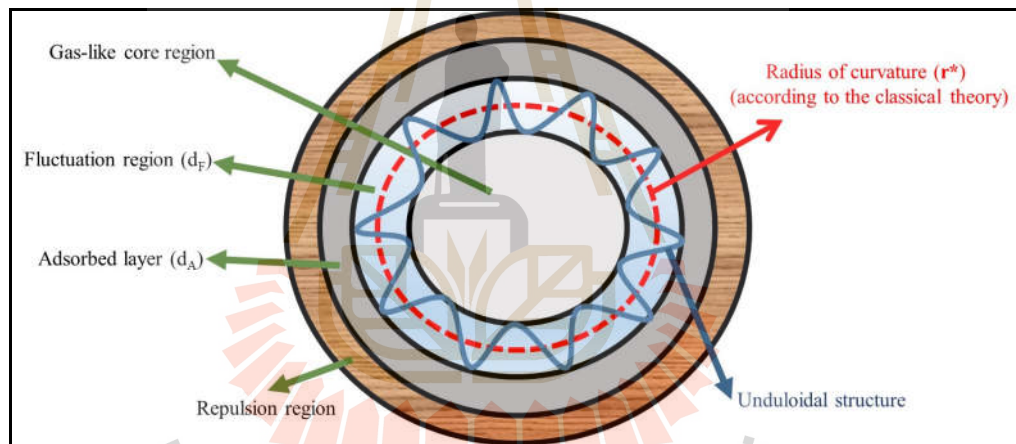
Figure 5.1   Schematic diagram of the adsorbed layer, fluctuation and gas-like regions analyzed by the undulation theory and the definition of the radius of curvature in cylindrical and spherical pores.

The DBdB models include an additional term to account for the solid-fluid potential and may be written in a general form

$$R_g T \ln\left(\frac{P_{cond}}{P_0}\right) = -\sigma v_M C + F_{SF}\left(r^*\right) \tag{4.1}$$

where P_{cond} is the condensation pressure; P_0 is the saturation vapor pressure of the

bulk fluid; σ is the liquid-vapor surface tension; v_M is the liquid molar volume; R_g is

the gas constant; C is the mean curvature of the meniscus separating the condensate

and the gas-like phase; and $F_{SF}(r^*)$ is the contribution from the solid-fluid potential

exerted on molecules at the boundary separating the adsorbed phase and the gas-like

phase by the external field from the solid adsorbent. When this contribution is

negligible, as in very large pores, the DBdB equation reduces to the unmodified

Cohan-Kelvin equation. When the meniscus is cylindrical, $C = 1/r^*$, and for a

spherical meniscus, $C = 2/r^*$. In Table 5.1 we list the simulated interfacial parameters

of the bulk liquid at various temperatures from the literature (Trokhymchuk and

Alejandre, 1999).

Table 5.1 Simulated liquid-vapor surface tension and liquid molar volume of argon
used in this work.

Temperature (K)	Surface tension (mN/m)	Liquid molar volume (L/kmol)	Interfacial product, σv_M (J m/kmol)
87	14.69	28.78	4.227×10^{-4}
100	11.28	30.62	3.455×10^{-4}
110	9.00	32.36	2.911×10^{-4}

5.4 Results and Discussion

5.4.1 Undulation theory for condensation in cylinders and spheres

The adsorption isotherms for argon adsorption at 87 K in a cylinder of 5 nm diameter and a sphere of 6 nm diameter are shown in Figure 5.2 with the local density distribution and particle number fluctuations versus the radial distance at various points marked on the isotherms. Both isotherms exhibit a hysteresis loop of Type H1, in the IUPAC classification. A first-order condensation transition follows the growth of a metastable adsorbed layer, and the first-order evaporation transition suggests that the desorption mechanism is one of cavitation. From the local PNF distribution plot, we identified three distinct regions: the dense adsorbed layer where the PNF is less than unity (I), the fluctuation region where the PNF is greater than unity (II), and the gas-like core where the PNF is close to unity.

On the adsorption branch of the isotherm, adsorption proceeds by molecular layering on the pore walls as pressure is increased from an empty pore (points A, B and C in Figure 5.2), and the volume of the adsorbed phase increases up to the condensation pressure when the pore is filled with condensate. From this plot, at temperatures below the critical hysteresis temperature, the boundary of the adsorbed layer increases with pressure, and the fluctuation zone has an undulating interface. Figure 5.3 shows a snapshot of adsorbed molecules at a pressure just before condensation in a 5nm diameter cylinder and 6nm diameter sphere and demonstrates the existence of an undulating interfaces in cylinders and spheres.

Along the adsorption path, as previously found for the open-ended slit pore, the size of the gas-like core or core size diameter in cylindrical and spherical

pores can be determined from the thickness of the adsorbed layer and that of the fluctuation region as

$$D_{core} \ = \ D - \left(d_A + d_F \right) \tag{4.2}$$

This can be used to defined the condensation criterion at the point just prior to condensation as

$$\left[D_{core} \ = \ D - \left(d_A + d_F \right) \right]_{P_{cond}} = D_{core} \big|_{P_{cond}} \tag{4.3}$$

where P_{cond} is the condensation pressure.

5.4.2   Effects of pore size

Figure 5.4 shows the effects of pore size on the argon adsorption isotherms at 87 K in cylindrical and spherical pores and the distributions of local PNF just before condensation. From this figure, we can draw a number of interesting observations:

1. When the pore size is increased, condensation occurs at higher pressure because a higher pressure is required before the thickness of the adsorbed layer is sufficient to leave a gas-like core small enough to induce condensation. It is also noted that the core size just before condensation is larger for a larger pore size, as expected because the condensation pressure is higher for a larger pore. This conforms to the DBdB theory that the radius of curvature of the

interface just before condensation increases at higher condensation pressure.

2. The fluctuation region and the amplitude of the fluctuation just before condensation are larger as the pore size is increased. This is due to the strong curvature of the interface and the influence of the solid-fluid potential in smaller pores. Thus, in large pores molecules enter or leave the adsorbed phase more frequently.

3. For a given pore size, the core size in a sphere just before condensation is greater than in a cylinder, which is in turn greater than in a slit pore because condensation occurs at lower pressure at a high curvature interface. This will be detailed later.

We see that for a given pore size the thickness of the adsorbed layer and that of the fluctuation region are deciding factors in the condensation and that of the radius of curvature of the interface is related to this thickness and to that of the fluctuation region. Figure 5.5 shows the variation of thickness of these zones at the point just before the condensation as a function of pore size. The thickness of the adsorbed layer increases with pore size until the core reaches the critical size for condensation. What is quite intriguing is that the thickness of the fluctuation region also increases with pore size. This can be attributed to the effects of both the curvature of the interface and the influence of the solid-fluid potential. In small pores the solid-fluid potential well is deeper due to overlap of potential fields from the surrounding atoms, which tends to dampen the fluctuations, and also the curvature is greater. In the larger pores the interfacial curvature is less, and potential overlap effects are diminished.
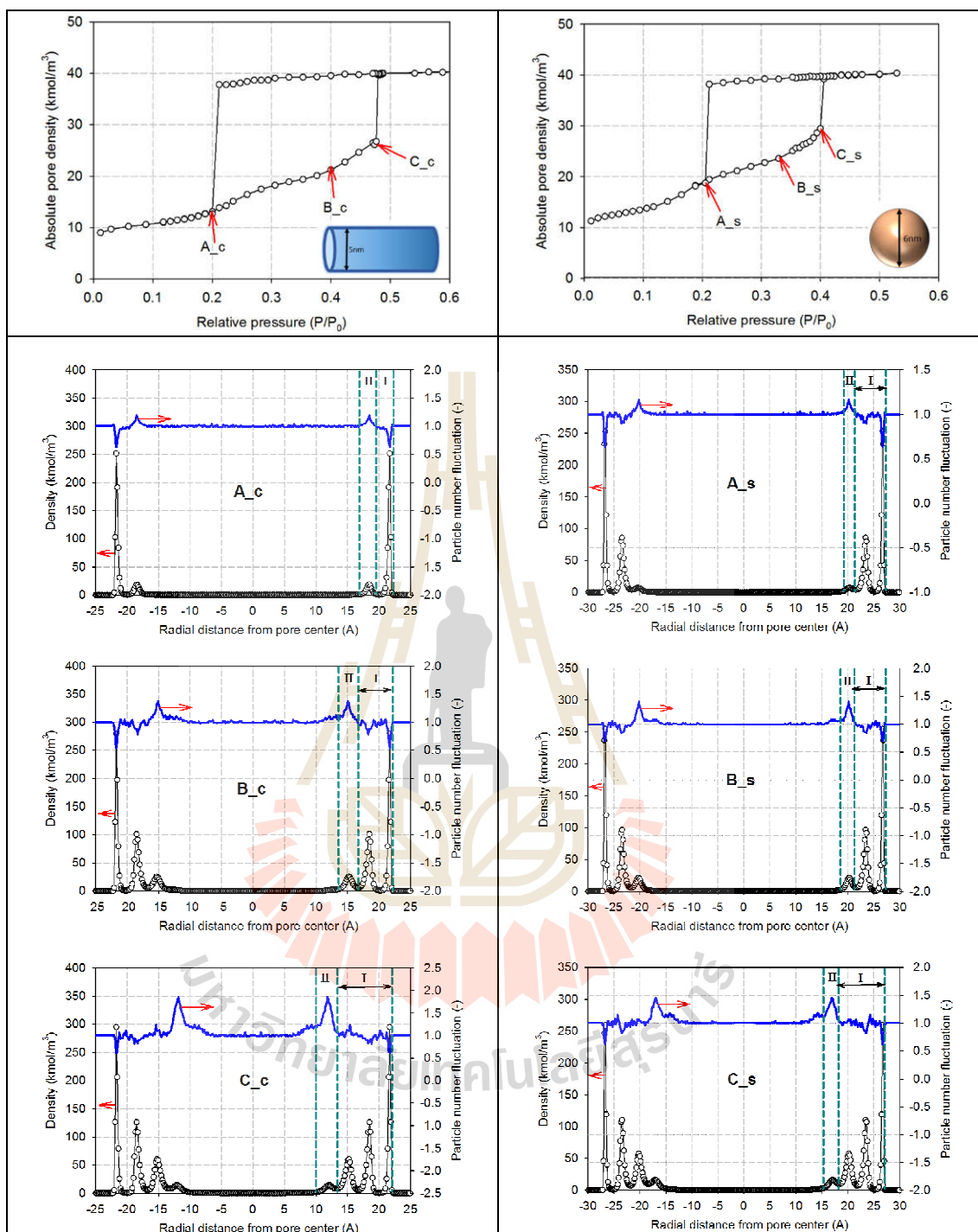
Figure 5.2 Argon adsorption isotherms in cylindrical (left panel) and spherical (right panel) pores having sizes of 5 and 6 nm in diameter at 87 K (top) and their local density distribution and particle number fluctuation (bottom).
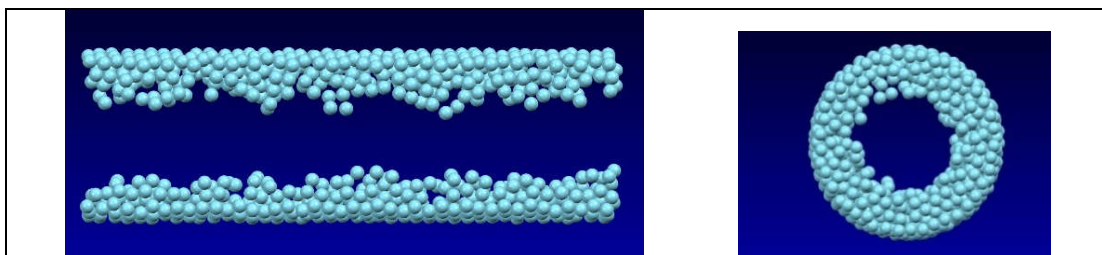
Figure 5.3   Snapshots of argon molecules in cylindrical and spherical pores of 5 and 6 nm in diameter at 87 K at the pressure just before condensation.

As seen in Figure 5.5, the size of the gas-like core and the radius of curvature just before condensation increase with pore size, in contrast to the constant core size observed in slit pores (Nguyen et al., 2011). Our finding here is consistent with the DBdB equation, which accounts for the thickness of the adsorbed layer, since for larger pores a higher condensation pressure is required to build an adsorbed phase thick enough for condensation to occur and DBdB states that the radius of curvature of the interface is greater at higher pressure.

To further understand the nature of adsorbed layer just prior to condensation in cylinders and spheres, we plotted the thickness of the adsorbed layer and the reduced condensation pressure versus pore size in Figure 5.6. For a given pore size, we see that the thickness of the adsorbed layer in spheres is lower than that in cylinders, while the condensation occurs at lower pressure. This suggests that condensation in spheres required fewer adsorbed layers than in cylinders because the solid-fluid potential is greater in spheres and therefore induces condensation sooner.
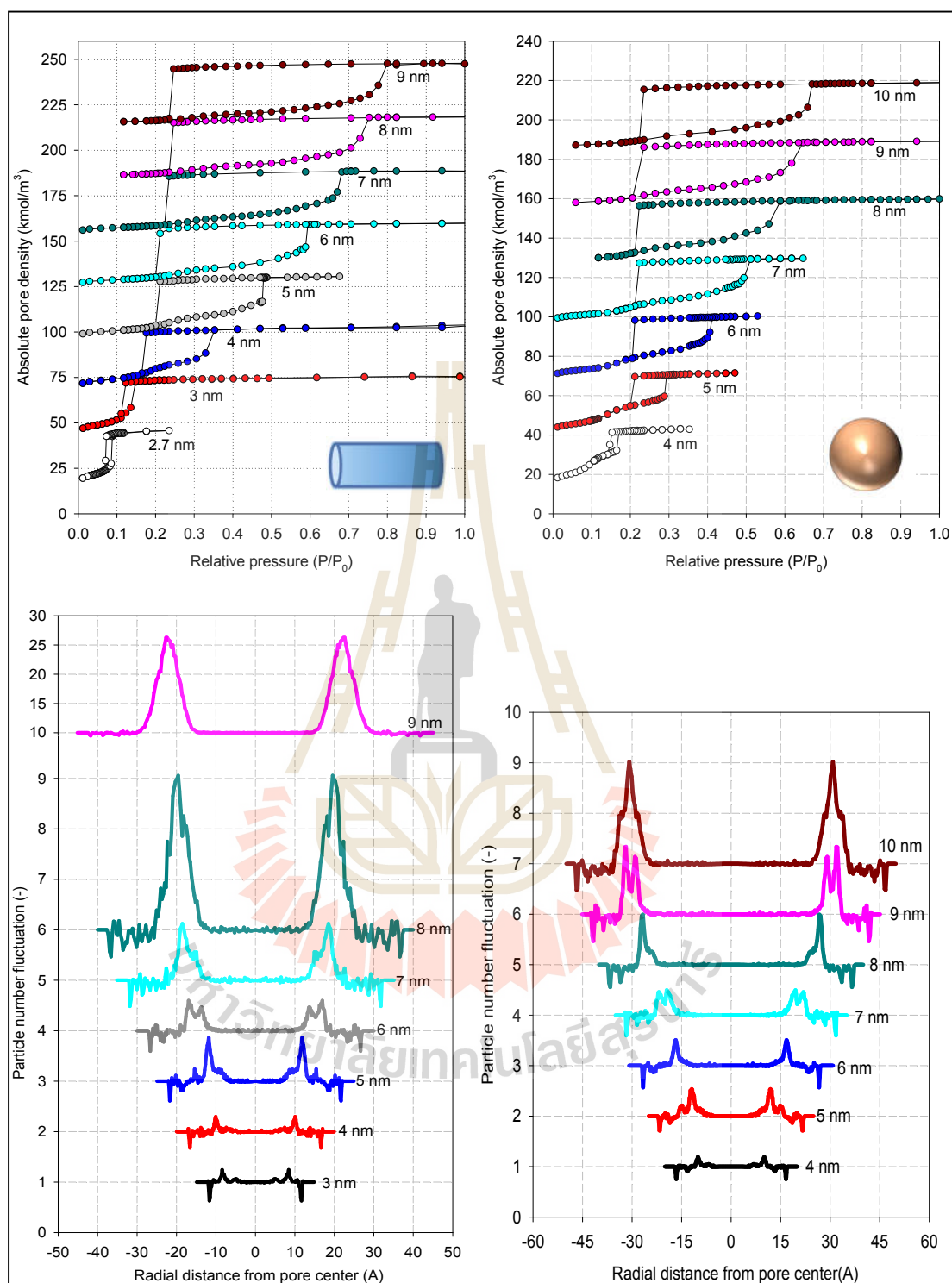
Figure 5.4 Argon adsorption isotherms at 87 K (top) and local particle number fluctuations just before condensation (bottom) in cylindrical (left panel) and spherical (right panel) pores having various pore diameters.
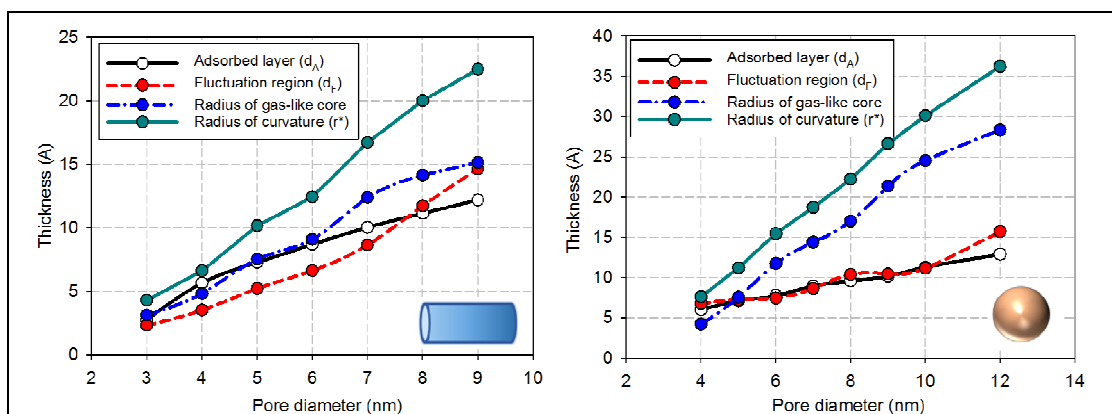
Figure 5.5   Plots of d_A, d_F, radius of gas-like core, and radius of curvature of argon adsorption at 87 K in cylinders (left panel) and spheres (right panel) at the pressure just before condensation.
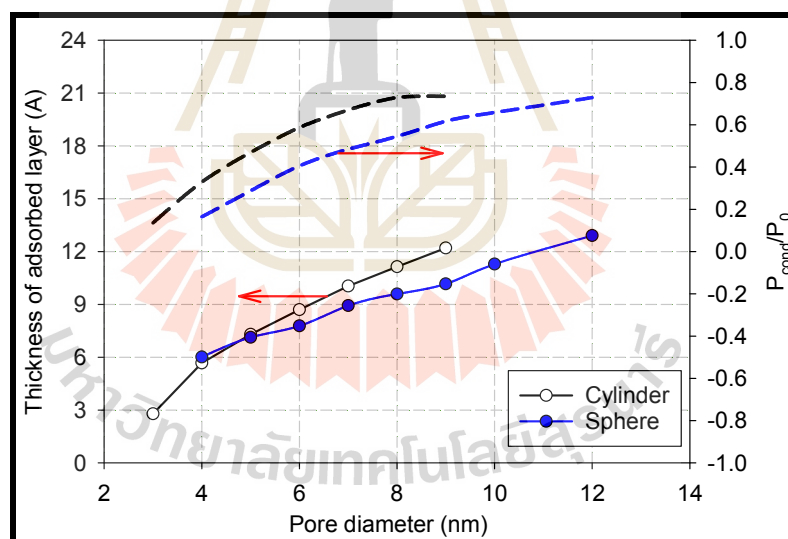
Figure 5.6   Thickness of adsorbed layer and relative pressure for argon adsorption at 87 K in cylinders and spheres at the pressure just before condensation.
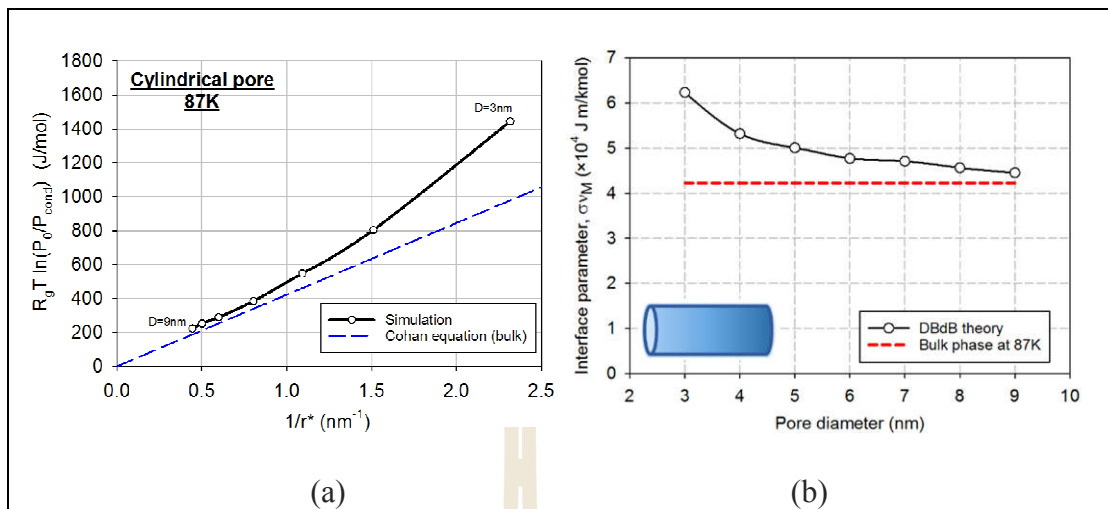
Figure 5.7   (a) Comparison of simulation results determined by undulation theory and the Cohan equation for argon adsorption at 87 K in cylinders having pore sizes of 3-9 nm at the pressure just before condensation. (b) Interfacial parameter obtained from simulation results compared to the bulk value at 87 K.

5.4.2.1   Analysis of the Cohan equation for condensation in cylindrical pores

Having determined the radius of curvature of the interface from the center of the pore to the midpoint of the fluctuation zone and the pressure at condensation from the simulation, we can now test the applicability of the DBdB equation. In Figure 5.7a, we plot $R_gT\ ln(P_0/P_{cond})$ versus the inverse of the radius of the curvature; the dashed line is the classical Cohan equation with the surface tension and molar volume of the bulk liquid. Applying the DBdB equation, we derived the interfacial energy parameter, α, and plotted it as a function of pore diameter in Figure 5.7b. For the range of pore sizes considered, the interfacial energy parameter

calculated from the DBdB equation is greater than its value for the bulk liquid. This is in agreement with earlier reports in the literature (Wongkoblap et al., 2011).

5.4.2.2 Analysis of the Kelvin equation for condensation in spherical pores

In Figure 5.8a we plot $R_g T \, ln(P_0/P_{cond})$ versus the inverse of the radius of the curvature for adsorption in spheres. The interfacial energy parameter, calculated from the DBdB equation are presented in Figure 5.8b as a function of pore size, now shows the opposite trend to cylinders and decreases with pore diameter for pores less than 6 nm but is, nevertheless, higher than the bulk liquid value. This can be attributed to the inefficient packing of molecules in a spherical confinement. As the pore diameter increases, efficient packing becomes more facile, and the cohesiveness of the interface due to the effect of the solid-fluid interaction becomes more dominant, resulting in an interfacial energy parameter that is greater than the bulk value. In even larger pores, the packing effect and the effect of the external adsorbent field both diminish, and the energy tends to the bulk value. The prove of packing efficiency is presented in Figure 5.9 the local density distribution for a 5 nm diameter spherical pore just before condensation and compare this with equivalent distribution for a graphitic surface and a cylindrical pore.

(a)   (b)
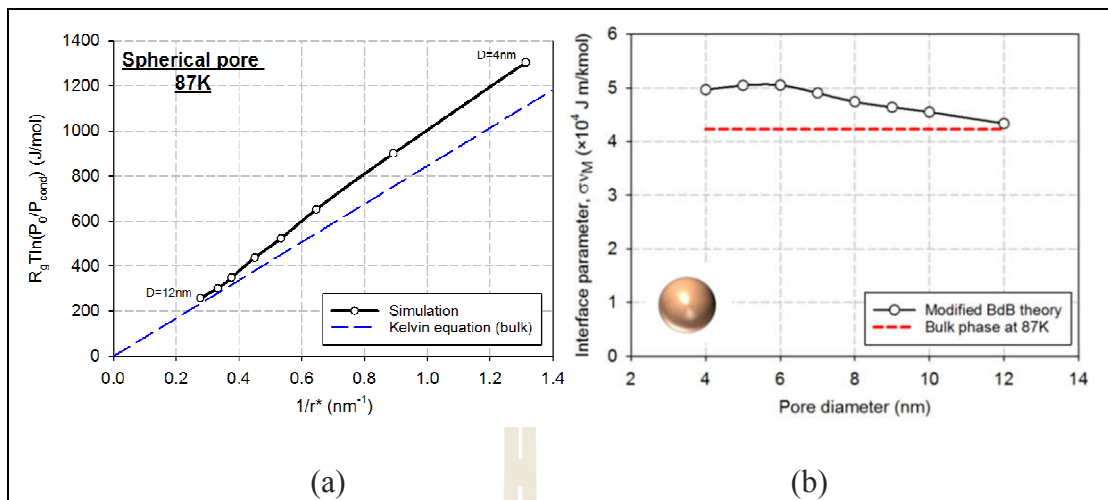
Figure 5.8   (a) Comparison of simulation results determined by undulation theory

and the Kelvin equation for argon adsorption at 87 K in cylinders

having pore sizes of 4-12 nm at the pressure just before condensation.

(b) Interfacial parameter obtained from simulation results compared to

the bulk value at 87 K.

5.4.2.3   Effect of solid-fluid potential on derived interfacial parameters at 87 K

The interfacial energy parameter, characterizing the

cohesiveness of molecules at the interface, is affected strongly by the solid-fluid

potential. In Figure 5.10, we plot α as a function of the solid-fluid potential energy at

the interface (r^*) for cylinders and spheres. The graphs show that in addition to the

role played by packing effects in small spheres the solid-fluid potential directly affects

the cohesiveness of molecules at the interface separating the adsorbed phase and the

gas phase.
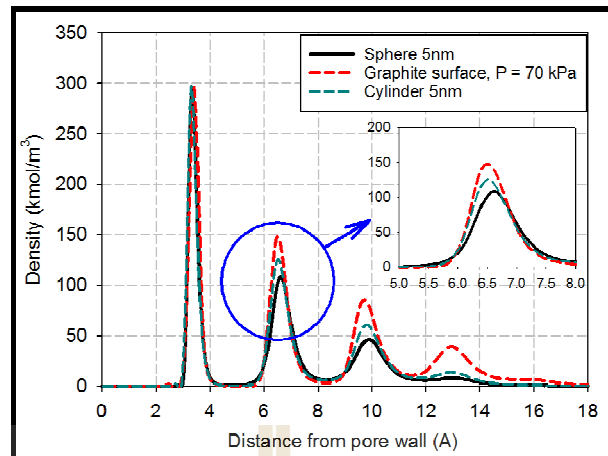
Figure 5.9   Comparison of local density distribution of argon between a spherical pore of 5 nm, a cylindrical pore of 5 nm, and on a flat surface at 87 K at the points just before condensation.
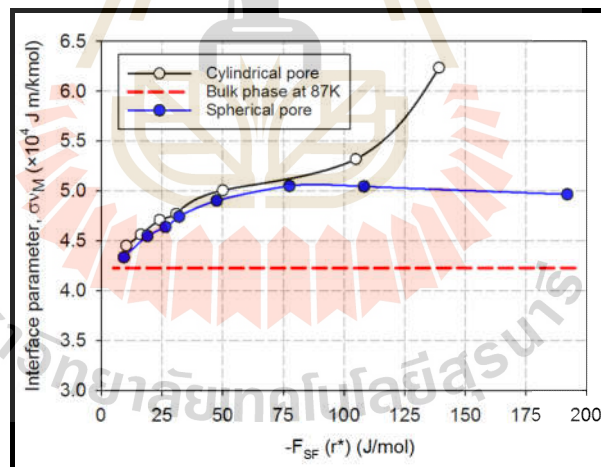
Figure 5.10   Gas-liquid interface parameter for argon adsorption at 87 K in cylindrical and spherical pores and for bulk phase argon, as a function of solid-fluid interaction at the radius of curvature for a liquid-like meniscus.
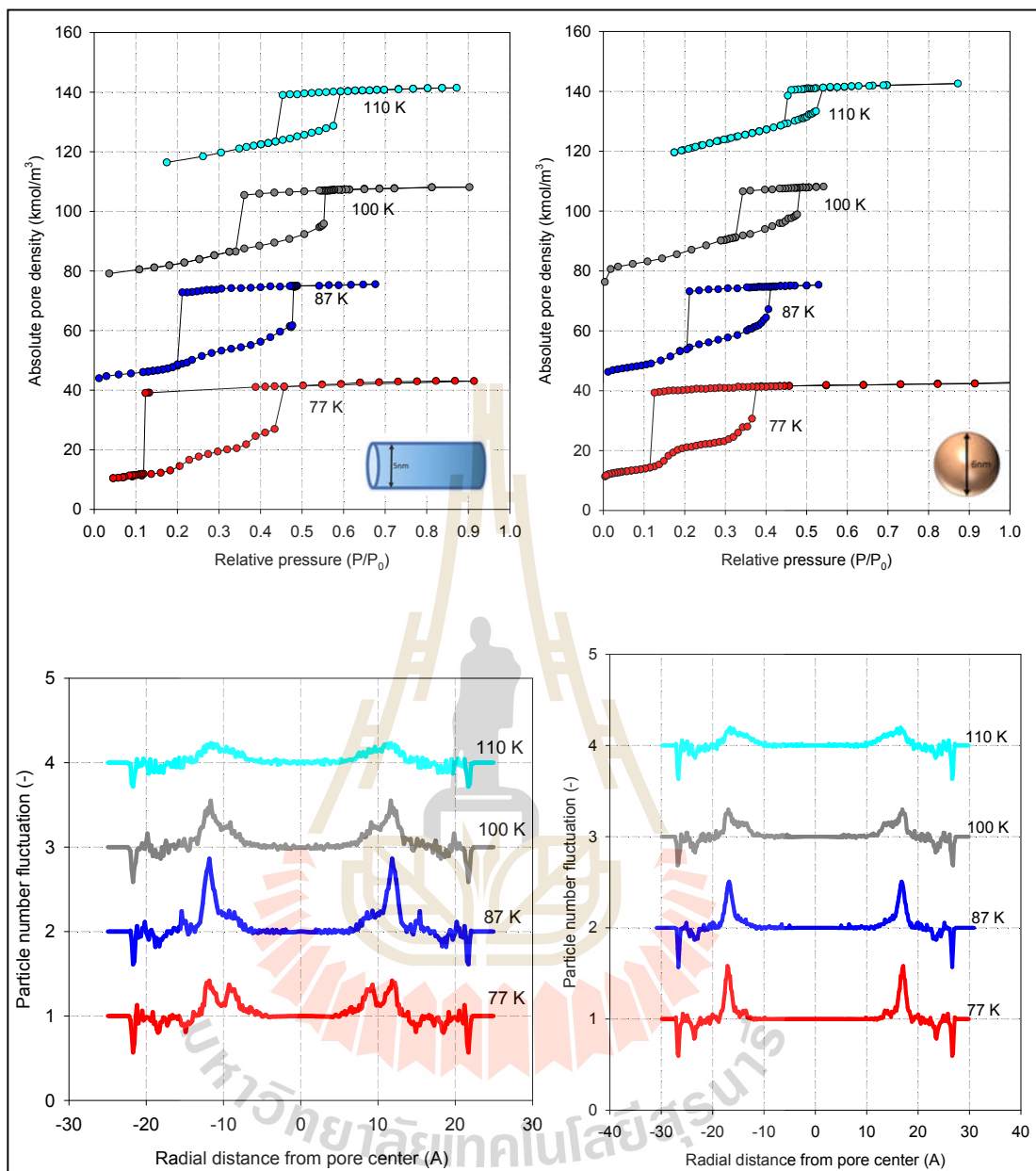
Figure 5.11   Argon adsorption isotherm (top) and local particle number fluctuation (bottom) at a pressure just before condensation in a cylinder of 5 nm in diameter (left panel) and a sphere of 6 nm in diameter (right panel) from 77 to 110 K.

5.4.3 Effects of temperature

Figure 5.11 shows the temperature dependence of the isotherms and their PNF at the point prior to condensation for argon in cylinders and spheres with pore diameters of 5 and 6 nm. As expected, the pore density and the width of the hysteresis loop decrease due to the increase in thermal fluctuations as temperature is increased. In contrast to an open-ended slit pore, the condensation shifts to higher relative pressures, as also reported experimentally by Morishige et al. (Morishige and Shikimi, 1998; Morishige and Tateishi, 2006) for adsorption in cylindrical pores. This occurs because the curvature of the pore wall dampens the unlation and stabilizes the adsorbed layer. To support this assertion, we plotted the thickness of the adsorbed layer and that of fluctuation just before condensation as a function of temperature as shown in Figure 5.12. For both cylindrical and spherical pores, the width of the fluctuation zone increases, and that of the adsorbed layer and of the gas-like core decreases, with increasing temperature due to the increase in thermal fluctuations at higher temperatures. We also found that the radius of curvature of the interface increases with temperature as predicted by DBdB theory.

We have determined earlier, by extrapolation, that at 87 K the threshold pore diameter for capillary condensation in cylinders is about 10 nm, below which the DBdB theory must be used to account for the fact that the interfacial energy parameter is greater than that of the bulk. This means that the Cohan equation is only applicable for pores having diameters greater than 10 nm. A question that now arises is what is the threshold pore size when the temperature is increased? Figure 5.13 shows the effects of temperature on the plot of $R_g T \, ln(P_0/P_{cond})$ versus the inverse radius of curvature at the relative pressure just prior to condensation for various pore

diameters. We find that the threshold pore size increases with temperature for both kinds of pores.

5.4.4 Effects of strength of the adsorbent field

The effects of different adsorbent field strength on argon adsorption isotherm at 87 K in a cylinder of 5 nm diameter and a sphere of 6 nm diameter are shown in Figure 5.14 with the PNF profiles at a pressure just before the condensation. For weaker adsorbents, condensation is shifted to higher pressure due to the slower growth of the adsorbed layer. It is notable, from the PNF plots, that the size of the fluctuation region and gas-like core both increase as the adsorbent becomes weaker. This is in qualitative agreement with the DBdB theory since a larger core radius is required before condensation can occur when the adsorbent strength is weaker.
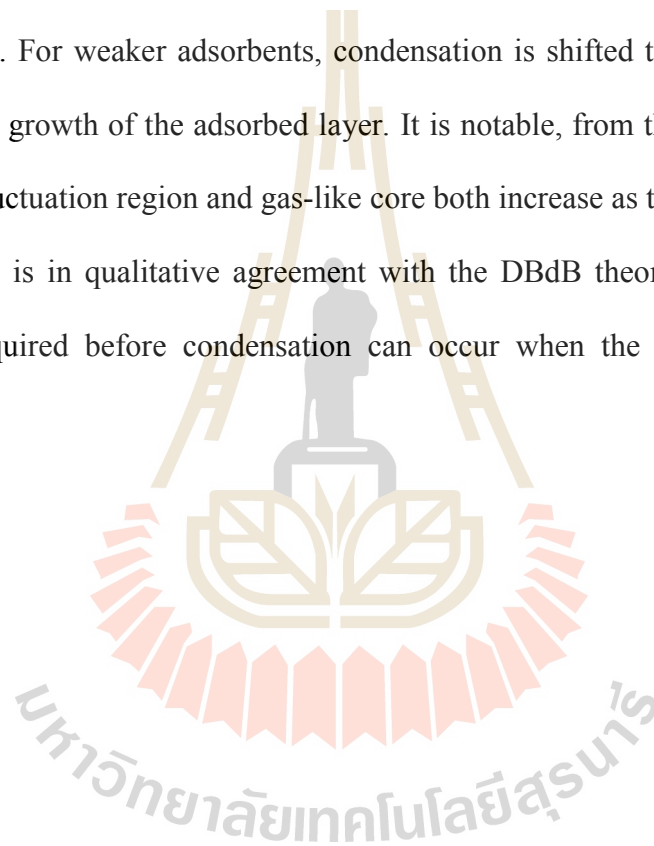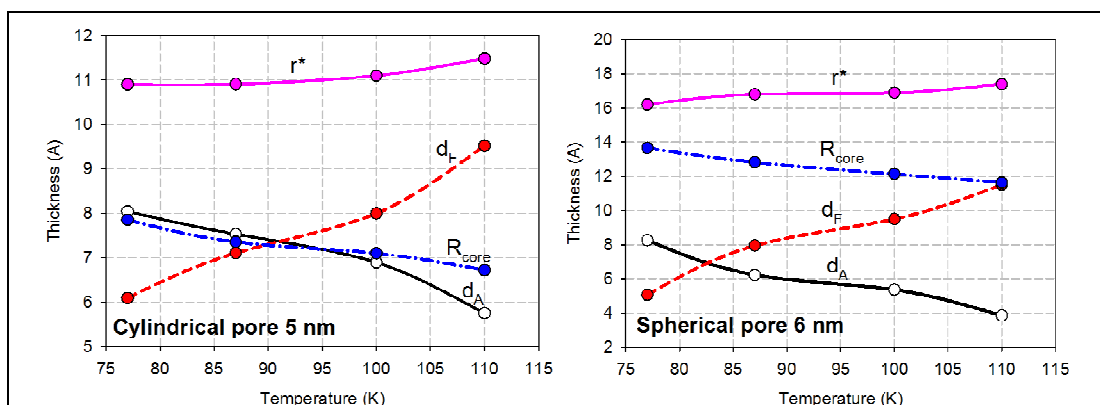
Figure 5.12 Plots of d_A, d_F, radius of gas-like core, and radius of curvature of argon adsorption in a cylinder of 5 nm diameter and a sphere of 6 nm diameter as a function of temperature.
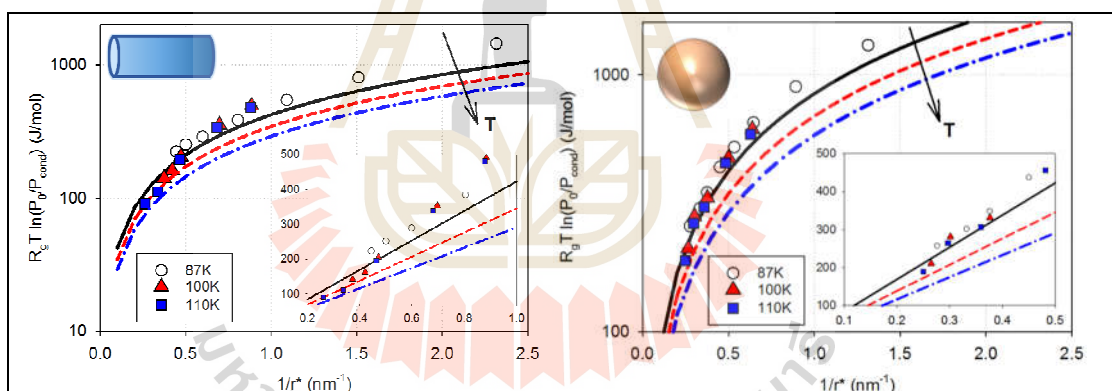
Figure 5.13 $R_g T \ln(P_0/P_{cond})$ for argon adsorption at 87-110 K versus the inverse meniscus radius just before condensation pressure. Simulation results: symbols. Dashed lines: Cohan (cylinders) or Kelvin (spheres) equation using bulk liquid values for the energy parameter. The color schemes are black 87 K, red 100 K, and blue 110 K.
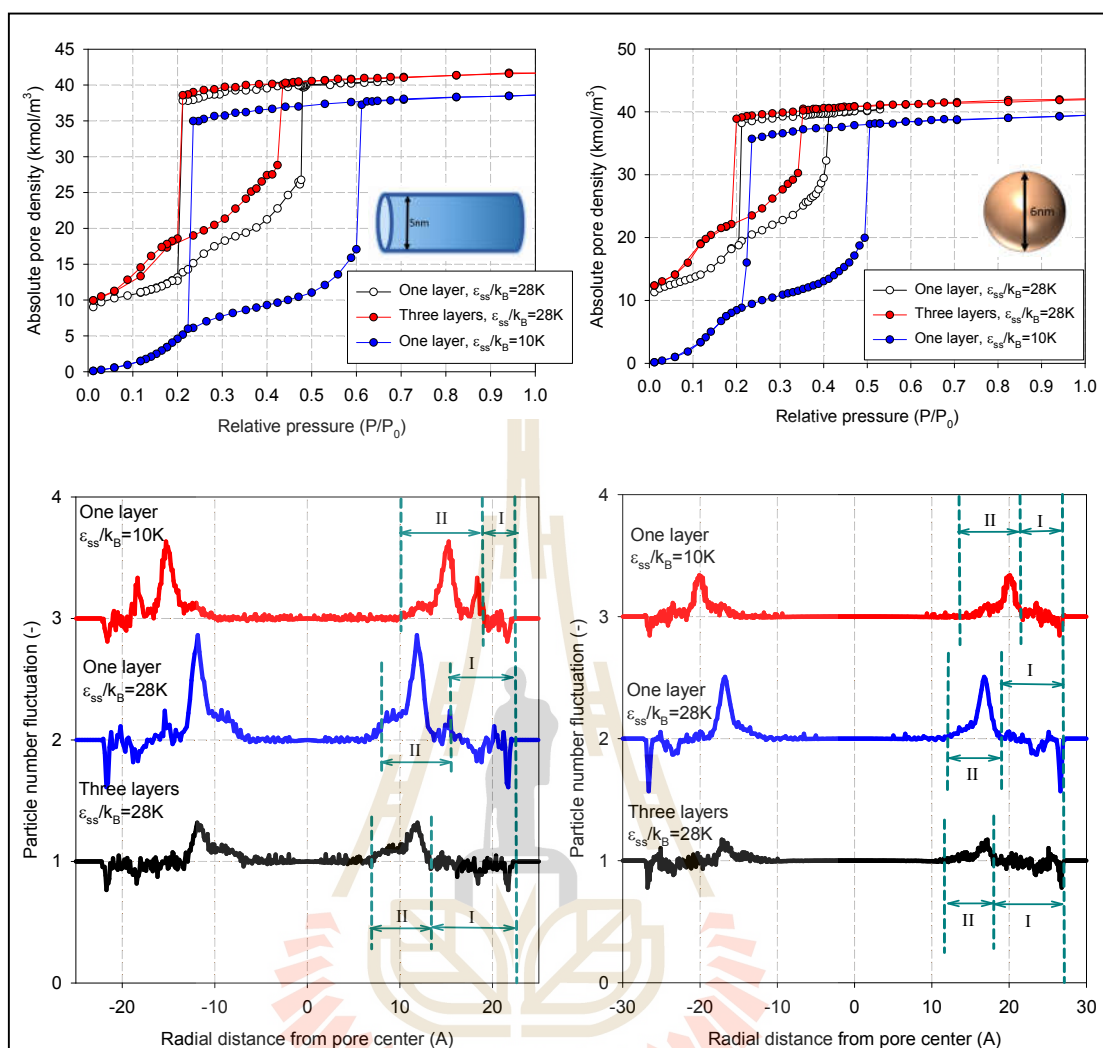
Figure 5.14 Argon adsorption isotherms (top) and PNF just before condensation (bottom) in a cylinder of 5 nm (left) and a sphere of 6 nm at 87 K with different surface strengths. I and II are indicated as dense adsorbate and fluctuation regions, respectively.

5.5   Conclusions

The undulation theory for capillary condensation under subcritical conditions, previously developed for slit pores, has been extended to cylindrical and spherical pores. A microscopic analysis of particle number fluctuation (PNF) has been used to interpret the mechanisms of condensation in these two pore geometries. The effects of pore diameter, temperature, and solid affinity on the wave-like fluctuation at the adsorbate gas-like interface are considered at a pressure just prior to condensation.

The conclusions from this study may be summarized as follows:

1. The width of the fluctuation region increases with increasing pore diameter. In particular, the gas-like core diameter does not remain constant in contrast to our earlier study on slit pores.
2. For a given pore diameter, the size of the fluctuation zone in a cylinder is smaller than in a sphere because of the difference in interfacial curvature.
3. The width of the fluctuation zone increases with increasing temperature or adsorbent field strength, and that of the dense adsorbed phase and the gas-like region decreases.

The interfacial energy parameter, α, which appears as σv_M in the Cohan or Kelvin equations has been evaluated at the relative pressure just prior to condensation. For the range of cylinder and sphere diameters considered, the energy parameter is typically greater than that calculated using bulk phase quantities. In large pores, the fluid properties within the pore converge toward those of the bulk fluid, and the Cohan-Kelvin theories are excellent approximations. An interesting feature, not

previously recognized, is that tight packing in smaller spherical pores results in disorder in the adsorbate and in a decrease in the interface parameter.

5.6   References

Broekhoff, J.C.P. and De Boer, J.H. (1967a). Studies on pore systems in catalysts IX. Calculation of pore distributions from the adsorption branch of nitrogen sorption isotherms in the case of open cylindrical pores. **Journal of Catalysis**. 9: 8-14.

Broekhoff, J.C.P. and De Boer, J.H. (1967b). Studies on pore systems in catalysts X. Calculation of pore distributions from the adsorption branch of nitrogen sorption isotherms in the case of open cylindrical pores. **Journal of Catalysis**. 9: 15-27.

Cohan, L.H. (1938). Sorption hysteresis and the vapor pressure of concave surfaces. **Journal of the American Chemical Society**. 60: 433-435.

Derjaguin, B. (1992). A theory of capillary condensation in the pores of sorbents and of other capillary phenomena taking into account the disjoining action of polymolecular liquid films. **Progress in Surface Science**. 40: 46-61.

Everett, D.H. and Haynes, J.M. (1973a). Capillarity and porous material: Equilibrium properties. **Colloid Science**. 123-172.

Everett, D.H. and Haynes, J.M. (1973b). Model studies of capillary condensation I. Cylindrical pore model with zero contact angle. **Journal of Colloid and Interface Science**. 38: 125-136.

Horikawa, T., Do, D.D. and Nicholson, D. (2011). Capillary condensation of adsorbates in porous materials. **Advances in Colloid and Interface Science**. 169: 40-58.

Kornev, K.G., Shingareva, I.K. and Neimark, A.V. (2002). Capillary condensation as a morphological transition. **Advances in Colloid and Interface Science**. 96: 143-167.

Morishige, K. and Shikimi, M. (1998). Adsorption hysteresis and pore critical temperature in a single cylindrical pore. **Journal of Chemical Physics**. 108: 7821-7824.

Morishige, K. and Tateishi, N. (2006). Accurate relations between pore size and the pressure of capillary condensation and the evaporation of nitrogen in cylindrical pores. **Langmuir**. 22: 4165-4169.

Nguyen, P.T.M., Do, D.D. and Nicholson, D. (2011). On the hysteresis loop of argon adsorption in cylindrical pores. **The Journal of Physical Chemistry C**. 115: 4706-4720.

Phadungbut, P., Fan, C., Do, D.D., Nicholson, D. and Tangsathitkulchai, C. (2015). Determination of absolute adsorption for argon on flat surfaces under sub- and supercritical conditions. **Colloids and Surfaces A: Physicochemical and Engineering Aspects**. 480: 19-27.

Rouquerol, F., Rouquerol, J. and Sing, K. (1999). **Adsorption by powders and porous solids**. Academic Press: London.

Thommes, M. (2004). Physical adsorption characterization of ordered and amorphous mesoporous materials. In: Lu, G., Zhao, X.S. (Eds.). **Nanoporous Materials**. Science & Engineering. Imperial College Press. New Jersey: 317-364.

Trokhymchuk, A. and Alejandre, J. (1999). Computer simulations of liquid/vapor interface in Lennard-Jones fluids: Some questions and answers. **Journal of Chemical Physics**. 111: 8510-8523.

Ustinov, E.A., Do, D.D. and Jaroniec, M. (2005). Equilibrium adsorption in cylindrical mesopores: A modified Broekhoff and de Boer theory versus density functional theory. **The Journal of Physical Chemistry B**. 109: 1947-1958.

Wongkoblap, A., Do, D.D., Birkett, G. and Nicholson, D. (2011). A critical assessment of capillary condensation and evaporation equations: A computer simulation study. **Journal of Colloid and Interface Science**. 356: 672-680.
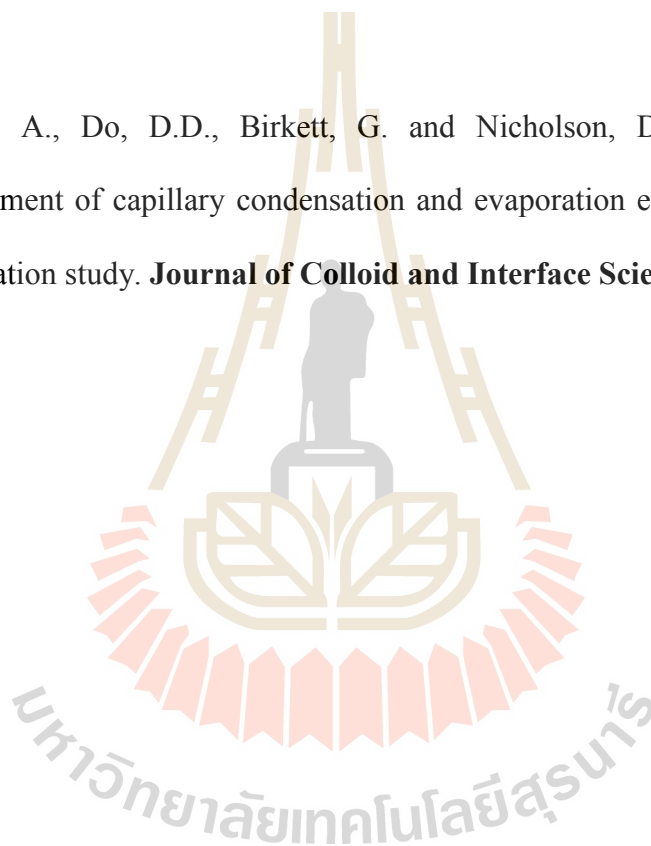
CHAPTER VI

THE MICROSCOPIC ORIGIN OF HYSTERESIS LOOP IN SLIT PORES

6.1 Abstract

The compelling evidence for adsorbate restructuring as the microscopic origin of hysteresis loop in closed end pores is here presented. The argument is based on the molecular simulations in the grand canonical (GCE) and meso-canonical (MCE) ensembles, for argon adsorbed at 87 K in slit mesopores of different topologies. The MCE isotherms have sigmoidal van der Waals type loops, while the GCE isotherms exhibit hysteresis loops, which are confined between the gas-like and liquid-like spinodal points. One interesting feature, not previously recognized, is that the condensation in the MCE isotherms for pores of different topologies is identical, and it occurs at the same chemical potential, which is the coexistence chemical potential of two phases in equilibrium: the liquid-like condensate and the gas-like phase. As the menisci approach the pore mouth, the liquid condensate is progressively restructured to become more cohesive. When the pressure is reduced in the grand canonical ensemble, a lower pressure is required to disrupt this cohesive structure, resulting in hysteresis in the closed end pores. The classical theories, which conclude that isotherms for closed end pores must be reversible, are in error because they assume that the interfacial energy parameter has the same value as in a bulk liquid.

6.2   Introduction

Adsorption of simple gases in mesoporous materials has been extensively studied because of its importance for the characterization of porous materials in conjunction with a suitable pore model (Neimark et al., 2000). Experimental isotherms for materials with pores in the mesopore size range exhibit hysteresis at temperatures below the critical hysteresis temperature (T_{ch}). For a given adsorbate, the properties of the hysteresis loop: shape, size and position, are a function of temperature, pore material and geometry. Thus for a given adsorbate, temperature, and an assumed pore model, experimental isotherms can be used in an inversion procedure to determine pore size distribution of the given solid. The question of whether the adsorption or desorption branch of the isotherm should be used for characterization is often raised. To this end, the shape of the hysteresis loop can provide some useful clues. Four distinct forms of hysteresis loop, H1-H4, and mechanisms for their formation have been proposed by the IUPAC.

The existence of hysteresis can be attributed to different metastable states in the adsorption along the adsorption branch and the condensate along the desorption branch (Neimark and Vishnyakov, 2000). Simulation studies of hysteresis are commonly carried out in one or both of two ensembles: grand canonical (GCE) and meso-canonical (MCE) ensembles. For the MCE study, Puibasset et al. (2009) and Nguyen et al. (2011) have carried out simulations to study the effects of the size of the gas reservoir, the dimension and shape of the pore walls and the dosing increment on argon adsorption in pores of infinite length at temperatures below the pore critical hysteresis temperature. They observed classical sigmoid vdW loops with a vertical segment in the middle of the loop, indicating the coexistence of the rarefied and dense

phases within the pore. However, for a pore of finite length open at both ends, the MCE isotherm exhibits an S-shape, which is closer to the desorption branch of the corresponding GCE isotherm (Nguyen et al., 2014; Fan et al., 2014a), indicating that the adsorbed fluid is closer to equilibrium along the desorption branch.

The existence of a hysteresis loop for closed end pores has been controversial topic. The classical thermodynamics originated by Cohan and Kevin (Cohan, 1938) implies that the isotherm would be reversible assuming that the adsorbate behaves like a bulk liquid and is not modified by the external adsorbent field. The recent communications (Nguyen et al., 2013; Zeng et al., 2014) have suggested that hysteresis can occur in uniform closed end pores, and the following conclusions are derived from the mesoscopic analysis:

1. The radius of curvature of the meniscus becomes smaller as the adsorbed layer grows thicker during adsorption; but it remains constant during desorption.
2. The condensate becomes denser and more cohesive as loading is increased, and consequently the desorption transition occurs at a lower pressure than the adsorption transition.

In this chapter, we have simulated MCE isotherms in pores open at both, closed at one end, or closed at both ends and searched for common features in the coexistence of two phases within the pores. We find that the adsorbate density distribution along the axial direction of a pore, at the same loading, is different in adsorption and desorption, and that an enhancement in the density, and consequent

restructuring of the adsorbate, which occurs when the pore is nearly filled, is the microscopic origin of the existence of hysteresis in a closed end pore.

6.3   Simulation

The simulations were performed with argon and its molecular interaction was given by the 12-6 Lennard-Jones equation. The three slit pore models studied are shown in Figure 6.1. The box length in the y-direction was kept constant at 10 times the collision diameter of argon. The planar walls were constructed from three homogeneous graphene layers. Periodic boundary conditions were applied at the y-boundaries, and the solid-fluid potential of the finite planes in the x-direction was modeled by the Bojan-Steele equation.

In the GCMC simulation, we used 80,000 cycles in the equilibration and sampling stages, except for pores with closed ends for which we used 300,000 cycles. Each cycle consisted of 1,000 attempted displacements, insertions or deletions with equal probability.

For the MCE simulation, we used 50,000 cycles in both the equilibration and sampling stages, and each cycle consisted of 1,000 attempted displacements or exchanges between boxes chosen randomly with equal probability. We have found that a cubic dosing reservoir with a linear dimension of 7 nm was suitable to trace the MCE isothers for all the pore models in Figure 6.1, following the concept of mass transfer lines (Phadungbut et al., 2014).
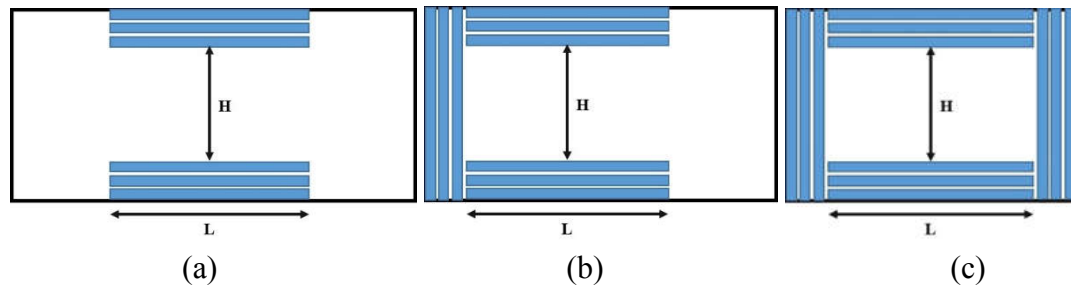
Figure 6.1   Schematic diagrams of the three slit-like graphitic pore models: (a) open end pore; (b) closed end pore; (c) closed pore.

6.4   Results and Discussion

6.4.1   Adsorption in slit pores of different topologies

The MCE (closed system) and GCE (open system) isotherms of argon in slit pores of 3 nm width and 20 nm length at 87 K with different topologies are shown in Figure 6.2-6.5. We denote the open end, closed end and closed pores as *O*-pore, *C*-pore and *CC*-pore, respectively.

6.4.1.1 Adsorption in the open end pore (*O*-pore)

The GCE isotherm of *O*-pore shows first order transitions for both condensation and evaporation. Condensation occurs in slits when the undulating interfaces of the two adsorbed layers on the two opposite walls meet the form a large bridge of adsorbate (Fan et. al., 2014b). On desorption, the menisci from opposite ends of the pore recede, and the isotherm forms a knee along the desorption branch prior to the evaporation.

Figure 6.2   (a) The GCE and MCE isotherms and 2D-density profiles at various points along the MCE isotherm for argon adsorption at 87 K in a finite open end slit pore of 3 nm width and 20 nm length. (b) Local density distribution along pore length at the points just before (Point A1) and after (Point B1) liquid bridge formation.

On the other hand, the MCE isotherm follows a sigmoid path: it first traces the adsorption branch of the GCE isotherm as molecular layers build up on the pore walls, but passes the GCE condensation pressure to reach a gas-lik spinodal point (A1). Here the density distribution is uniform, except at the ends of the pore where the solid-fluid interaction are weaker. There is then a sharp decrease in pressure to B1 where a thin biconcave liquid bridge forms as shown in the inset of Figure 6.2a and the density plots in Figure 6.2b. The supply of molecules to build this liquid bridge comes from two sources:

1. The dosing reservoir; resulting in a sharp decrease in the pressure from Point A1 to B1 (Figure 6.2a)

2. The adsorbate layers; which become thinner and are in equilibrium with the liquid bridge (Figure 6.2b). Prior to this mass transfer the adsorbate layer is meta-stable, and is stabilized by the transfer.
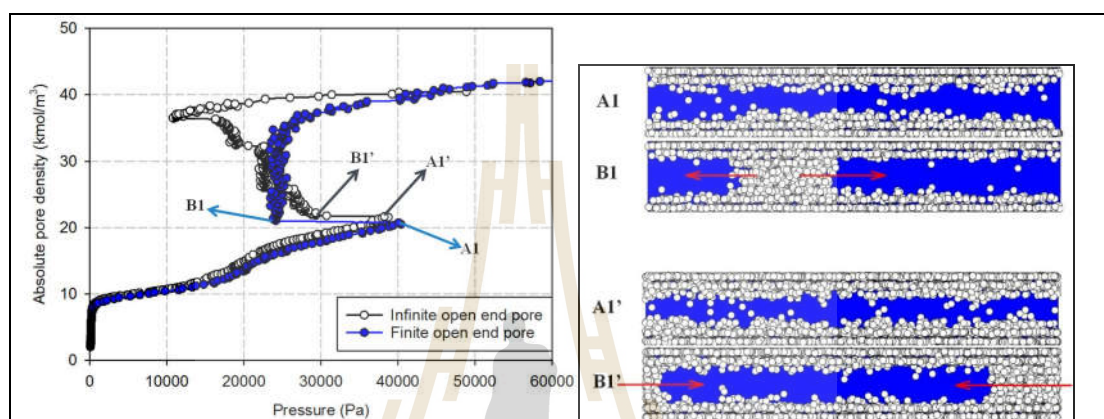
Figure 6.3   MCE isotherms and snapshots for infinite and finite open end pores of 3 nm pore width. The arrows show the direction of menisci movement.

The MCE adsorption then follows a path close to the desorption branch of the GCE isotherm. The magnitude of the sharp pressure decrease from A1 to B1, with the accompanying re-distribution of molecules, is a measure of the hysteresis, and could be regarded as its microscopic orgin. In pores with both ends open, this corresponds to the two different curvatures of the interfaces separating the condensed and gas phases (zero curvature at A1 to a cylindrical curvature at B1). While Point A1 is the gas-like spinodal point, Point B1 is not the liquid-like spinodal point because this would take the form of a liquid condensate containing dispersed bubbles. Instead, the adsorbate at B1 consists of a condensed phase in the form of a

liquid bridge in thermodynamic equilibrium with a gas phase. It is important to note that this is a thermodynamic equilibrium in a finite system (Hill, 1994), which differs from that in an infinite system where there is a first-order transition between the two states.

We demonstrate in Figure 6.3 where we have plotted the MCE isotherms for two slit pores with both ends open: one is finite in length and the other infinite (modeled with periodic boundary conditions). When the gas-like spinodal point is reached in both pores, the pressure is decreased and two phases co-exist. The difference between these pores lies in fact that the gas-like phase in the finite pore is in contact with the gas surroundings, while in the infinite pore, the liquid bridge is dispersed within the gas-like phase. As the number of molecules increases the gas-like phase becomes a dispersed phase in the liquid-like condensate and reaches a liquid-like spinodal point where the gas-like bubbles are small and disappear as further molecules are added to the system.

The transition between the two phases is first order in an infinite pore, but not in a finite pore. This is explained as follows: after the pressure decreases sharply from A1 to B1 (Figure 6.2a) with the formation of a thin biconcave liquid bridge, further addition of molecules results in an expansion of the liquid bridge along the pore axis as its two interfaces advance toward the pore mouths. As they approach the pore mouths, the solid-fluid interaction is weaker and therefore a higher chemical potential is required to sustain the thermodynamic equilibrium between the two phases. The MCE isotherm for the finite pore with both ends open therefore shows a second order transition.

Although the MCE isotherm beyong B1 is close to the desorption branch of the GCE isotherm, they do not coincide, indicating that the structures of the fluid in the MCE and GCE ensembles are different.

6.4.1.2 Adsorption in the closed end pore (*C*-pore)

The GCE isotherm for the *C*-pore (Figure 6.4) exhibits a much smaller hysteresis loop that the corresponding *O*-pore. It is important to note that much longer cycles were used in the simulation of the *C*-pore to ensure the reproducibility of its hysteresis loop. As adsorption progresses from an empty *C*-pore, adsorbed layers build up on the pore walls as well at the closed end, with a thicker layer at the closed end, because of the overlap from adjacent adsorbent planes gives a stronger solid-fluid interaction. This results in the formation of a meniscus which advances to the pore mouth over a small change of pressure as shown in the steep (but not vertical) increase in the density of the GCE isotherm. Once the meniscus has reached the open end, the density gradually increases as the meniscus changes from cylindrical to flat and fills the region at the pore mouth.

On desorption from a completely filled pore, the meniscus recedes from the pore mouth into the pore interior. The meniscus shape changes from flat to cylindrical, and the thickness of the adsorbed layers in the gas-like region becomes essentially constant. When the radius of curvature of the meniscus has reached its minimum (Zeng et al., 2014) there is a steep (but not vertical) evaporation.

The MCE isotherm, unlike the corresponding GCE isotherm, osciallates strongly but falls within the hysteresis loop of the GCE isotherm. This could be regarded a sign of the existence of a hysteresis, which is supported by the microscopic analysis in Section 6.4.2.
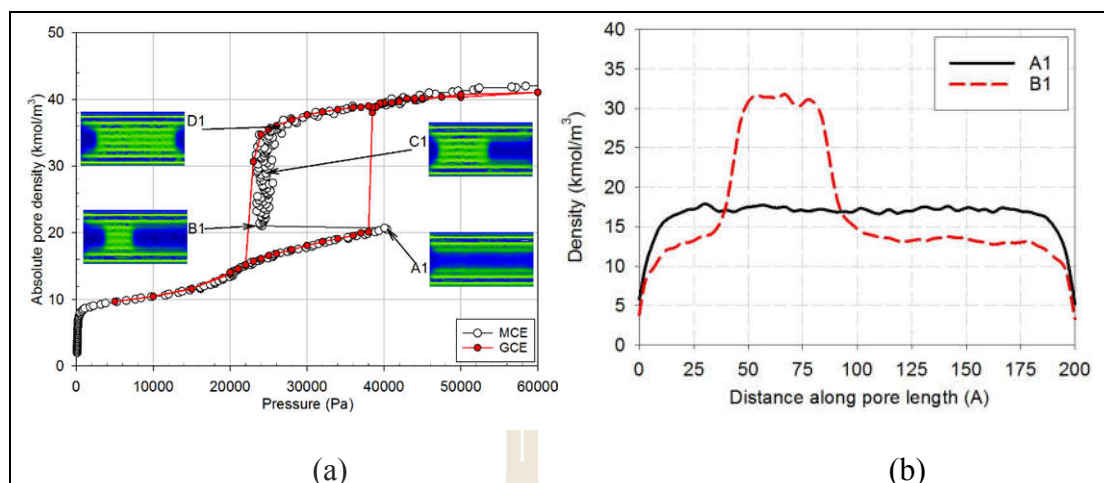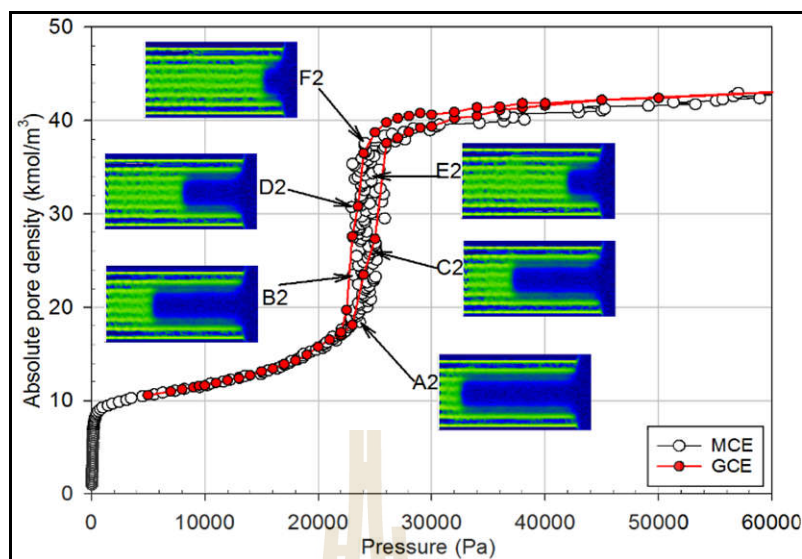
Figure 6.4 GCE and MCE isotherms and 2D-density profiles at various points along the MCE isotherm for argon adsorption at 87 K in a closed end slit pore of 3 nm width and 20 nm length.

6.4.1.3 Adsorption in the closed pore (*CC*-pore)

The hysteresis loop of the GCE isotherm for the CC-pore, shown in Figure 6.5, is of Type H2, which is a classic case of cavitation in a completely filled pore. The same cavitation also occurs in an infinitely long pore with both ends open to the gas surroundings. It should also be stressed that the cavitation pressure is affected by the solid-fluid interaction, and approaches bulk fluid properties asymptotically for large pores.

The MCE isotherm shows a gradual transition to the gas-like spinodal point B3 (in constrast to the steep transition to the corresponding point for the *O*-pore), a steep transition at the liquid-like spinodal point D3 and an even steep transition at the solid-like spinodal point F3. This is in accord with the appearance of

a spherical bubble according to the classical nucleation theory (Frenkel, 1946; Debenedetti, 1996) and first-order phase transition theory (Binder, 1987; Bravina and Zabrodin, 1995). Adsorption starts with molecular layering on the pore walls up to Point A3, followed by the formation of two menisci at the closed ends, which advance toward the center of the pore, as the bubble changes its shape from ellipsoidal to cylindrical at B3. When further molecules are added, the cylindrical bubble shrinks in size and finally disappears at D3 (the liquid-like spinodal point). The path E3-F3 represents the transition from a liquid-like adsorbate to a solid-like adsorbate (inset in Figure 6.5).
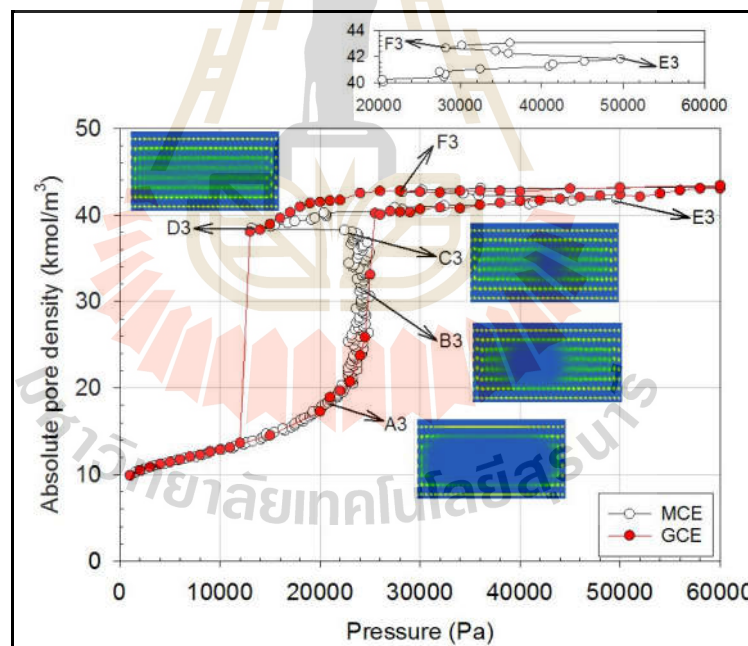
Figure 6.5 GCE and MCE isotherms and 2D-density profiles at various points along the MCE isotherm for argon adsorption at 87 K in a closed slit pore of 3 nm width and 20 nm length.

6.4.1.4 Comparison between MCE isotherms for pores of different topologies

Figure 6.6 shows the three MCE isotherms for pores of different topologies, where we note a distinctive feature about the overlap of the very steep segments of these isotherms. This steep segment corresponds to the thermodynamic equilibrium between the two phases, suggesting that when two phases are in equilibrium the thermodynamic properties (for example, the coexistent chemical potentials) are affected by the pore ends, whether they are open or not. This conclusion remains true for pores of different dimensions.

To substantiate our assertions, we illustrated in Figure 6.7 the local densities of the O- and C-pores and the corresponding snapshots as a function of the distance along the pore axis, at various points on the MCE isotherms.

We see that the densities of the condensed phase and the gas-like phase for both pores from Points B1 to D1 and B2 to D2 are the same (see the two horizontal dashed lines), confirming that:

1. the two phases are at equilibrium, and

2. this equilibrium (densities of two phases and the coexistence chemical potential) does not depend on whether the ends are open or closed, an assertion that we alluded to in the previous section.
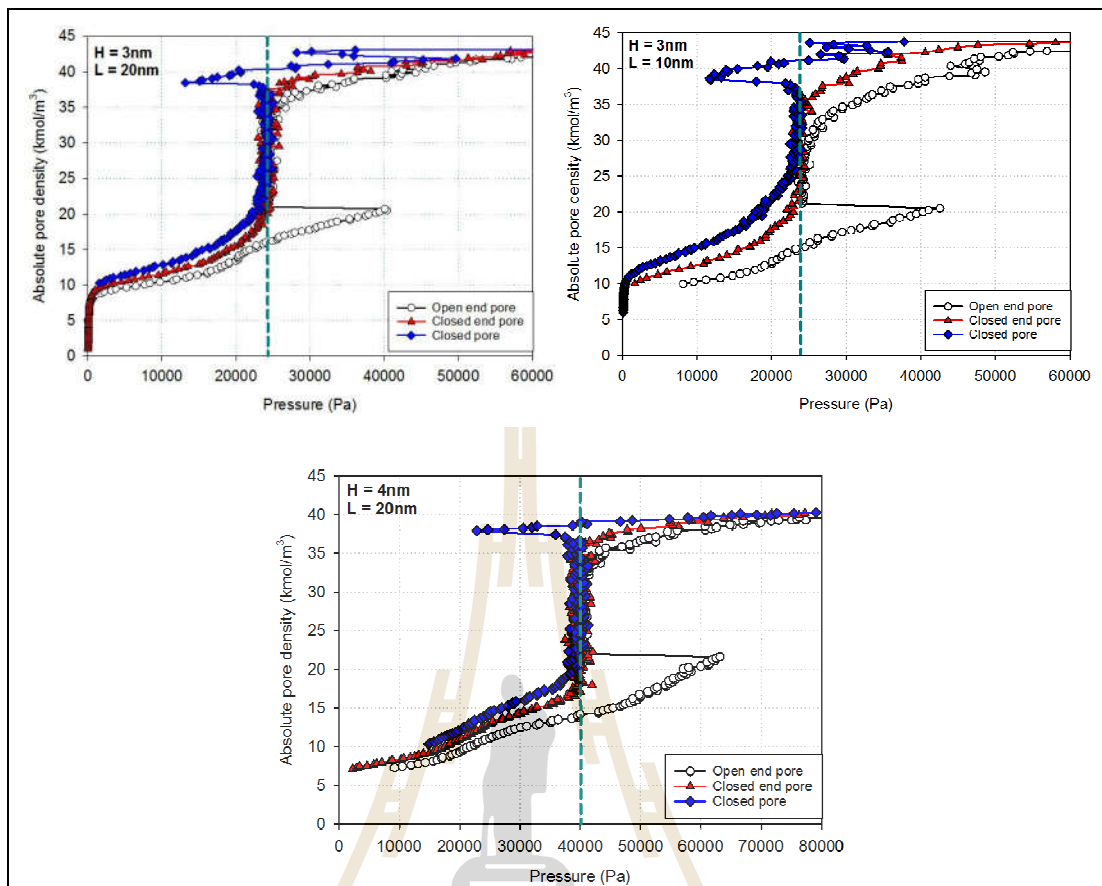
Figure 6.6 MCE isotherms for argon adsorption at 87 K in slit pores having different topologies. The vertical dashed lines show the common transition pressure for these slit pores.
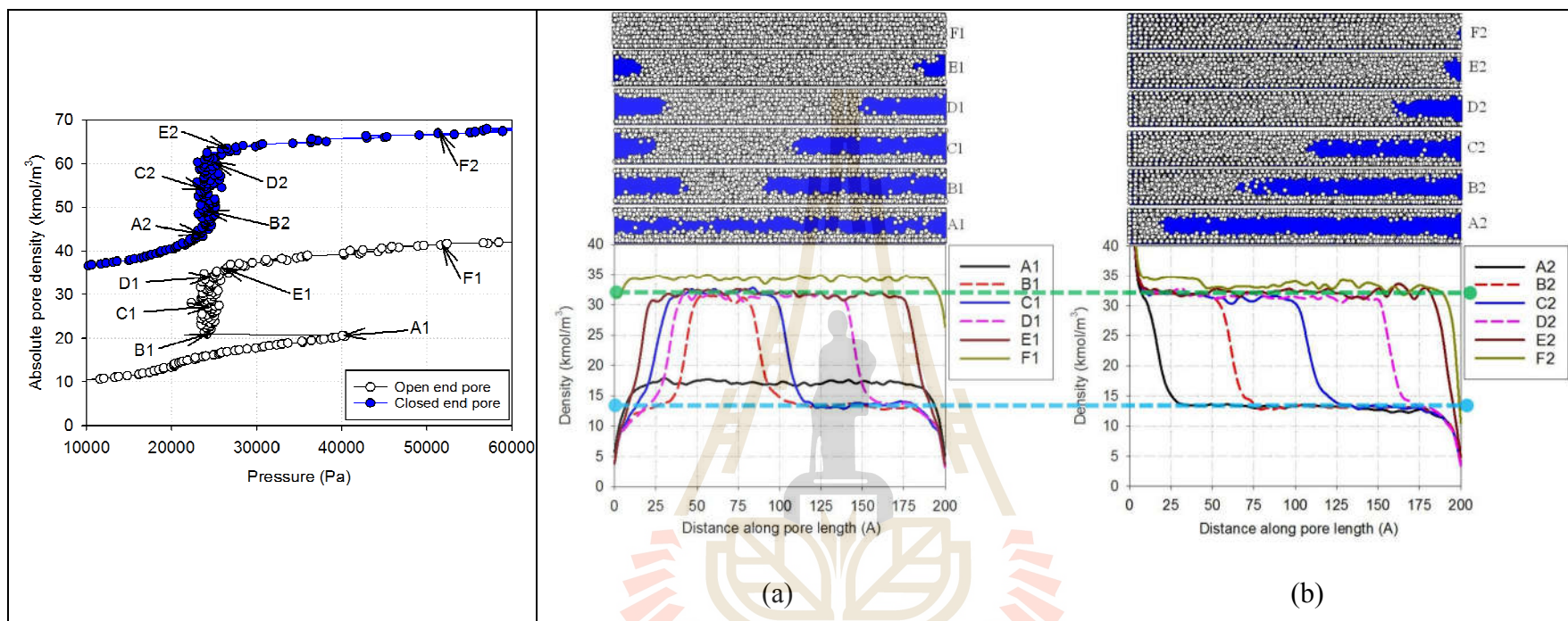
Figure 6.7 Shifted MCE isotherms (left panel) and local densities along the pore length (right panel) with increasing density of argon adsorption at 87 K in (a) open end and (b) closed end pores of 3 nm width and 20 nm length. The top and bottom horizontal dashed lines correspond to the mean densities of the condensed phase and adsorbed layer of argon for both pores, respectively. The closed end pore isotherm has been shifted upwards by 25 kmol/m³.

With further addition of molecules to Points F1 and F2 in both pores the condensed phase extends in length and there is a small jump in its density. This suggests that a molecular rearrangement has occurred which lowers the free energy of the adsorbate making it more cohesive, which is why the desorption transition takes place at a lower pressure than the adsorption transition, resulting in hysteresis in both the open end pore and the closed end pore in the grand canonical ensemble. In the open end pores, this cohesiveness is masked by the difference in the curvature of the interface in adsorption and desorption. However, in the closed end pores, the curvature for adsorption and desorption is the same, and therefore, in this case, it is the difference in cohesion of the molecules in the condensed phase that gives rise to hysteresis in the GCE isotherms. Further evidence in support of this conjecture is given in the next section where we analyze the structural change in greater detail.
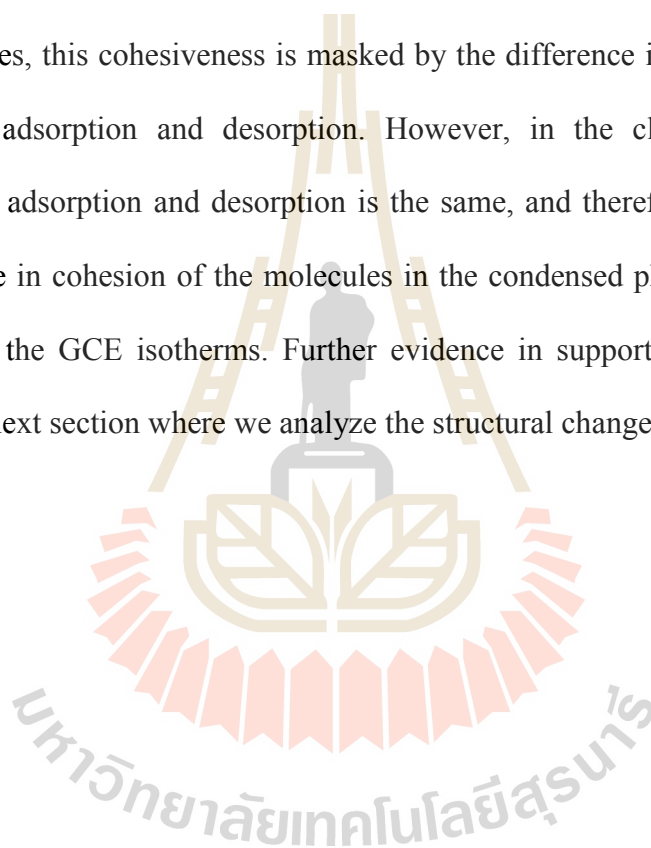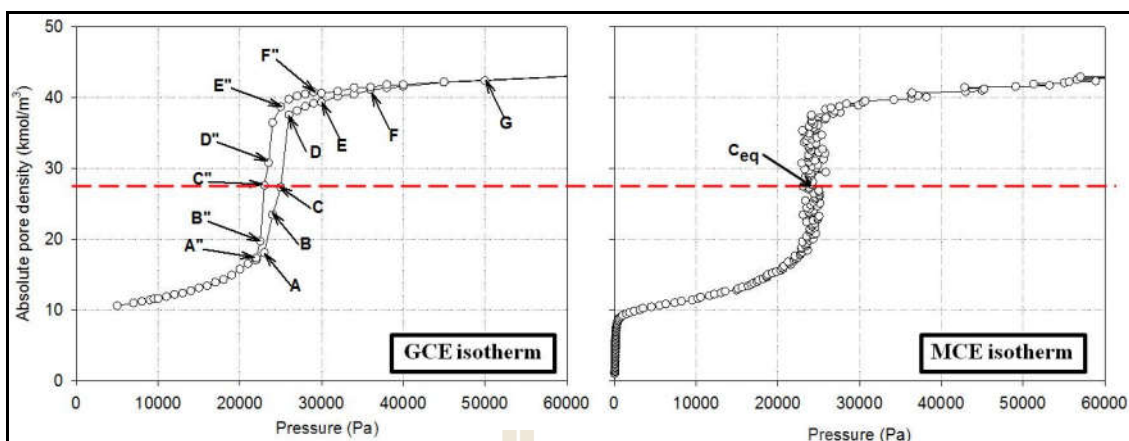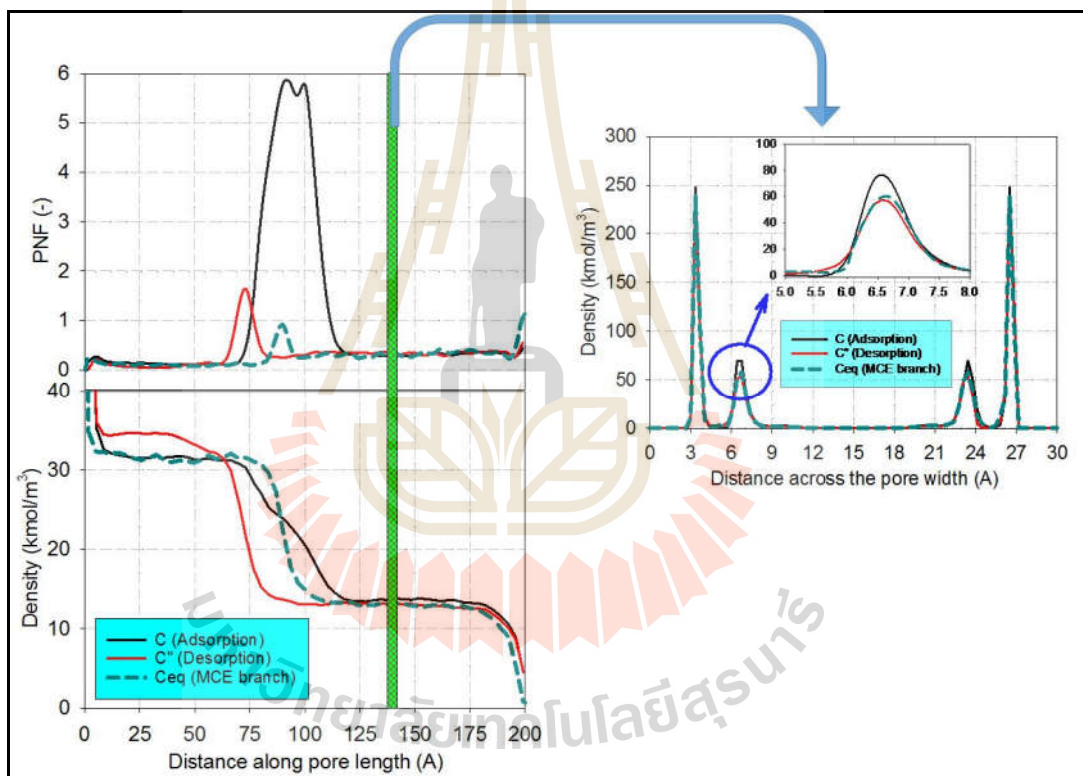
Figure 6.8 (a) GCE isotherm and (b) local properties along the pore length at the same pore density for argon adsorption at 87 K in a closed end pore of 3 nm width and 20 nm length. (c) The local density distributions across the pore width in the selected bin (shaded area in (b)).

6.4.2 Structural evolution of the adsorbed phase in a uniformed closed end (*C*-pore)

Figure 6.8a shows the GCE and MCE isotherm for the *C*-pore of 3 nm width and 20 nm length and we analyze the evolution of various points along the adsorption and desorption branches, shown in Figure 6.8b and 6.8c.

6.4.2.1 Structural analysis at the same pore density

To show the difference in the structures of the condensed phase along the adsorption and desorption branches, we selected two points having the same density and investigated the microscopic structures of the condensed phase at C and C" on the GCE isotherm, and the point C_{eq} on the MCE isotherm. A number of interesting points may be particular noted, some of which have not been widely recognized:

1. The density of the condensed phase (between 0 and 6 nm of the pore length) is distinctly higher along the desorption branch than along adsorption branch, indicating that the condensed fluid is more cohesive along the desorption branch. This means that desorption cannot occur until the pressure is lower that the adsorption pressure, and therefore that there will be hysteresis.

2. The density of the adsorbed layer in the gas-like region is greater during adsorption than that during desorption, as shown in Figure 6.8c.

3. The density of the condensed phase along the adsorption branch is the same as that at the equilibrium transition,

while the density of the gas-like region along the desorption branch is the same as that at the equilibrium transition.

4. Employing the undulation theory with the particle number fluctuation plot, we can locate the fluctuation (interface) region where the molecules are exchanged between the condensed phase and the gas-like phase. Interestingly, the amplitude and size of the fluctuation region for adsorption are greater than those for desorption and equilibrium; this will be discussed further in Section 6.4.2.2.

To shed further light on how the structure evolves within the *C*-pore, we next investigate the adsorption and desorption branches separately in the following section.

6.4.2.2 Evolution of adsorption

Figure 6.9 shows the plots of density versus the axial distance along the pore in the *C*-pore at Points A-G in Figure 6.8a of the GCE isotherm. The evolution of the density profiles can be classified into two groups.

Group I: developing meniscus (Points A-D)

In this group the meniscus is formed at the closed end and then advances toward the pore mouth. The density of the condensed phase is 32 kmol/m^3. To gain further insight, we plotted the 1D-, 2D- density and PNF profiles at Point C (taken as an example) in Figure 6.10. From these plots we can see three distinct regions: the condensed phase (left region), the interface region where the PNF is maximum and the gas-like phase (including the adsorbed layers on the pore walls). In Section 6.4.2.1 we raised the question of why the size of the undulating meniscus

128

for adsorption is much broader that that for desorption. We can now see that this is because molecules enter the condensed phase via the cylindrical interface as well as entering the meta-stable adsorbed layers in the gas-like region to make them thicker. Consequently, there are two mechanisms occurring simultaneously: the advance of the meniscus and the growth of the adsorbed layer in the coexistence region.
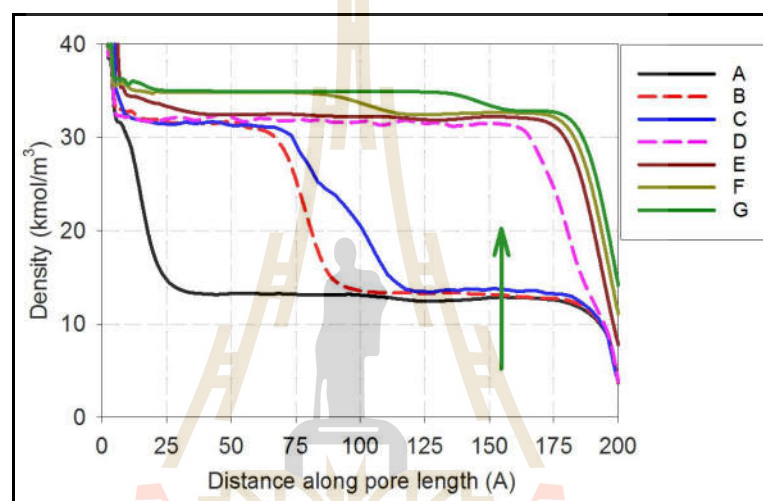
Figure 6.9   The local density distributions along the pore length during adsorption, at Points A-G on the GCE isotherm in Figure 6.8a. The arrow denotes the evolution of density of the adsorbed layers.
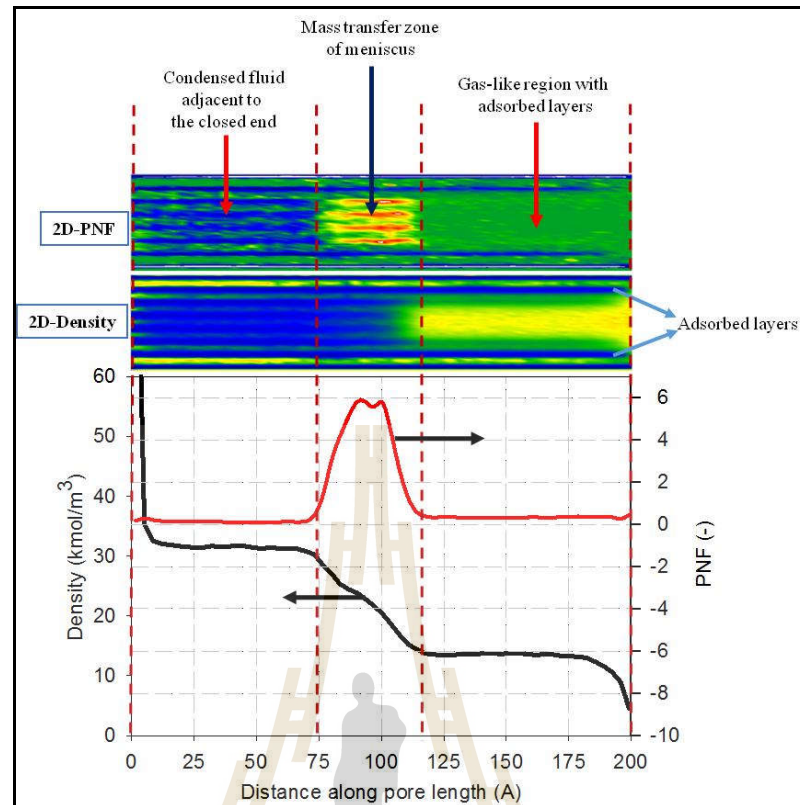
Figure 6.10   1D- and 2D-local density distributions and particle number fluctuations as a function of distance from the closed end at Point C labeled in Figure 6.8a.

Group II: restructuring of adsorbate (Points D-G)

Restructuring starts to occur when the meniscus has reached the pore mouth, where the solid-fluid interaction is weaker, and this is compensated by an increase in the fluid-fluid interaction advancing from the closed end. This results in the adsorbate restructuring, with an increase in the density, which is exhibited as a wave stemming from the closed end (see Point E-G in Figure 6.11a). To support this argument, we take two sections at Point F (shown as the shaded areas in Figure 6.11b) to investigate the local density distributions across the pore as shown

in Figure 6.11c. The first section is where the condensed fluid has been restructured and the second section is where it is still unstructured. This once again confirms the restructuring of the condensed phase after the meniscus has reached the open end.

6.4.2.3 Evolution of desorption

Figure 6.12 shows the local density as a function of the axial distance along the pore during desorption from Points A"-F" (as marked in Figure 6.8a). This figure conforms to observations in the recent communications (Nguyen et al., 2013; Zeng et al., 2014) as follows:

1. The density of the adsorbed layers in the gas-like region, as well as its thickness, remains constant.

2. The withdrawal of the meniscus is the only mechanism for the removal of molecules from the condensed phase, resulting in a narrower interface region, as evidenced by the narrow peak of the PNF plot, as discussed in Section 6.4.2.1, and the meniscus profile is identical in shape to that at equilibrium (see Figure 6.8b)

As the pressure is progressively decreased, the density of the condensed phase remains the same as that acquired after the restructuring in the adsorption cycle. Because the adsorbate is more structured, the desorption therefore occurs at lower pressures, giving rise to hysteresis in the GCE isotherm. Thus, the restructuring of adsorbate is the microscopic origin for the hysteresis loop in the closed end pore.
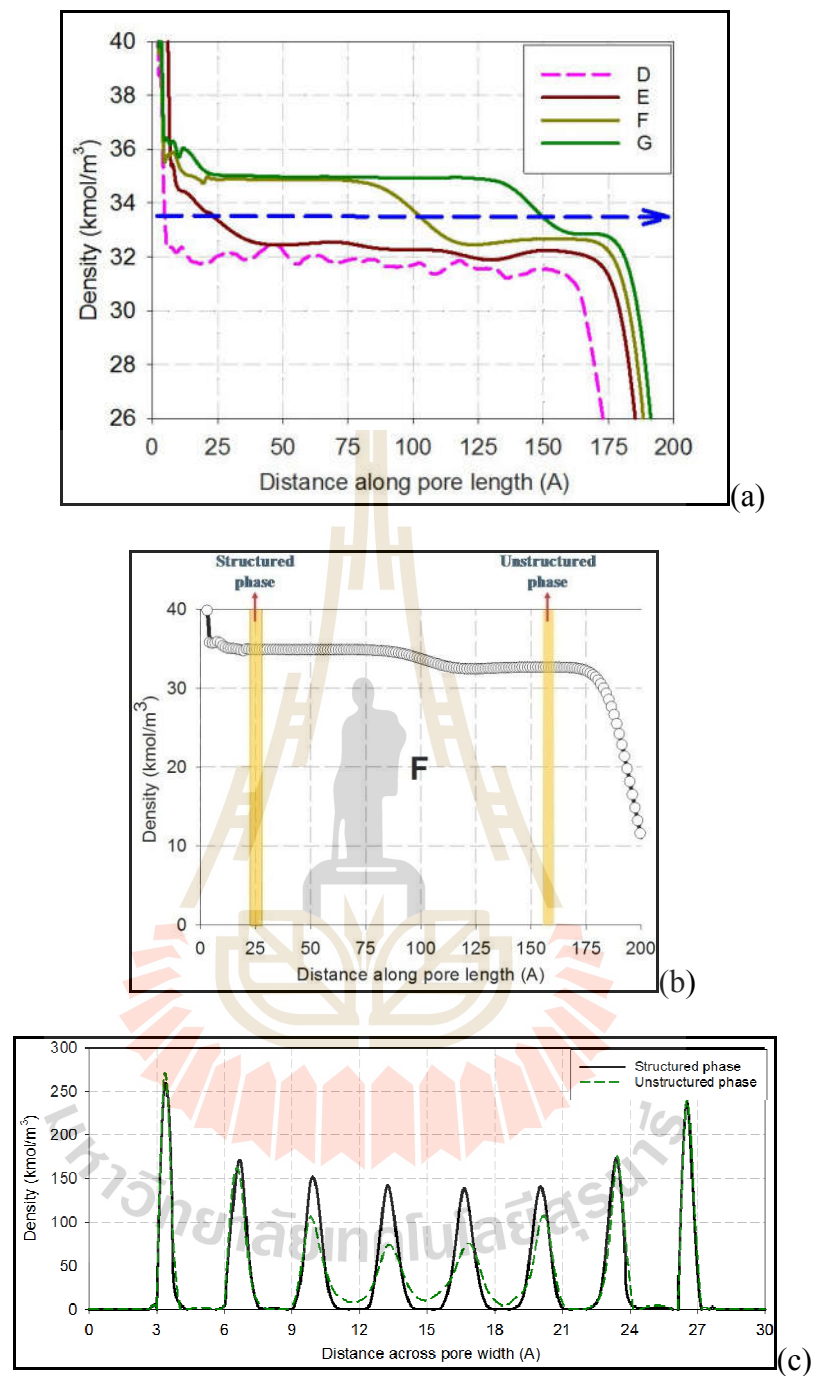
Figure 6.11 (a) The evolution of the restructuring of the adsorbate during adsorption from Points D-G, marked on the GCE isotherm in Figure 6.8a. (b) The local density distribution as a function of distance from the closed end at Point F. (c) Comparison of density profiles as a function of pore width in the two selected regions shaded in (b).
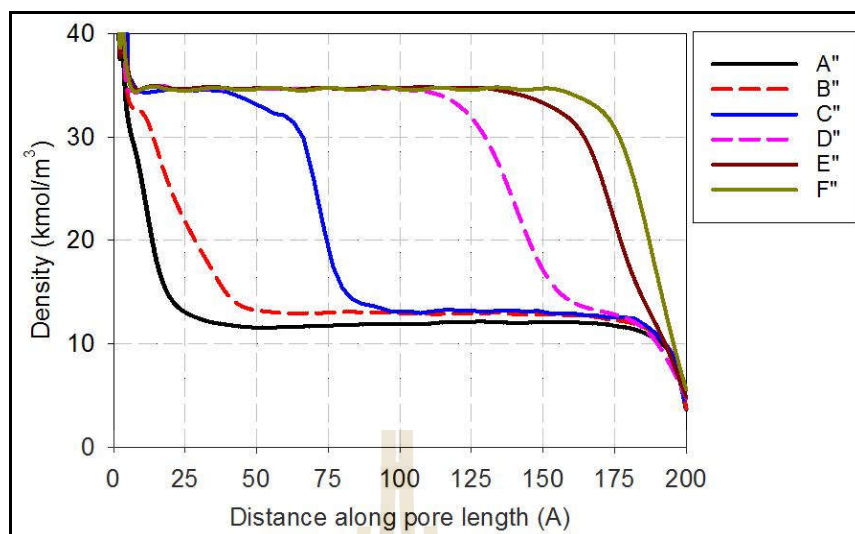
Figure 6.12 The local density distributions for the GCE isotherm along the pore length during desorption. The Points A"-F" are labeled in Figure 6.8a.

6.5 Conclusions

We have presented a rigorous and extensive simulation study of argon adsorption at 87 K to explain the microscopic origin of hysteresis in uniform sized pores. Three different topologies were considered: pores open at both ends, pores closed at one end and pores closed at both ends. Isotherms for these pores were obtained for two different simulation schemes: GCE and MCE. From our investigation of simple pores having the same pore dimensions, we find that the vertical segments of their MCE isotherms coincide at the same pressure when the menisci within the pores travel further away from the closed end or liquid bridge. This has not been recognized previously, and shows further clear evidence for the microscopic origin of the hysteresis loop in this kind of pore.

We have also substantiated the existence of a hysteresis loop in the closed end pore by investigating the microscopic structures of the adsorbate as a function of pore length along adsorption, desorption and equilibrium branches. The conclusions from this study can be summarized as follows:

1. The equilibrium branch is a combination of adsorption and desorption.

2. For adsorption, the width and amplitude of the undulating menisci are an indication of a thicker adsorbed layer.

3. Desorption occurs at a slightly lower pressure because the fluid within the pore becomes more structured, and this is the origin of the hysteresis loop in the closed end pore.

6.6 References

Binder, K. (1987). Theory of first-order phase transitions. **Reports on Progress in Physics** 50: 783.

Bravina, L.V. and Zabrodin, E.E. (1995). Aspects of the bubble nucleation in a first order phase transition. **Physics Letter A** 202: 61-67.

Debenedetti, P.G. (1996). **Metastable Liquids**. Princeton University Press, Princeton.

Fan, C., Do, D.D. and Nicholson, D. (2014a). On the existence of a hysteresis loop in open and closed end pores. **Molecular Simulation** 41: 245-255.

Fan, C., Zeng, Y., Do, D.D. and Nicholson, D. (2014b). An undulation theory for condensation in open end slit pores: critical hysteresis temperature and critical hysteresis pore size. **Physical Chemistry and Chemical Physics** 16: 12362-12373.

Frenkel, J.I. (1946). **Kinetics Theory of Liquids**. Oxford University Press, London.

Hill, T.L. (1994). **Thermodynamics of Small Systems**. Dover, New York.

Neimark, A.V. and Vishnyakov, A. (2000). Guage cell method for simulation studies of phase transitions in confined systems. **Physical Review E**. 62: 4611.

Neimark, A.V., Ravikovitch, P.I. and Vishnyakov, A. (2000). Adsorption hysteresis in nanopores. **Physical Review E**. 62: 1493-1496.

Nguyen, P.T.M., Do, D.D. and Nicholson, D. (2013). On the reversibility of the adsorption isotherm in a closed-end pore. **Langmuir** 29: 2927-2934.

Nguyen, V.T., Do, D.D. and Nicholson, D. (2011). Monte Carlo simulation of the gas-phase volumetric adsorption system: effects of dosing volume size, incremental dosing amount, pore shape and size, and temperature. **The Journal of Physical Chemistry B**. 115: 7862-7871.

Nguyen, V.T., Do, D.D. and Nicholson, D. (2011). Reconciliation of different simulation methods in the determination of the equilibrium branch for adsorption in pores. **Molecular Simulation** 40: 713-720.

Phadungbut, P., Nguyen, V., Do, D.D., Nicholson, D. and Tangsathitkulchai, C. (2014). On the phase transition in a monolayer adsorbed on graphite at temperatures below the 2D-critical temperature. **Molecular Simulation** 41: 446-454.

Puibasset, J., Kierlik, E. and Tarjus, G. (2009). Influence of reservoir size on the adsorption path in an ideal pore. **Journal of Chemical Physics** 131: 124123.

Zeng, Y., Phadungbut, P., Do, D.D. and Nicholson, D. (2014). Anatomy of adsorption in open-end and closed-end slit mesopores: adsorption, desorption, and equilibrium branches of hysteresis loop. **The Journal of Physical Chemistry C** 118: 25496-25504.

CHAPTER VII

DETERMINATION OF ABSOLUTE ADSORPTION
UNDER SUB- AND SUPERCRITICAL CONDITIONS

7.1 Abstract

A new method, employing computer simulation, is proposed for the determination of the location of the interface separating the adsorbed phase from the adjacent gas phase, giving a means to calculate the "absolute" amount adsorbed. The method involves monitoring the fraction of successful insertions of molecules into differential volumes in the simulation box. By applying the concept of equal areas, as implemented in the determination of the Gibbs dividing surface, for the profile of the fraction of success versus distance, we are able to determine the location of the interface bounding the adsorbed phase. This allows us to find (1) the thickness of the adsorbed phase, as a function of pressure. Knowing the absolute surface density as a function of pressure at different temperatures, we are able to calculate the heat of adsorption as a function of loading, using the Clausius-Clapeyron equation and to show that this is consistent with the heat obtained from the fluctuation formula in grand canonical Monte Carlo simulations.

7.2   Introduction

Physical adsorption of gases at supercritical temperatures under high pressures has been extensively studied experimentally (Zhou et al., 2003; Himeno et al., 2005; Dreisbach et al., 2002; Hemert et al., 2009; Jakubov et al., 2007; Salem et al., 1998; Wang et al., 2011) because of its importance in many applications such as energy storage and sequestration of carbon dioxide. Computer simulations under equivalent conditions have been made in attempts to understand their microscopic behavior better (Do and Do, 2005; Do et al., 2010; Fan et al., 2010; Kurniawan et al., 2006; Liu et al., 2012). It has been suggested that high pressure adsorption at supercritical temperatures does not extend beyond a monolayer, and as such the storage application of energy gases is of limited economic value because the densified adsorbate is essentially confined to a single layer (Zhou, 2012; Zhou et al., 2005; Sun et al., 2009). This implies that there are no suitable adsorbents such as carbon nanotubes or metal organic framework materials, which could be optimized for storage of energy under supercritical conditions. Application of solid adsorbents to store high energy gases requires a better understanding, at the microscopic level, of the mechanism of adsorption at supercritical temperatures, although some reservations have been put forward about the use of adsorption for energy storage (Bhatia and Myers, 2006).

There are three different descriptions of adsorbed amount: excess, net and absolute adsorption. The excess adsorbed amount is the difference between the total amount in the system and the amount in an apparent void space, at the same density as the bulk gas density. The choice of this void space leads to three definitions of adsorbed amount:

1. The helium void volume is measured by the expansion of helium, which is assumed to be non-adsorbed, into the void space. Since helium, despite its low polarizability, does actually adsorb, the helium void volume measured in this way is always greater than the actual physical void volume that an adsorbate molecule can access, resulting in negative excess amount. A better choice for the apparent volume is the accessible volume, which is defined as the volume in which the solid-fluid potential is non-positive since the excess density gives a good measurement of how dense the adsorbed phase is, relative to the surrounding bulk gas.

2. When apparent volume is taken as the volume of the system, including the solid volume, the result is called the net adsorption (Gumma and Talu, 2010; Talu, 2013; Pini, 2014). This can also lead to a negative amount adsorbed, and the density does not reflect the density of the actual adsorbed phase.

3. When the apparent volume is defined as the volume occupied by the surrounding gas, the adsorbed amount is an absolute quantity and therefore it is amenable to thermodynamic treatment. However this raises the problem of how to determine the boundary that demarcates the adsorbate phase from the surrounding gas. The search for a solution to this problem is the objective of this chapter. We will demonstrate our new method with argon adsorption on a graphite surface under subcritical and supercritical conditions.

7.3   Simulation

Due to argon used to study in this work, the intermolecular interaction energy was calculated by the 12-6 Lennard-Jones equation. For the adsorbent, we used a graphitic slit pore which its width is large enough so that the adsorption occurred on two independent surfaces over the pressure range studied. In the GCMC simulation, we used 60,000 cycles for the equilibrium stage and the same number for the sampling stage. Each cycle consisted of 1,000 attempted displacements, insertions or deletions.

7.4   Fraction of Success

In order to determine the interface between the adsorbed phase and the gas-like region, we have developed a new method based on the concept of fraction of success (*FoS*) of the insertion attempts in the simulation. Using a similar procedure to the one developed in the determination of accessible volume, we determine the fraction of success by dividing the simulation box into differential bins, and recording the fraction of success for total number of attempted insertions in each bin. This gives the fraction of success as a function of position. For example, in bin number *j*, bounded by z and $z+\Delta z$, the fraction of success is:

$$FoS_j \;=\; \frac{M_{success,j}}{M_j} \tag{6.1}$$

where M_j is the number of insertion attempts in bin j and $M_{success,j}$ is the number of successful insertions.

On the surface considered here, there are two flat interfaces bounding the adsorbed phase: (1) the one separating the adsorbed phase from the adsorbent and (2) that separating the adsorbed phase from the gas-like phase.

For the first boundary, we considered the system at zero loading, the fraction of success profile is a step function located at the position z_0 where the solid-fluid potential energy is zero. This is simply the boundary of the accessible volume (Herrera et al., 2011).
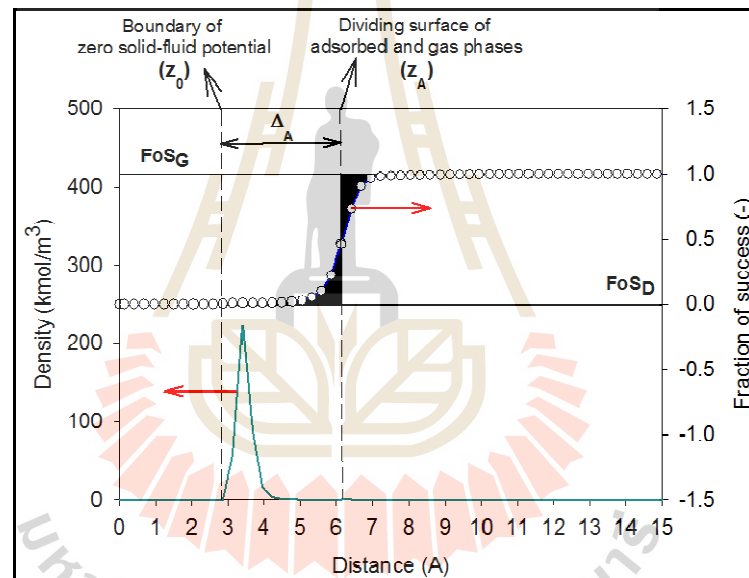
Figure 7.1   The fraction of success of complete monolayer argon adsorbed on graphite and its determination of a planar dividing interface. The region shaded black shows the illustration of determination of the boundary, with the area to the left boundary being the same as that to the right.

At temperatures greater than 0 K, the profile of the fraction of success at the second boundary becomes diffuse across the interface zone, varying between zero, close to the surface, and 1.0 in the rarefied phase (see Figure 7.1). An unambiguous way of to locate this boundary is to equate the excess area between zero and the fraction of success curve to the left of the boundary with the corresponding excess area to the right in analogy with the procedure used to locate a Gibbs interface. The position of the boundary so-defined is shown as z_A, in Figure 7.1. In terms of the two identified boundaries, we can now determine:

1. The thickness of the adsorbed phase: $\Delta_A = z_A - z_0$.
2. The volume of the adsorbed phase: $V_A = S \times \Delta_A$, where S is the area of the surface.
3. The number of molecules N_A with centers within the adsorbed phase which can be counted as being adsorbed molecules.
4. The absolute surface density: N_A / S (molecule/m^2).
5. The volumetric density of the adsorbed phase: N_A / V_A.

7.5   Results and Discussion

7.5.1   Fraction of success of the bulk phase

We performed GCMC simulation for a bulk fluid with a cubic box with periodic boundaries having a linear dimension of 10 nm at temperatures ranging from subcritical to supercritical. The plots of density versus pressure and *FoS* against pressure are shown in Figure 7.2. From this figure, we made the following observations:

1. At subcritical temperatures, well below the critical point (Figure 6.2a), the gas phase is rarefied, the fraction of success is very close to unity, and is linearly related to the gas density as shown in the inset.

2. As the density is increased, the fraction of success decreases because it is more difficult to insert molecules in a dense system, especially at high pressures under supercritical condition (Figure 7.2b)

7.5.2 Argon adsorption on graphite at subcritical conditions

The concept of fraction of success is particular useful for adsorption on an open surface. The method enables a clear description of how the boundary of the adsorbed phase shifts with pressure under sub- and supercritical conditions.

The GCMC isotherms at 77 K and 87 K and their local density distribution, fraction of success and particle number fluctuation, are shown in Figure 7.3. Points A, B and C on the 87 K isotherm correspond to one, two and three statistical layers, respectively. We determined the position of the interface separating the adsorbed phase (I) and the gas-like phase (II) using the equal area principle applied to plots of the fraction of success versus distance; shown as the vertical dashed lines in the middle panel. Interestingly the location of the interface determined from the *FoS* method is identical to the peak position of the particle number fluctuation, suggesting that the boundary of the adsorbed phase coincides with the position where the mass exchange is a maximum.
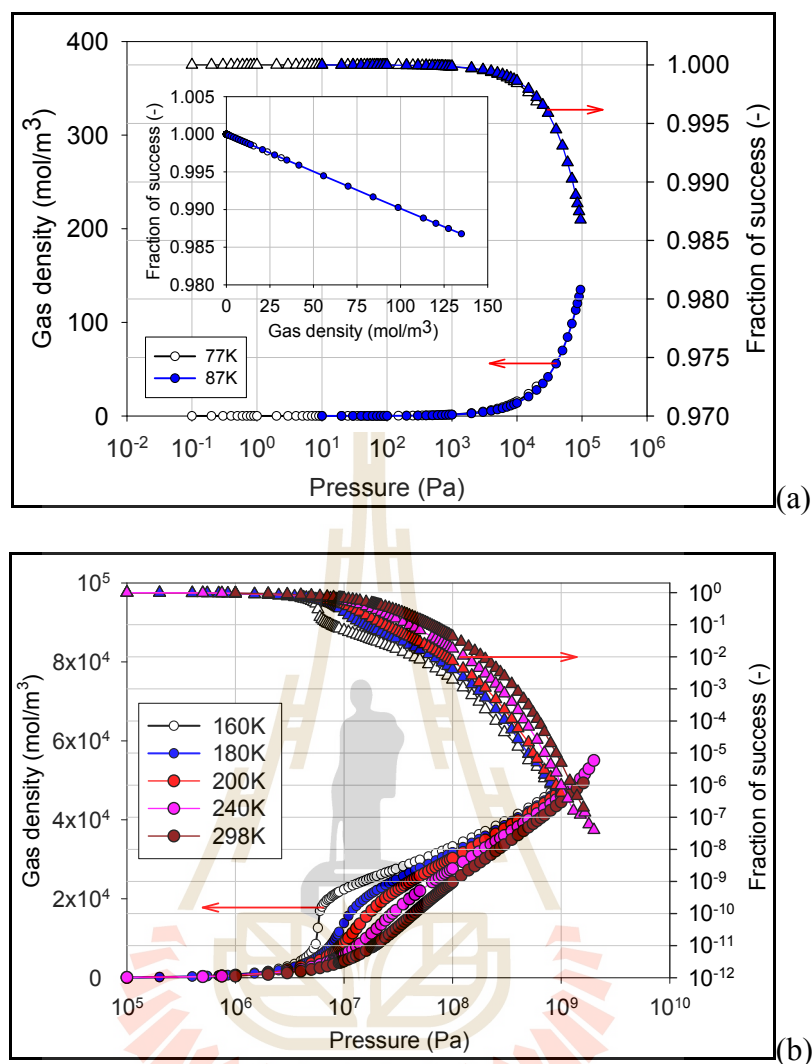
Figure 7.2   The density and fraction of success of argon as a function of pressure at (a) subcritical and (b) supercritical conditions.

For argon at 87 K, adsorption proceeds by molecular layering as loading is increased. According to the undulation theory the adsorbed region is within the boundary where the fraction of success is approximately zero. For example at Point C the local density distribution shows 4 peaks, but only the first three are within the adsorbed region and the *FoS* is close to zero outside the region of these three peaks. The fourth peak resides in the region where the *FoS* starts to increase from zero

to the *FoS* of the bulk gas phase and this is also the region where the PNF is a maximum, suggesting that this is the region where mass exchange occurs between the adsorbed region and the gas phase as defined by the undulation theory.

The absolute isotherm was determined using the *FoS* procedure; Figure 7.4a, shows that the boundary of the adsorbed phase increases linearly at subcritical temperatures, there is no difference between the absolute and excess isotherms shown in Figure 7.3. We note that the thickness of the adsorbed layer is equal to one argon collision diameter at the monolayer coverage. We will show below that different observations are found at supercritical temperatures.

Figure 7.4b shows the volumetric density of the adsorbed phase, i.e. the ratio of the number of molecules in the adsorbed phase to the volume of the adsorbed phase. A number of observations can be made from this plot:

1. In the sub-monolayer coverage, the volumetric density of the adsorbate increases linearly with loading.

2. The volumetric density of the adsorbate is higher at lower temperatures.

3. The volumetric density of the adsorbate reaches a maximum when the monolayer has been completed, beyond which it decreases because the density of the second and higher layers is lower. At 87 K, the maximum adsorbed density is 35 kmol/m^3, which is very close to the density of the bulk liquid, suggesting that the argon monolayer is liquid-like at this temperature. At 77 K, the maximum density is 38 kmol/m^3, suggesting that the argon monolayer is solid-like at the lower temperature. As loading is increased the

volumetric density of the adsorbate increases slightly before reaching a plateau.

7.5.3 Argon adsorption on graphite at supercritical conditions

The potential utility of the *FoS* approach is brought out by the analysis of adsorption at supercritical temperatures where there has been much debate about how best to obtain an absolute adsorption isotherm.

Figure 7.5 shows the excess and absolute adsorption isotherms for argon adsorption on grahite at 298 K, and the local density distribution and *FoS* versus distance from the surface. The excess isotherm exhibits a maximum because the apparent gas phase density increases more rapidly that the total density at higher pressures. On the other hand, the absolute isotherm increases monotonically and, perhaps the most interesting feature, reaches a constant value at extremely high pressures. To our knowledge, this has not been noted previously and we return to this observation below.
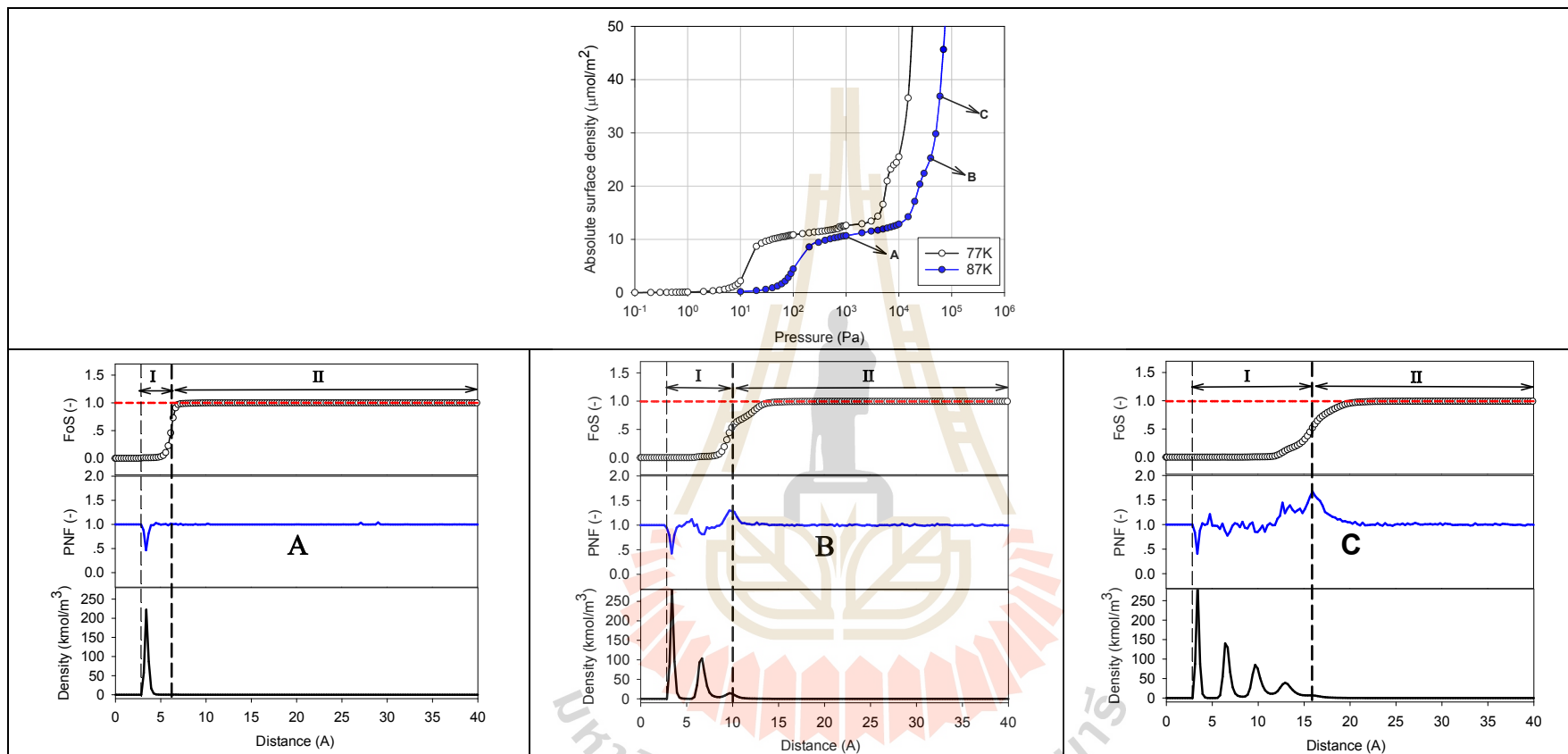
Figure 7.3   Absolute adsorption isotherm of argon on graphite at 77 K and 87 K and local density distribution, fraction of success and particle number fluctuation of 87 K. The left and right vertical dashed lines are the boundaries of zero solid-fluid potential and the gas-adsorbed planar interface, respectively. The horizontal dashed lines are the fraction of success of bulk gas.
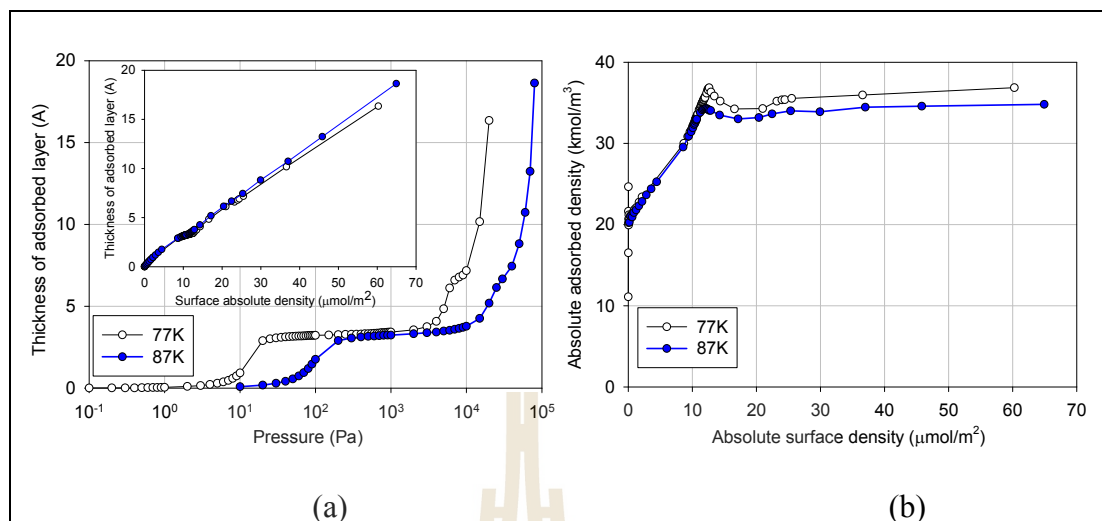
Figure 7.4   (a) Thickness of adsorbed layer and (b) absolute adsorbed density of argon adsorption on graphite at subcritical conditions.

First we consider the local density distribution and the *FoS* versus distance at Points A, B and C, on the absolute isotherm. We make the following observations that distinguish supercritical from subcritical adsorption:

1. The *FoS* in the first layer at supercritical temperatures is not zero; this is due to the increase in thermal fluctuations at high temperatures. From the computational standpoint it is easier to reach equilibrium at high temperatures.

2. The peaks of the *FoS* versus distance are commensurate with the peaks of the local density distribution; this means that it is easier to insert molecules in these regions that in the regions between the peaks where insertion is inhibited by overlap with molecules on either side.

Figure 7.5 Absolute and excess adsorption isotherms for argon on graphite at 298 K and the local density distribution and fraction of success. The left and right dotted vertical lines are the boundary of zero solid-fluid potential and the gas-adsorbed planar interface, respectively. The thick red arrow line indicates the reduction of the interface width from Point B to C.
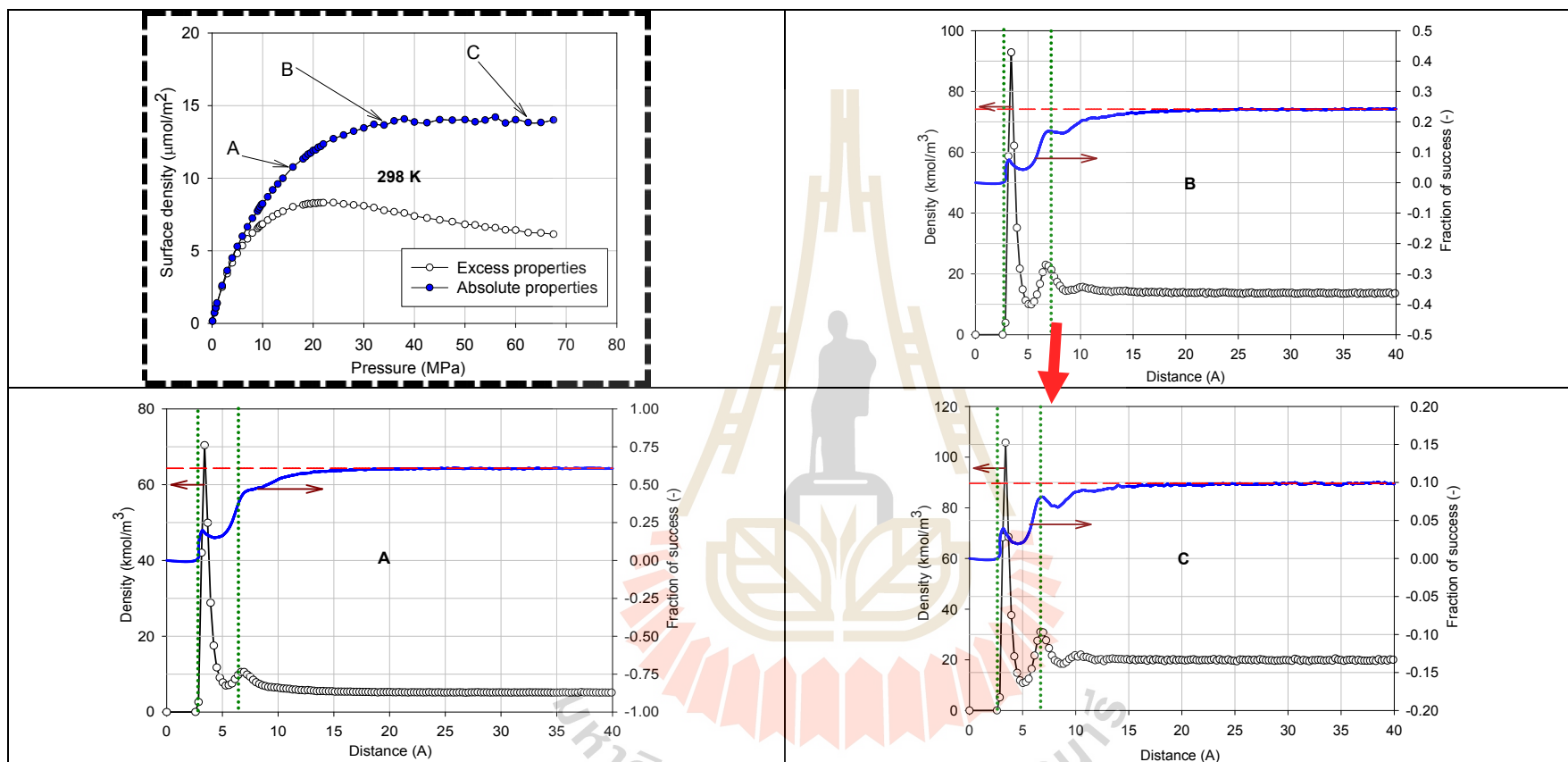
3. The height of the first peak in the local density distribution increases with loading, indicating the densification of this layer as pressure is increased; however this densification is accompanied by a slight decrease in the thickness of the adsorbed layer and as a result, the absolute surface density reaches a constant.

4. At Point B and C, the thickness of the adsorbed layer is equivalent to no more than one and a half molecular diameters, and this supports the view that supercritical adsorption is mainly confined to about one monolayer.

To shed further light on adsorption at supercritical temperatures, it is informative to study the effects of increasing the temperature. In Figure 6.6 we show the absolute isotherms and plots of the absolute density of the adsorbate and the thickness of the adsorbed layer for temperatures ranging from 200 K to 298 K. The excess and absolute isotherms have the same features as those already discussed for 298 K; the only difference being the level of the plateau in the absolute isotherm.

As the absolute surface density is decreased at higher temperatures, the thickness of the adsorbed phase is also decreased, as seen in the right panel of Figure 7.6, which is in agreement with the work of Murata et al. (2001). One interesting feature that has apparently not been previously recognized is that the thickness decreases when the absolute surface density has reached the plateau. This is a process of densification at supercritical temperatures when pressure is extremely high, as is also observed in the bulk fluid, as confirmed by the continuous increase in the peak height of density of the first layer as pressure is increased (as shown in the Figure

7.5). It has also noted in Figure 7.2 and 7.6 that the volumetric adsorbed density continues to increase and approaches the liquid density of argon of 35 kmol/m^3.

In Figure 7.7 the isosteric heats, calculated from the fluctuation formula in the GCMC simulations, are compared with heats from the Clausius-Clapeyron equation using the absolute adsorption isotherms at different temperatures. Good agreement between the heat curves confirms the physical consistency of the absolute adsorbed amount obtained from the concept of equal area applied to plots of fraction of success versus distance.
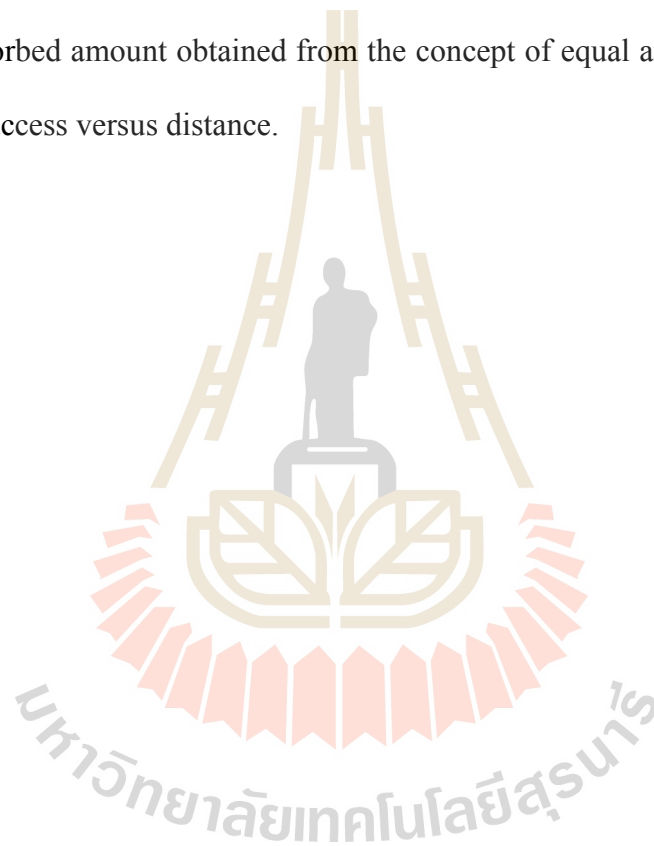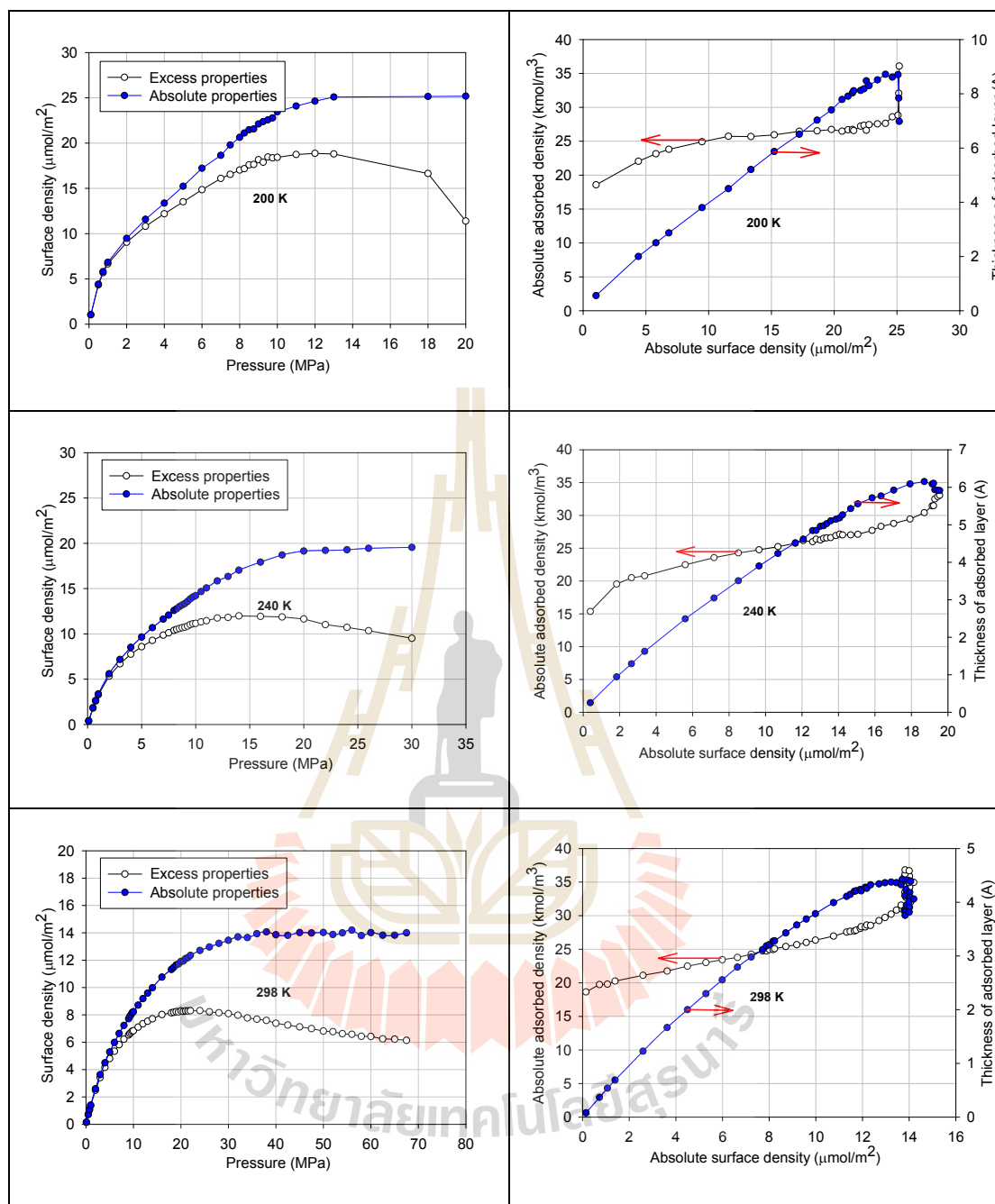
Figure 7.6 Absolute and excess adsorption isotherm (left panel) and thickness of adsorbed layer and absolute adsorbed density (right panel) for argon adsorbed on graphite at supercritical temperatures.
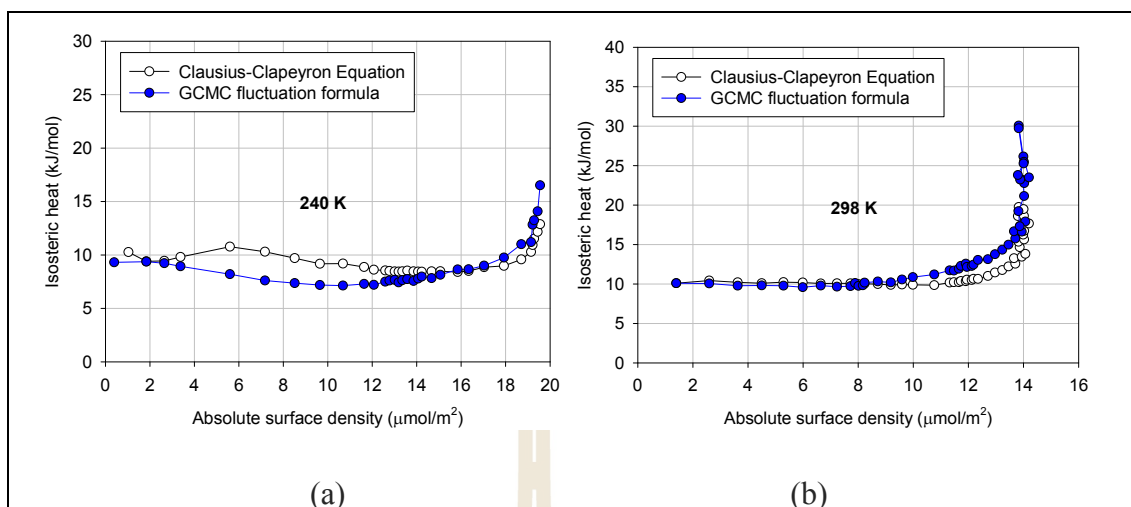
Figure 7.7 Isosteric heat of adsorption at (a) 240 K and (b) 298 K obtained from the Clausius-Clapeyron equation and from the fluctuation formula.

7.6 Conclusions

We have proposed a novel approach for the determination of the boundaries of the adsorbed phase, based on the concept of fraction of success. We have applied the new method to simulation of a bulk phase and to data for the adsorption of argon on a graphite surface at sub- and supercritical temperatures.

A number of interesting points arise from our consideration of supercritical adsorption; an area in which there has been controversy about how the absolute adsorption isotherm should be computed. Our conclusions from this study can be summarized as follows:

1. The adsorbed phase is very probably confined to no more than two layers above the surface.

2. The absolute surface density reaches a constant value at extremely high pressure, and this value decreases with increasing temperature.

3. The adsorbed phase is densified as pressure is increased, and the thickness of the adsorbed phase is slightly decreased at extremely high pressures, such that the overall effect is a densification.

4. The volumetric adsorbed density approaches the bulk liquid state density of 35 kmol/m^3, suggesting that <u>the limit for the process of densification of the adsorbed phase is a liquid-like state</u>.

7.7 References

Bhatia, S.K. and Myers, A.L. (2006). Optimum conditions for adsorptive storage. **Langmuir**. 22: 1688-1700.

Do, D.D. and Do, H.D. (2005). Adsorption of argon from sub- to supercritical conditions on graphitized thermal carbon black and in graphitic slit pores: a grand canonical Monte Carlo simulation study. **Journal of Chemical Physics**. 123: 084701.

Do, D.D., Do, H.D., Fan, C. and Nicholson, D. (2010). On the existence of negative excess isotherms for argon adsorption on graphite surfaces and in graphitic pores under supercritical conditions at pressures up to 10,000 atm. **Langmuir**. 26: 4796-4806.

Driesbach, F., Losch, H.W. and Harting, P. (2002). High pressure adsorption equilibria data: measurement with magnetic suspension balance and analysis with a new adsorbent/adsorbate-volume. **Adsorption**. 8: 95-109.

Fan, C., Do, D.D., Li, Z. and Nicholson, D. (2010). Computer simulation for argon adsorption on graphite surface from subcritical to supercritical conditions: the behavior of differential and integral molar enthalpies of adsorption. **Langmuir**. 26: 15852-15864.

Gumma, S. and Talu, O. (2010). Net adsorption a thermodynamic framework for supercritical gas adsorption and storage in porous solids. **Langmuir**. 26: 17013-17023.

Hemett, P.V., Bruining, H., Rudolph, E.S.J., Wolf, K. and Maas, J.G. (2009). Improved manometric setup for the accurate determination of supercritical carbon dixide sorption. **Review of Scientific Instruments**. 80: 035103.

Hererra, L., Fan, C., Do, D.D. and Nicholson, D. (2011). A revisit to the Gibbs dividing surfaces and helium adsorption. **Adsorption**. 17: 955-965.

Himano, S., Komatsu, T. and Fujita, S. (2005). High-pressure adsorption isotherms above the critical temperature on microporous adsorbebts; application to methane. **Journal of Chemical Engineering Data**. 50: 369-376.

Jakubov, T.S. and Jakubov, E.S. (2007). Adsorption volume and absolute adsorption: 1. Adsorption from a gaseous phase. **Colloid Journal**. 69: 666-670.

Kurniawan, Y., Bhatia, S.K. and Rudolph, V. (2006). Simulation of binary mixture adsorption of methane and CO_2 at supercritical conditions in carbons. **AICHE journal**. 52: 957-967.

Liu, Y. and Wilcox, S.K. (2012). Molecular simulation studies of CO_2 adsorption by carbon model compounds for carbon capture and sequestration applications. **Environmental Science & Technology**. 47: 95-101.

Murata, K., El-Merraoui, M. and Kaneko, K. (2001). A new determination method of absolute adsorption isotherm of supercritical gases under high pressure with a special relevance to density-functional theory study. **Journal of Chemical Physics**. 114: 4196-4205.

Pini, R. (2014). Interpretation of net and excess adsorption isotherms in microporous adsorbents. **Microporous and Mesoporous Materials**. 187: 40-52.

Salem, M.M.K., Braeuer, P., Szeombathely, M., Heuchel, M., Harting, P., Quitzsch, K. and Jaroniec, M. (1998). Thermodynamics of high-pressure adsorption of argon, nitrogen, and methane on microporous adsorbents. **Langmuir**. 14: 3376-3389.

Sun, Y., Liu, C., Su, W., Zhou, Y. and Zhou, L. (2009). Principles of methane adsorption and natural gas storage. **Adsorption**. 15: 133-137.

Talu, O. (2013). Net adsorption of gas/vapor mixtures in microporous solids. **The Journal of Physical Chemistry C**. 117: 13059-13071.

Wang, Y., Helvensteijin, B., Nizamidim, N., Erion, A.M., Steiner, L.A., Mulloth, B. and LeVen, M.D. (2011). High pressure excess isotherms for adsorption of oxygen and nitrogen in zeolites. **Langmuir**. 27: 10648-10656.

Zhou, L. (2005). Progress and problems in hydrogen storage methods. **Renewable Sustainable Energy Reviews**. 9: 395-408.

Zhou, L., Bai, S., Su, W., Yang, J. and Zhou, Y. (2003). Comparative study of the excess versus absolute adsorption of CO2 on superactivated carbon for the near-critical region. **Langmuir**. 19: 2683-2690.

Zhou, Y. and Zhou, L. (2009). Fundamentals of high pressure adsorption. **Langmuir**. 25: 13461-13466.

CHAPTER VIII

CONCLUSIONS AND RECOMMENDATIONS

8.1   Conclusions

This thesis work encompasses a fundamental study on the characterization of porous carbons and the adsorption of gases both on graphitized carbon surface and in graphitic pores with different pore topologies. Two ensembles of the Monte Carlo simulation were used to investigate the microscopic explanation of hysteresis loop and adsorption mechanism for argon under subcritical and supercritical conditions. The output of this study will be worthwhile to understand the structural characteristics of porous carbons and its fundamental physics of gas adsorption to benefit the adsorption processes for practical applications, such as separation, purification and energy storage.

The first objective of this thesis is to develop the method for determining the pore volume, surface area and pore size distribution of porous carbons. This is achieved by introducing the differential 3D-grid as the position of a center of probe molecule to test its accessiblity, rather than employing the random insertion within the simulation space. This proposed method was applied to a number of simple pore models and a more complex simulated porous carbon. The porous properties of which were compared with those of longan seed-derived activated carbon. The results indicated that the computation method proposed in this work was able to calculate the porous properties of porous carbons faster than those of the previous one. Moreover,

the textural properties and nitrogen adsorption isotherm of a simulated porous carbon determined by this method showed that the resultant carbon structure coincide with activated carbon structure derived at low degree of activation.

Argon adsorption on graphite and in slit pores with different pore sizes at temperatures below 2D-critical temperature were analyzed for the 2D-phase transitions, consisting of vapor-solid, vapor-liquid and liquid solid transitions, using Grand Canonical (GCE) and Meso-Canonical (MCE) ensembles. The simulated isotherm of argon adsorbed on graphite exhibits the single hysteresis loop with a sigmoid vdW loop, brought about by the phase change. However, for the first time in literature, it is noted that the isotherm in large slit pores show a single hysteresis loop with two sequential vdW loops, where each loop is associated with the unstable state of phase evolution. When the pore wall become closer, the vdW loop alters from double loops to a fused single loop. At the same time, the adsorption mechanism also shifts from a surface adsorption to pore filling.

Another objective of this thesis is the investigation and analysis of capillary condensation in cylindrical and spherical pores. The extension of undulation theory was applied to observe the development of undulating interface as the loading is increased. Unlike the classical theory, the fluctuation region plays an important role for capillary condensation in pores, apart from the dense adsorbed and gas-like regions. The increase of pore size, temperature, adsorbent field strength and degree of curvature results in the wider width of the fluctuation region. By analyzing the fluid cohesiveness within cylinders and spheres at the pressure point just prior to condensation, the interfacial parameter is always greater than the bulk phase value and then converges to the bulk value when the pore diameter is increased.

The adsorption in slit mesopores of uniform width with non-ended, one-ended and two-ended closed was studied to investigate the microscopic origin of hysteresis loop. Our results show that the adsorbate restructuring and re-distribution of molecules in pores is the microscopic reason for the hysteresis, which is in contrast to which the classical theory reports that the reversibility always exhibits the adsorption in one-ended closed pores.

For the last section of the thesis, another aspect of adsorption under supercritical conditions was investigated systematically. The novel concept based on the fraction of successful insertions of probe molecules has been proposed to determine the absolute adsorbed amount and density of adsorbed phase. We applied the new method to the argon adsorption on a graphite surface at sub- and super-critical temperatures. At supercritical condition, it is found that the adsorbed phase is confined about no more than two molecular layers above the graphite surface and the shape of absolute adsorption isotherm is similar to Type 1b of the IUPAC classification in 2015. At extremely high pressure, the density of adsorbed phase approaches that of bulk liquid, indicative of adsorbed phase behaving as liquid-like state.

8.2 Recommendations for future work

There are a number of aspects of the construction of simulated porous carbon and molecular simulation of gas adsorption that can be further studied in the future. These aspects are outlined below.

- The computational technique of pore characterization for porous solids having known atomistic structure proposed in Chapter 3 can be further applied to

derive the structural characteristics of other types of atomistic porous solids, such as metal organic framework (MOF), zeolite, porous glass and polymer.

- The molecular model of porous carbon in Chapter 3 is still needed to be further developed to take into account the effects of structured parameters of carbon microcrystallites and surface heterogeneity on the carbon structure and the adsorption behavior.

- The adsorption isotherm in pore connectivity should be further studied to reveal the origin of hysteresis loop and the stable, metastable and unstable states within the hysteresis loop by means of MCE at subcritical condition.

- In reality, the practical adsorption processes always involve with gas mixtures like natural and toxic gases. Therefore, the gas mixture adsorption is worth further investigations.

- In Chapter 7, we have proposed the determination method for absolute adsorbed amount but it is only applicable to the adsorption on a graphitic surface, where one side is solid system and the opposite is empty space. The fraction of success technique should be developed for the adsorption systems on a graphitic surface and in carbon slit pores. This topic will benefit the study of energy storage application in the future.

APPENDIX A

LIST OF PUBLICATIONS

LIST OF PUBLICATIONS

International Publications

Zeng, Y., Phadungbut, P., Do, D.D. and Nicholson, D. (2014). Anatomy of adsorption in open-end and closed-end slit mesopores: adsorption, desorption and equilibrium branches of hysteresis loop. **The Journal of Physical Chemistry C**. 118: 25496-25504.

Phadungbut, P., Nguyen, V.T., Do, D.D., Nicholson, D. and Tangsathitkulchai, C. (2014). On the phase transition in a monolayer adsorbed on graphite at temperatures below the 2D-critical temperature. **Molecular Simulation**. 41: 446-454.

Phadungbut, P., Do, D.D., Nicholson, D. and Tangsathitkulchai, C. (2015). On the phase transition of argon adsorption in an open end slit pore: effect of temperature and pore size. **Chemical Engineering Science**. 126: 257-266.

Phadungbut, P., Fan, C., Do, D.D., Nicholson, D. and Tangsathitkulchai, C. (2015). Determination of absolute adsorption for argon on flat surfaces under sub- and supercritical conditions. **Colloids and Surfaces A: Physicochemical and Engineering Aspects**. 480: 19-27.

Bruschi, L., Mistura, G., Phadungbut, P., Do, D.D., Nicholson, D., Mayamei, Y. and Lee, W. (2015). Adsorption on ordered and disordered duplex layers of porous anodic alumina. **Langmuir**. 31: 4895-4905.

Fan, C., Nguyen, V.T., Zeng, Y., Phadungbut, P., Horikawa, T., Do, D.D. and Nicholson, D. (2015). Novel approach to the characterization of the pore structure and surface chemistry of porous carbon with Ar, N_2, H_2O and CH_3OH adsorption. **Microporous and Mesoporous Materials**. 209: 79-89.

Phadungbut, P., Do, D.D. and Nicholson, D. (2015). Undulation theory and analysis of capillary condensation in cylindrical and spherical pores. **The Journal of Physical Chemistry C**. 119: 20433-20445.

Phadungbut, P., Do, D.D. and Nicholson, D. (2016). On the microscopic origin of the hysteresis loop in closed end pores: adsorbate restructuring. **Chemical Engineering Journal**. 285: 428-438.

Zeng, Y., Phadungbut, P., Do, D.D. and Nicholson, D. (2016). Wedge pore model as an alternative to the uniform slit pore model for the determination of pore size distribution in activated carbon. **The Journal of Physical Chemistry C**. 119: 25853-25859.

Phadungbut, P., Herrera, L.F., Do, D.D., Tangsathitkulchai, C., Nicholson, D. and Junpirom, S. (2016). Computational methodology for determining textural properties and adsorption isotherms of simulated porous carbons. (In preparation)

Prasetyo, L., Horikawa, T., Phadungbut, P., Tan, S. J., Do, D.D. and Nicholson, D. (2016). A GCMC simulation and experimental study of krypton adsorption/desorption hysteresis on a graphite surface. **Journal of Colloid and Interface Science**. (Submitted)

National Publication

Phadungbut, P., Julklang, W., Sriling, P., Intomya, W., Wongkoblap, A. and Tangsathitkulchai, C. (2012). Simulation study for adsorption of carbon dioxide and methane in carbon-nanotubes. **Engineering Transaction**. 15.

International Conference Proceeding

Phadungbut, P., Junpirom, S. and Tangsathitkulchai, C. (2013). Monte Carlo simulation of activated carbon structure and nitrogen adsorption for pore characterization. **Pure and Applied Chemistry International Conference (PACCON 2013)**. Chonburi, Thailand.

Phadungbut, P., Zeng, Y. and Do, D.D. (2013). Microscopic explanation of the lower closure point of 0.42 in nitrogen adsorption at 77K and argon at 87K in activated carbon. **OzCarbon 2013**. Melbourne, Australia.

Do, D.D., Fan, C., Zeng, Y., Phadungbut, P., Nguyen, V.T., Horikawa, T. and Nicholson, D. (2014). Novel approach to the characterization of the pore structure and surface chemistry of porous carbon with Ar, N_2, H_2O and CH_3OH adsorption. **COPS-X**. Granada, Spain.

Do, D.D., Tan, S., Zeng, Y., Phadungbut, P., Prasetyo, L., Fan, C., Klomkliang, N. and Nicholson, D. (2015). Mechanisms of adsorption and desorption of simple gases and associating fluids on surfaces and in confined spaces of porous carbon: effects of pore topology, surface chemistry and temperature. **PBAST-7**. Xiamen, China.

Phadungbut, P., Do, D.D., Nicholson, D. and Tangsathitkulchai, C. (2015). Determination of the volume and density of adsorbed phase by computer simulation under sub- and supercritical conditions. **PBAST-7**. Xiamen, China.

Do, D.D., Tan, S. J., Phadungbut, P., Zeng, Y., Prasetyo, L., Fan, C. and Nicholson, D. (2016). Characterization of porous solids for accessible volume, accessible area and excess versus absolute adsorption isotherm. **12th International Conference on the Fundamentals of Adsorption (FOA 2016)**. Friedrichshafen, Germany.

National Conference Proceeding

Phadungbut, P., Intomya, W., Wongkoblap, A. and Tangsathitkulchai, C. (2011). Study of methane adsorption in carbon nanotubes: computer simulation and experiments. **The 21st Thailand Institute of Chemical Engineering and Applied Chemistry Conference (TIChE)**.

Phadungbut, P., Julklang, W., Sriling, P., Intomya, W., Wongkoblap, A. and Tangsathitkulchai, C. (2012). A Monte Carlo simulation study for adsorption of carbon dioxide and methane in carbon nanotubes. **The 22nd Thailand Institute of Chemical Engineering and Applied Chemistry Conference (TIChE)**.

BIOGRAPHY

Mr. Poomiwat Phadungbut was born on the 4th of May 1989 in Bangkok Province of Thailand. After completing his high school education at his hometown, he then continued his undergraduate study at Suranaree University of Technology (SUT) and graduated with first-class honor degree in Chemical Engineering in 2011. On that same year, he was awarded the scholarship from the Royal Golden Jubilee (RGJ) programme to pursue his doctoral study in Chemical Engineering at SUT. During his Ph.D. study period, he had invaluably spent two years at the University of Queensland (UQ), Australia, for continuing research on the microscopic behaviour of gas adsorption in porous carbons by computer simulation.